Lukas Wittwer

Experimental and numerical investigations of pin structures and pin reinforced dissimilar joints

PhD Thesis

For obtaining the academic degree of
Doctor of technical science
(Doktor der technischen Wissenschaften)

Graz University of Technology

Institute for Materials Science and Welding
Head: Univ.-Prof. Dipl-Ing. Dr.techn. Christof Sommitsch

Supervisor: Assoc.Prof. Dipl-Ing. Dr.techn. Norbert Enzinger

January 2014

Statutory Declaration

I declare that I have authored this thesis independently, that I have not used other than the declared sources/resources, and that I have explicitly marked all material which has been quoted either literally or by content from the used sources.

Graz, ______________________ ______________________

Date Signature

Eidesstattliche Erklärung

Ich erkläre an Eides statt, dass ich die vorliegende Arbeit selbstständig verfasst, andere als die angegebenen Quellen/Hilfsmittel nicht benutzt, und die den benutzten Quellen wörtlich und inhaltlich entnommenen Stellen als solche kenntlich gemacht habe.

Graz, am ______________________ ______________________

Datum Unterschrift

Abstract

Modern lightweight design demands for joining of dissimilar materials, e.g. plastics and metals. One possibility of enhancing such joints are pin structures on metal surfaces. Using a special welding technique - the cold metal transfer (CMT)- pins of different shape can be placed on metal sheets. In this work we sought to understand the welding process itself as well as the role of pins in an actual joint. In doing so we performed various experimental investigations (such as metallography, light and electron microscopy). Special focus was given on the connection between pin an substrate, which was an issue in the case of aluminum pins. Furthermore we conducted a series of surveys concerning the base material's mechanical performance under the influence of the pin welding process. Eventually, we investigated the role of pins in a dissimilar joint between austenitic stainless steel and carbon fiber reinforced plastics. In addition to the experimental work we carried out numerical simulations using the finite element method. First, we investigated the temperature distribution and evolution during the welding process of a single pin. Secondly, we focused on the mechanical performance of a single pin and later on dissimilar joints reinforced with pins. The latter was achieved using the cohesive zone contact formulation between metal and plastics.

Acknowledgments

I want to thank *Norbert Enzinger* for giving me the opportunity to carry out this thesis and for his competent guidance throughout the whole time. Furthermore I express my gratitude to all members of the joining group and all the people with the *Institute of Materials Science and Welding.*

Furthermore I would like to thank all our partner in the Join4+ project 2.2. Special thanks to Almedin Bećirović and Andreas Waldhör from Fronius Internatianl for their expertise in simulations and pin welding as well as Stephan Uscnik from the LKR Ranshofen for his valuable advises.

Eventually I want to thank my family and friends for their support throughout the years.

This work was carried out within the framework of the K-Project Join4+. The K-Project Network of Excellence for Joining Technologies JOIN4+ is fostered in the frame of COMET - Competence Centers for Excellent Technologies by BMVIT, BMWFJ, FFG, Land Oberösterreich, Land Steiermark, SFG and ZIT. The program COMET is handled by FFG.

Contents

List of Figures

List of Tables

1. Introduction

Modern lightweight construction demands for combining different types of materials in order to achieve an optimum between maximum strength and weight reduction. In doing so fiber reinforced plastics have come in the spotlight for the last two decades and thus joining metals and plastics has become an issue.

A very common and widely used method of joining metals and plastics is to use adhesives. Such joints can be improved by adding mechanical reinforcements such as bolts or rivets [1]. The described techniques are state of the art in many branches of industry like automotive or shipbuilding industry. The failure mechanisms in such joints are subject to current research [2, 3].

However, further developments in light weight design having increased the use of composite materials, e.g. carbon fiber reinforced plastics, demand for improvements in joining composites and metals. Pin structures on metal surfaces pose a mechanical reinforcement to ordinary adhesive joints with respect to forces perpendicular to the metal surface. Therefore pins are placed on a metal sheet substrate by use of a special arc welding technique called cold metal transfer (CMT), developed by Fronius International [4]. In the case of fiber reinforced plastics the fibers may be woven around the pins or the pins can be impressed into the fiber mats and then be processed further. It has been demonstrated that joints reinforced by pin structures exhibit a considerable increase of strength in comparison to joints without pins [5].

This work aims to obtain a deeper understanding of the pin welding process itself as well as to understand the mechanisms of pins in dissimilar joints.

In order to understand the pin welding process our first investigations aimed to pins made of stainless steel. Further, we investigated the welding of aluminum pins using the classic CMT procedure and a variant of it - the drop by drop method. Here we focused on the quality of the interface zone between filler and base material. Another point was the influence of the welding process on the mechanical performance of the base material.

Further experimental investigation concerned actual joints between stainless steel plates with pins and carbon fiber reinforced plastics.

Supplemental to the experimental investigations we performed finite element analyses of the welding process in order to get deeper insights concerning temperature evolution and distribution. In order to get optimized parameters for the Goldak heat source [6] we applied an optimization scheme called the artificial bee colony (ABC) algorithm. Furthermore, numerical surveys of pin reinforces dissimilar joints were carried out. For that matter we aimed to find a simplified mechanical model based on the *cohesive zone* approach.

Eventually this work is concluded with a summary and discussion of the most important findings.

2. Fundamentals

In this chapter the basic techniques used in this work are presented. In the first two paragraphs different ways of generating pin structures on metal surfaces are described. The third section deals with simulation tools that we used in order to get a deeper understanding of the investigated processes. Eventually, the last part of this chapter describes an optimization scheme applied in order to refine the numerical models.

2.1. The cold metal transfer process

One possibility to produce pin structures is the *cold metal transfer* (CMT) process. It is a special gas metal arc welding (GMAW) technique developed by Fronius International [4]. This process was designed originally for joining aluminum sheets with steel. The key element of the CMT process is the controlled back and forth movement of the filler wire during the arc is burning. This rapid movement stimulates the detachment of the drop at the wire's tip.

Welding pins poses a special application of the aforementioned CMT process. In principal, a pin welding process is structured in the following stages (compare Haslinger [7]):

Stickout During the stickout phase the wire tip is placed at the surface of the plate and a current is applied for several milliseconds preheating the wire. At the end of the stickout phase the arc ignites.

Heating During this stage the arc burns causing the wire to heat up to melting temperature and a liquid droplet is forming at the wire's tip. While the arc is burning the wire approaches the substrate until it touches it. At this point the arc is turned off and the heating phase is finished. The wire is now attached to the base material.

Pullback Right after the wire attaches to the base material it is pulled backwards sharply forming the typical conical pin foot.

Cooling During this stage the whole system calms down. Due to the large volume of the plate compared to the wire most of the heat flows from the wire to the base material. As a consequence the zone of maximum temperature is migrating upwards in the wire.

Shaping Depending on the amount of time the zone of maximum temperature reaches a certain point in the wire. As a consequence the electric resistance is highest in this area. When applying an electric current, the wire will heat most at the point of maximum temperature and electric resistance, respectively. In addition to the applied current the wire is pulled backwards. Since the tensile strength decreases with rising temperature the wire will break at the point of maximum temperature. Depending on the time and the speed as well as the amount of applied current differently shaped pin heads are possible.

The process described above is graphically depicted in Figure 2.1. As mentioned above the shape of the pin head depends on the process parameters (current, velocity of the pullback, ...):

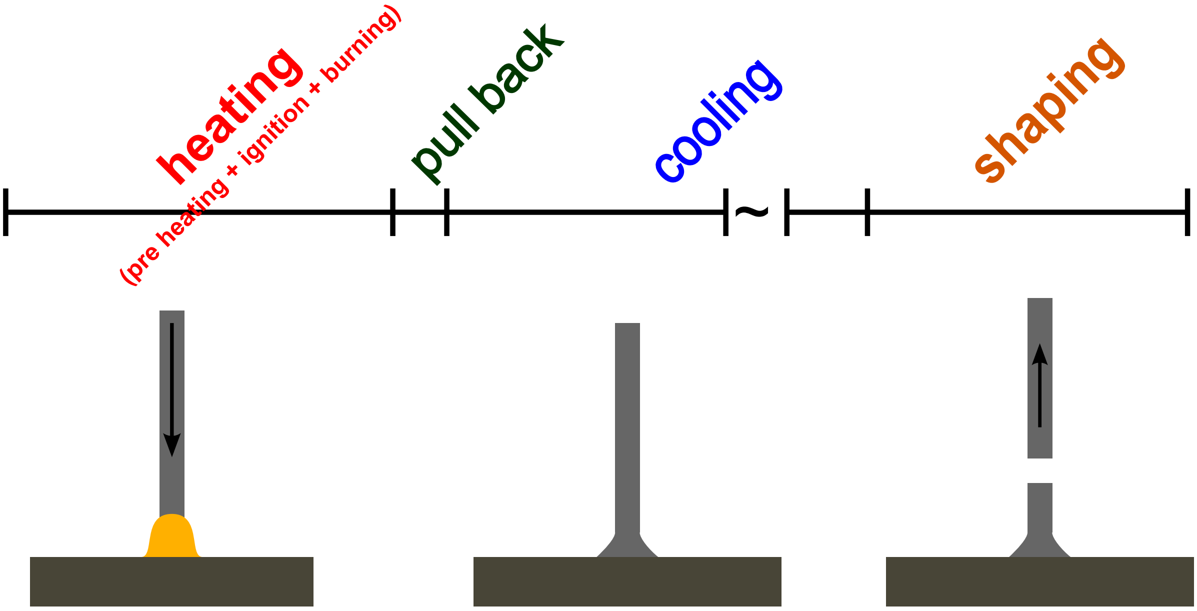

Figure 2.1.: Illustration of the different stages of the pin welding process.

Cylindric In the case of cylindrical pins the pullback of the wire happens after the current is applied. Thus the wire break right when the material reaches its melting temperature.

Ball pins are formed if the time delay between applying the current and pulling back the wire is larger than for cylindric pins. Combined with low pull back velocity an extended liquid zone forms within the wire before it break. Surface tensions of the liquid wire forms the ball at the pin's head.

Spiky For those pins the delay between the current and the pullback is larger than for cylindrical and ball pins, but the applied currents is much lower. Thus the necking in the zone of maximum temperature is very distinct leading to the spiky pin head.

2.2. Electron beam welding

A totally different approach on placing pins on a metal surface is by means of electron beam welding (EBW). While in the case of the CMT process the pins consist of additional filler material, the EBW procedure uses the base material itself in order to generate pins. In the work of Schultz the electron beam welding process is described in full detail [8]. The brief description given below is intended as a short overview for the sake of completeness. Figure 2.2a depicts the basic setup of an EBW machine. The whole welding process must be carried out under evacuated conditions. In the case of EBW the energy input needed to melt the workpiece results from electrons hitting the material's surface and the kinetic energy of the electrons transforms to heat. The energy input per length reads then as follows:

$$E = \frac{UI}{v}, \tag{2.1}$$

with U and I being the voltage at the electron gun and I the beam current. Basically U defines the kinetic energy of the electrons and I orchestrates the amount of electrons emitted. Electrons have only little mass (rest mass $\approx 9 \times 10^{-31}$ kg) and are accelerated to very high velocities (up to 70 % the speed of light), therefore the electron beam shows very little inertia and may be deflected virtually instantaneously. Furthermore it is possible to focus the beam on a very small area, resulting in high energy densities. Thus, this welding technique allows for very deep and narrow energy penetration into the working piece, causing the material to melt in the close vicinity of the beam, the so called *keyhole evaporation*. In the middle of the keyhole the material vaporizes the resulting vapor pressure in combination with the relative movement of work piece and beam transfer the molten material to the back of the keyhole where it accumulates (compare to Figure 2.2b). Due to the mechanisms described above, EBW seams usually exhibit a welding reinforcement a the end and a crater at the beginning. Normally, the

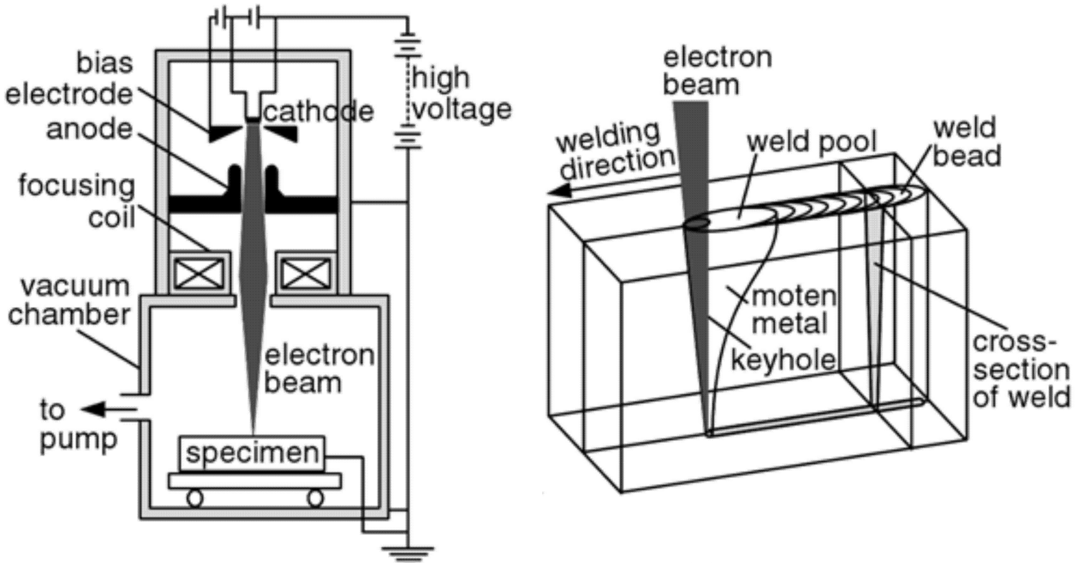

(b) Keyhole forming

(a) Process setup

Figure 2.2.: Schematic representation of the EBW process [9]

material accumulation at the back of the keyhole is not desired. However, in the context of generating pin structures on metal surfaces this effect is used specifically. Under the brand name SurfiSculpt® technology, invented at *The Welding Institute* [10], a method was elaborated to generate special surface structures by means of EBW.

2.2.1. Surfi Sculpt Technology

As mentioned above this technique makes use of the characteristic accumulation of material behind the keyhole. The electron beam moves away multiple times from a central point where more and more material accumulates at every step. In Figure 2.3 this process is sketched schematically - the pin is forming behind the beam with respect to the moving direction. For actual applications, different figures such as cross pattern (see Figure 2.4a) or even more sophisticated patterns (like in Figure 2.4b) are applied. Since the beam itself has hardly any inertia it can be deflected almost instantaneously, so it is not necessary to build one pin by another but an array of pins can be generated almost at once as illustrated in Figure 2.5. The branches denoted with the numbers 1-4 are carved consecutively then the beam goes back to position 5 and goes along the branches 5-8. This scheme is repeated until the 'star' is finished and in its center the pin emerges. The advantage of this procedure is that the heat input on the workpiece is equally distributed over the pin array during the welding process. Thus remelting of the

already formed pin can be avoided. In literature applications of such modified surfaces may be found, e.g. to enhance the mechanical performance of plastic-metal joints. In this context the author may point to the work of Wang et al [11, 12] and Buxton et al [13].
Another possible application of such surface texturing is presented in the work of Reisgen et al. [14]. Surfaces of bone implants are modified using EBW in order to stimulate their ingrowth behavior.

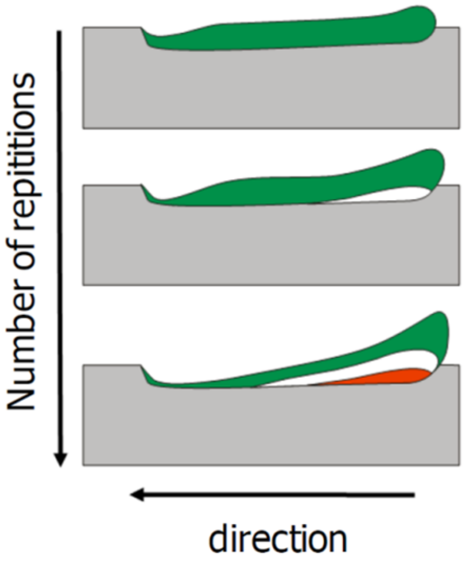

Figure 2.3.: Schematic representation of the creation of pins using SurfiSculpt technique [14, 15]

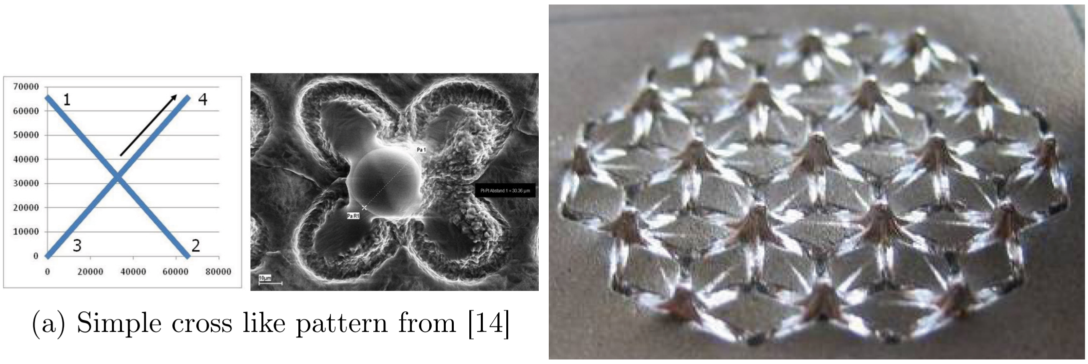

(a) Simple cross like pattern from [14]

(b) A more complex pattern from [12]

Figure 2.4.: Example of possible beam patterns in order to generate pin structures at metal surfaces

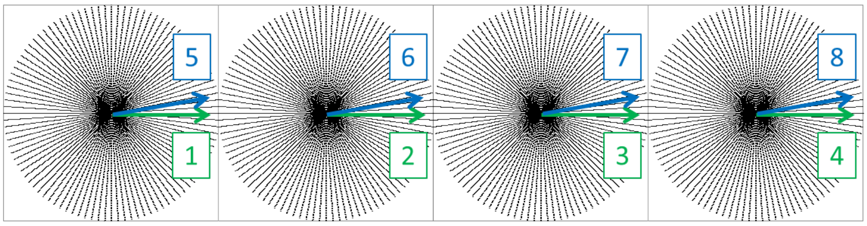

Figure 2.5.: Beam deflection and order when generating an array of pins using EBW according to Tändl et al [16]

2.3. Finite Element Method

The finite element (FE) method is a very powerful and common technique in order to solve the mathematics occurring within the framework of welding simulations. The FE method has been used for academic research since the 1970s. For industrial purposes is has become interesting in the early 1990s with the advent of adequately powered computers [17].

Basically, such a simulation consists of two parts, a *thermal* and based on that a *mechanical* part.

2.3.1. Thermal calculations

An excellent overview on solving thermal problems using the finite element method can be found in the lecture note of Prof. Heinrich Sormann [18]. The following explanations are deduced from this work.

In the thermal FE calculation, the heat conduction problem is solved, i.e. one has to solve the heat equation describing the energy balance of the system:

$$\frac{\partial T(\mathbf{x},t)}{\partial t} - \frac{\lambda}{c_p \rho} \nabla^2 T(\mathbf{x},t) = q. \tag{2.2}$$

The parameters λ, ρ and c_p denote the thermal conductivity, density and heat capacity, respectively. These are material parameters and they usually depend on temperature. The term q in equation 2.2 describes an external heat flow, in case of welding simulation this is the heat source. In order to solve equation 2.2 it is necessary to define initial and boundary conditions. In the beginning of a simulation the temperature in all points of an area Ω has some initial value T_0:

$$T(\mathbf{x}, t) = T_0(\mathbf{x}, t = 0)\ \forall \mathbf{x} \in \Omega. \tag{2.3}$$

Further, at the boundaries of the considered area one has to define the heat exchange with the surrounding medium. Such conditions may be:

- a fixed temperature (*Dirichlet boundary conditions*)

$$T = T^*(\mathbf{x}) \tag{2.4}$$

- or the spatial deviation of the temperature (→ heat flux, *Cauchy boundary conditions*)

$$-\frac{\lambda}{c_p \rho} \nabla T \mathbf{n} = q \tag{2.5}$$

$$-\frac{\lambda}{c_p \rho} \nabla T \mathbf{n} = h_{\text{env}}(T - T_{\text{env}}) \tag{2.6}$$

Usually one has to deal with mixed boundary conditions, i.e. on some edges the temperature is given and on others the heat flux. The quantity h_{env} is the so called *heat exchange coefficient* and T_{env} the environment's temperature. For very simple geometries equation 2.2 may be solved analytically, but within the framework of welding simulations usually one has to deal with complex structures and non linear material behavior. In the course of the FE analyses the considered area is divided in finite elements. Basically one has great freedom in choosing the shape or number of such elements, however for most problems triangular or/and tetragonal elements are used[1].

In terms of mathematics equation 2.2 is a special case of a parabolic partial differential equation which reads in its most general form as follows

$$\frac{\partial}{\partial x}\left(a_1 \frac{\partial f}{\partial x}\right) + \frac{\partial}{\partial y}\left(a_2 \frac{\partial f}{\partial y}\right) + gf + h = a_0 \frac{\partial f}{\partial t} \tag{2.7}$$

---

[1] This is true for two dimensional problems. In three dimensional cases the according elements are tetrahedral and octahedral. The further considerations will be elaborated for 2D structures but they can be easily extended to 3D cases.

with the Cauchy boundary conditions[2]

$$a_1 \frac{\partial f}{\partial x} n_x + a_2 \frac{\partial f}{\partial y} n_y + a_4 f = a_5. \tag{2.8}$$

where n_x and n_y are the components of the surface normal vector. Comparing the heat equation 2.2 with the general form 2.7 yields

$$a_1 = a_2 = -\frac{\lambda}{c_p \rho}, \quad a_0 = 1 \quad h = q \quad g = 0.$$

The Cauchy boundary conditions as presented in equation 2.5 describe internal heat sources (e.g. welding heat source), thus the coefficients a_4 and a_5 are:

$$a_5 = q \text{ and } a_4 = 0$$

In regions where the considered area experiences heat exchange with the environment condition 2.6 applies, it can be rewritten as

$$-\frac{\lambda}{c_p \rho} \nabla T \mathbf{n} - h_{\text{env}} T = -h_{\text{env}} T_{\text{env}}.$$

Comparing this with the Cauchy boundary conditions in their general form (equation 2.8) we get

$$a_4 = -h_{\text{env}} \text{ and } a_5 = -h_{\text{env}} T_{\text{env}}.$$

In order to solve equation 2.7 the following ansatz is used within the framework of FE analysis:

$$T(x, y, t) = \sum_{i=1}^{n} N_i(x, y) T_i(t) \tag{2.9}$$

where n is the total number of nodes and T_i is the temperature at the ith node. The *shape functions* $N_i(x, y)$ only depend on the shape of the used element type. They have to be continuously differentiable and must fulfill the following condition:

$$N_i(x, y) = \begin{cases} 1 & \text{at node } i \\ 0 & \text{at all other nodes} \end{cases} \tag{2.10}$$

A widely used method for determining the coefficients $N_i(t)$ is the *Galerkin* method.

---

[2] The case $a_5 \neq 0$ is called inhomogeneous boundary conditions.

The basic idea is that applying the ansatz 2.9 to equation 2.7 will not solve it exactly but yields a residual R which must be minimized. In doing so one ends up with a set of n algebraic equations that can be solved quite easily. A detailed explanation of the Galerkin method can be found in various textbooks on FE such as [19, 20].

Modeling the heat input in welding

As mentioned before, the heat input due to welding is described by a heat flux q implemented as a boundary condition in the FE analysis. The actual shape of such an input depends on the considered welding process.

The first models describing the heat input due to welding were already established in the 1930s (point and line heat sources). However, those models show significant shortcomings in order to predict the temperature distribution within a weld [17].

In *circular disc* models the surface heat flux $q(r)$ is distributed Gaussian like

$$q(r) = q_0 e^{-Cr^2} \tag{2.11}$$

where q_0 is the maximum at the center, C the width of the Gauss curve and r the radial distance from the center. For welding processes where the depth of penetration is negligible such as flame straightening such heat sources as in equation 2.11 may be sufficient. But for welding situations where deep penetration occurs (especially laser and electron beam welding) the model above is insufficient [17].

A further refinement in modeling was achieved by introducing volumetric heat sources. The most prominent representative in the context of arc welding is the *Goldak* heat source [6]:

$$q = q_0 e^{-\frac{3x^2}{a^2}} e^{-\frac{3y^2}{b^2}} e^{-\frac{3(z+v(\tau-t))^2}{c^2}} \tag{2.12a}$$

$$q_0 = \frac{6\sqrt{3}Q}{abc\pi\sqrt{\pi}} f \tag{2.12b}$$

In this model q represents power density with q_0 at its center. The shape of this power distribution is elliptic with the parameters a, b and c defining the ellipsoid's expansion (compare to Figure 2.6). The Goldak model was elaborated in order to mimic the heat input of a moving arc, thus the entity v denotes the velocity and t is the time. The term τ is a reference time parameter defining the heat source's position at time $t = 0$. As depicted in Figure 2.6 the Goldak heat source is divided in two section, one in front and one in the rear of the center with respect to the velocity vector. Therefore one has to find two sets of parameters a, b and c for those two sections. Eventually, the parameter f orchestrates the power deposition in the front and rear part of the heat source. However, the quantities a, b and c are just auxiliary parameters that must be adopted for the current welding situation. For that reason they have to be redefined if for example the considered material or welding parameters (e.g. voltage, current ...) change. It is common practice to deduce the values of the geometry parameters (a, b and c) from cross sections of experimental welds [17].

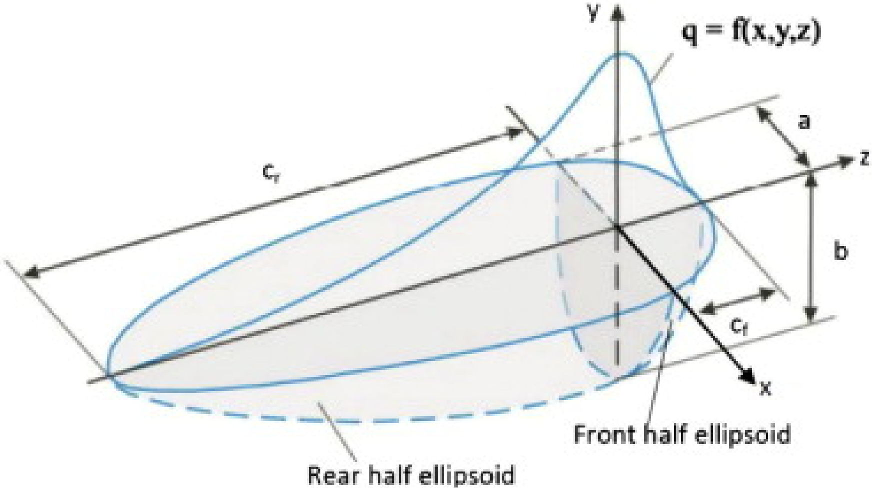

Figure 2.6.: Graphical illustration of Goldak's double ellipsoidal heat source; from [21]

2.3.2. Mechanical calculations

In the framework of welding simulations displacements also result from thermal strains. Thus deformations, due to the heat input of welding, are calculated by use of the temperature field resulting from thermal calculations. Thus, a temperature field $T(x, y)$ is transferred to a displacement filed $U(x, y)$ via the thermal expansion coefficient α

$$U(x, y) = \alpha T(x, y). \tag{2.13}$$

Within the finite element formulation deformations $U(x, y)$ are expressed by shape functions $N(x, y)$

$$U(x, y) = \sum_{l=1}^{m} U_l N_l(x, y) \tag{2.14}$$

where m is the number of nodes in the considered element and U_l the displacement of the l-th node. The strains then compute as

$$\epsilon = \begin{pmatrix} \epsilon_{xx} \\ \epsilon_{yy} \\ \tau_{xy} \end{pmatrix} = \begin{pmatrix} \frac{\partial U}{\partial x} \\ \frac{\partial U}{\partial x} \\ \frac{\partial U}{\partial y} + \frac{\partial y}{\partial x} \end{pmatrix} \tag{2.15}$$

or in matrix notation

$$\begin{aligned} \boldsymbol{\epsilon} &= \boldsymbol{L}\boldsymbol{U} \\ \boldsymbol{\epsilon} &= \boldsymbol{L}\boldsymbol{N}\boldsymbol{U}_l \\ \boldsymbol{B} &= \boldsymbol{L}\boldsymbol{N} \end{aligned} \tag{2.16}$$

with the strain-displacement transformation matrix for the l^{th} node reading

$$\boldsymbol{B}_l = \begin{pmatrix} \frac{\partial N_l}{\partial x} & 0 \\ 0 & \frac{\partial N_l}{\partial y} \\ \frac{\partial N_l}{\partial x} & \frac{\partial N_l}{\partial y} \end{pmatrix}$$

Furthermore, stresses are connected to strains via the following formulation

$$\boldsymbol{\sigma} = \boldsymbol{D}\boldsymbol{\epsilon} \tag{2.17}$$

Calculating the displacements of an element j can be done by minimizing the total potential energy, thus the variation with respect to the displacements must be stationary:

$$\delta U = \int \delta\boldsymbol{\epsilon}\boldsymbol{\sigma} dxdy + \int \delta U_j F_j = 0 \tag{2.18}$$

The first integral term above can be rewritten using Equations 2.16 and 2.17, yielding

$$\int \delta\boldsymbol{\epsilon}\boldsymbol{\sigma} dxdy = \int \delta U_j \boldsymbol{B}^T \boldsymbol{D}\boldsymbol{B} dxdy U_j$$

So we end up with

$$\int \delta U_j \boldsymbol{B}^T \boldsymbol{B}\boldsymbol{D} dxdy U_j = -\int \delta U_j F_j$$

$$\boldsymbol{K}_j \mathbf{U}_j = \mathbf{F}_j$$

where $\mathbf{F}_j$ is the vector of external forces and $\boldsymbol{K}_j$ is the elements stiffness matrix

$$\boldsymbol{K}_j = \int \boldsymbol{B}^T \boldsymbol{D} \boldsymbol{B} dxdy \tag{2.19}$$

Similar to the thermal problem it is possible to compute the integral expression 2.19 quite easily by applying appropriate coordinate transformations.

2.4. Interface between two bodies

2.4.1. Contact formulations

So far only situations involving continuously meshed regions have been discussed. In this section we will work on problems with two bodies being in contact with each other. The following explanations are adopted from the book of Zienkiewicz and Taylor [22, Chapter 10.8].

Whenever a contact between two bodies occurs the mathematical equations become highly non-linear and the system stiffness matrix non-symmetrical. Prior to the contact on the edge of the involved bodies boundary conditions are imposed which must be modified as soon as the a they get in contact. Within the framework of the finite element method most of the contact situations can be modeled using the following techniques:

- direct method,
- penalty method or
- Lagrange multipliers.

Furthermore only mechanical contacts will be treated, but the concepts above can be adopted for thermal and electrical contacts as well.

Further it is necessary to find a criterion in order to define when two bodies are in contact and when not. In cases where only small displacements occur and the meshes of the two involved bodies match, the concept of *point to point* contacts may be applied as depicted in Figure 2.7. In this case the definition whether two bodies being in contact or not can be simply defined using the vertical components of two nodes:

$$g = x^s - x^m = (X^m + u^m) - (X^s + u^s) \tag{2.20}$$

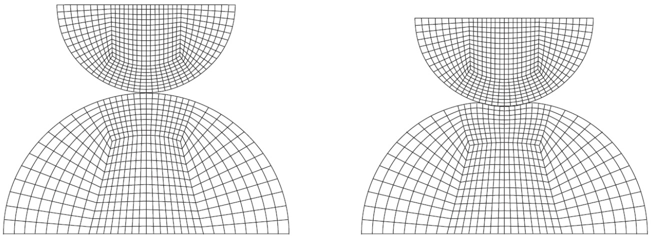

Figure 2.7.: Schematic illustration of two bodies being in contact with matching meshes; from [22]

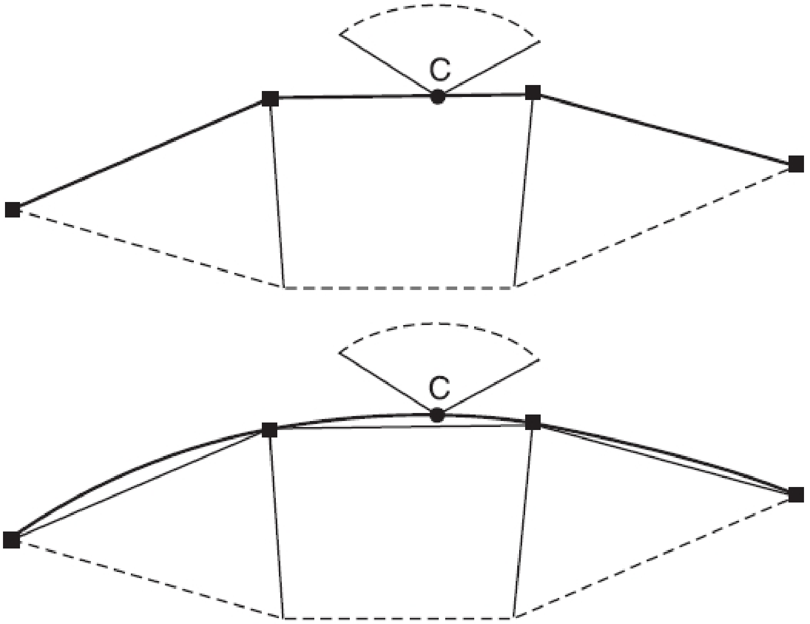

Figure 2.8.: Node to surface contact with linear (upper) or smoothed surface (lower), from [22]

The quantity X denotes the position and u the displacement of the nodes. The superscripts m and s stand for *master* and *slave*, i.e. the boundary nodes of the upper body in Figure 2.7 are called slave nodes and the lower nodes master nodes. So if $g > 0$ no contact occurs and if $g \leq 0$ the bodies are in contact.

In situations where master and slave surface have meshes that mismatch *node to surface* contacts are used. The definition of the contact is in this case somewhat trickier, either the surface is interpolated linearly or it is smoothed as illustrated in Figure 2.8. For the sake of simplicity let us assume a contact problem in two dimensions, then the interpolation can be written as

$$\mathbf{x} = N_\alpha(u)\mathbf{x}_\alpha \tag{2.21}$$

with $\mathbf{x}_\alpha$ being the edge nodes and N_α the according interpolation function. In order to define the distance between a contacting point and the contact surface, it is necessary to find the closest distance between the two considered bodies:

$$f = \frac{1}{2}\left(\mathbf{x}_s^T - \mathbf{x}^T\right)(\mathbf{x}_s - \mathbf{x}) \rightarrow \min \tag{2.22}$$

where u is the horizontal internal coordinate. The vector $\mathbf{x}_s$ is the position of the slave node (point c in Figure 2.8) and $\mathbf{x}$ the master surface expressed using 2.21. The superscript T indicates the transposed vectors of $\mathbf{x}_s$ and $\mathbf{x}$. The expression 2.22 may be minimized using the Newton-Raphson method yielding a parameter u_c. Thus the point on the surface where the distance is minimal can be written using Equation 2.21

$$\mathbf{x}_c = N_\alpha(u_c)\mathbf{x}_\alpha. \tag{2.23}$$

After having formulated the contact definitions it is necessary to impose the displacement of the master nodes to the according slave nodes in order to guarantee contact enforcement. As mentioned in the beginning of this section we will discuss the following possibilities:

Direct method This method is the simplest way of contact enforcement. If the gap between the points $\mathbf{c}_s$ and the master surface (line between points $\mathbf{p}$ and $\mathbf{q}$) is below some limit, the displacements (u, v) of the master nodes $\mathbf{p}$ and $\mathbf{q}$ are imposed to the according slave node $\mathbf{c}_s$ as depicted schematically below:

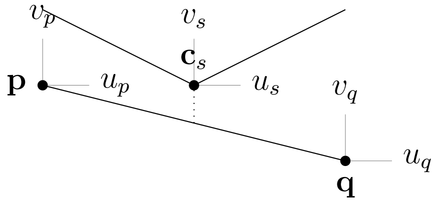

Penalty method Considering the potential U in the variation 2.18, the idea behind the penalty method is to add a term reading

$$U_c = \kappa g^2 \tag{2.24}$$

with a fixed penalty parameter κ. It can be interpreted as a spring constant 'pushing' the slave node out of the master surface.

Lagrangian multipliers Here a similar approach as in the penalty method is used. The additional term to the potential U is

$$U_c = \lambda g \tag{2.25}$$

with λ the Lagrangian multiplier. In contrast to the penalty coefficient in Equation 2.24 the parameter λ itself is an additional unknown variable. Thus the variation of the overall potential reads then as

$$\delta \bar{U} = \delta U + \delta U_c = \delta U + \delta \lambda g + (\delta u^s - \delta u^m)\lambda \tag{2.26}$$

When regarding the variational term 2.26 it is obvious that λ is equivalent to a force restraining penetration.

2.4.2. Friction

The formulations so far have only considered the normal component of contact situations, the tangential components have been assumed to zero describing frictionless contacts. The simplest way to include friction is using the Coulomb condition

$$|t_s| \leq \mu |t_n| \tag{2.27}$$

where t_s and t_n are the tangential and normal traction, respectively. The parameter μ is called the Coulomb friction coefficient, it is a positive dimensionless number. Basically, Equation 2.27 states that points whose tangential traction is lower than the product $\mu|t_n|$ stick. As soon as $|t_s|$ exceeds the Coulomb limit the points slide.

2.4.3. The cohesive zone model

In order to model the failure of an interface between two bodies, a variety of concepts have arisen within the frame work of the finite element method. Basically they can be divided in two groups direct and indirect approaches.

Techniques such as linear elastic fracture mechanics (LEFM), virtual crack closure (VCC) or the J-integral method directly include fracture or damage mechanics. The

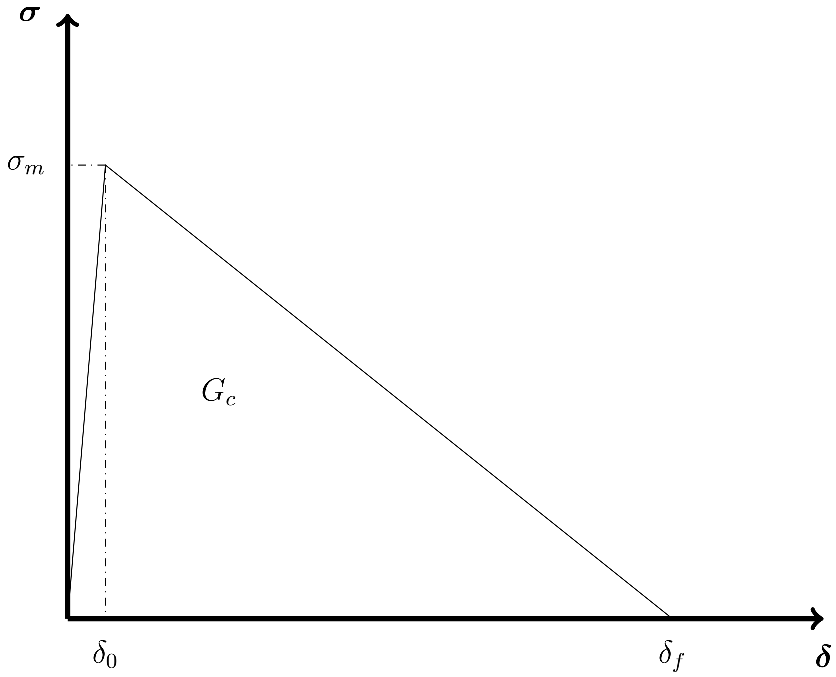

Figure 2.9.: Schematic representation of the traction (σ) separation (δ) law used in the cohesive zone model.

drawback of these procedures is that the initial location of the crack must be known and they exhibit severe difficulties if more than one crack occur simultaneously. This might not be an issue for cases where the locus of the crack and its path is predefined by geometry (e.g. notches) but for general applications this might be inappropriate.

Therefore, different approaches have been made to overcome the aforementioned shortcomings by use of special types of elements based on damage mechanics *indirectly* combined with fracture mechanics [23]. A very popular strategy among those indirect approaches is the *cohesive zone model* first introduced by Barenblatt [24] and later refined by Hillerborg et al [25]. Hillerborg's originally used this model in order to simulate the failure of concrete, it was later extended by Tvergaard et al [26] for ductile materials. The key element of the cohesive zone model is the traction separation law, schematically shown in Figure 2.9. The basic idea of Hillerborg et al was that a crack is assumed to propagate when the stress at the crack tip reaches σ_m. Then the stress does not drop to zero immediately but decreases gradually according to Figure 2.9. As soon as the crack width exceeds δ_f the stress is zero (compare [25, page 775]). The area under the triangle in Figure 2.9 G_c is equivalent to the amount of energy the joint is capable to bear and

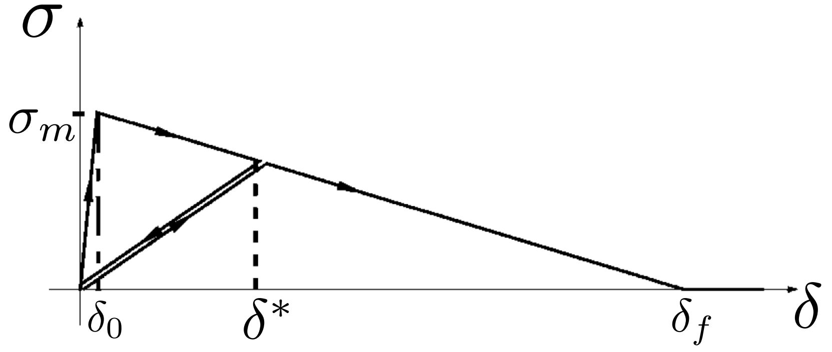

Figure 2.10.: Unloading behavior of the cohesive zone, according to [23].

can be calculated using:

$$G_c = \frac{1}{2}\sigma_m \delta_f. \tag{2.28}$$

The analytical expression for the curve in Figure 2.9 reads as follows:

$$\sigma = \begin{cases} \delta\ k_{\text{init}} & \text{if} \delta \leq \delta_0 \\ \delta\ k_{\text{init}} \frac{\delta_0}{\delta_0 - \delta_f} & \text{if} \delta_0 < \delta < \delta_f \\ 0 & \text{if} \delta \geq \delta_f \end{cases} \tag{2.29}$$

where k_{init} is the initial slope of the curve up to σ_m. In case of decreasing values of δ prior to δ_f the elastic unloading takes place with reduced stiffness (compare Figure 2.10). Regarding Figure 2.9 there are two ways of defining the cohesive behavior:

Energy based Since the area under the curve in Figure 2.9 corresponds to the critical fracture energy the triangle is unambiguously defined by the parameters $k_{\text{init}}, \sigma_{\text{m}}$ and G_c.

Traction Based On the other hand the final displacement δ_f and the fracture energy are linked via Equation 2.28, thus δ_f may be used to define the cohesive potential instead of G_c.

In most problems mixed mode loading occurs, that is a mixture of peeling (mode I) and shearing modes (mode II) can be observed and therefore one has to define appropriate mixing rules. Sometimes mode III failure is taken into account (tearing), too. However according to Camanho et al. [27], there is no reliable failure criterion addressing mode III. Thus it is common practice summarize mode II and mode III energy to an overall shear energy

$$G_{\text{shear}} = G_{II} + G_{III},$$

if mode III loads occur.

In case of the energy based cohesive zone formulation there are two very prominent mixing laws. The *power law criterion* elaborated by Wu and Reuters [28] reads as

$$\left(\frac{G_I}{G_{Ic}}\right)^{\alpha} + \left(\frac{G_{II}}{G_{IIc}}\right)^{\alpha} = 1 \tag{2.30}$$

where G_{Ic} and G_{IIc} are the critical fracture energy rates of mode I and mode II, respectively.

Another criterion, conceived especially for composite materials is the criterion of Benzeggagh and Kean (B-K criterion) [29] yielding

$$G = G_{Ic} + (G_{IIc} - G_{Ic})\left(\frac{G_{II}}{G_T}\right)^{\eta}, \quad \text{with} \quad G_T = G_I + G_{II} \tag{2.31}$$

Finding appropriate values for exponents α and η in Equation 2.30 and 2.31 demands for experimental testing using double cantilever beam (DCB) test for mode I failure and end-notched flexure (ENF) or end loaded split (ELS) test for pure mode II. Using the mixed mode bending (MMB) test it is possible to probe mixed mode fracture [27]. The experimental findings are then plotted in such a manner as in Figure 2.11 and interpolated using expression 2.30 or 2.31 where α and η serve as fitting parameters.

In the context of a displacement based criterion, according to Campilho et al. [30] the mixing behavior my be defined by means of a mixed mode displacement

$$\delta_{\text{m}} = \sqrt{\delta_I^2 + \delta_{II}^2} \tag{2.32}$$

and mixed mode ratio

$$\beta_i = \frac{\delta_i}{\delta_I}, \quad i = I, II. \tag{2.33}$$

Campilho et al. [30] elaborated their mixing relationships for trapezoidal cohesive laws as depicted in Figure 2.12. Such a cohesive model may be used to mimic the failure behavior of ductile materials since damage does not occur immediately but after some 'softening' stage represented by the plateau between δ_1 and δ_2. The constitutive relationship of

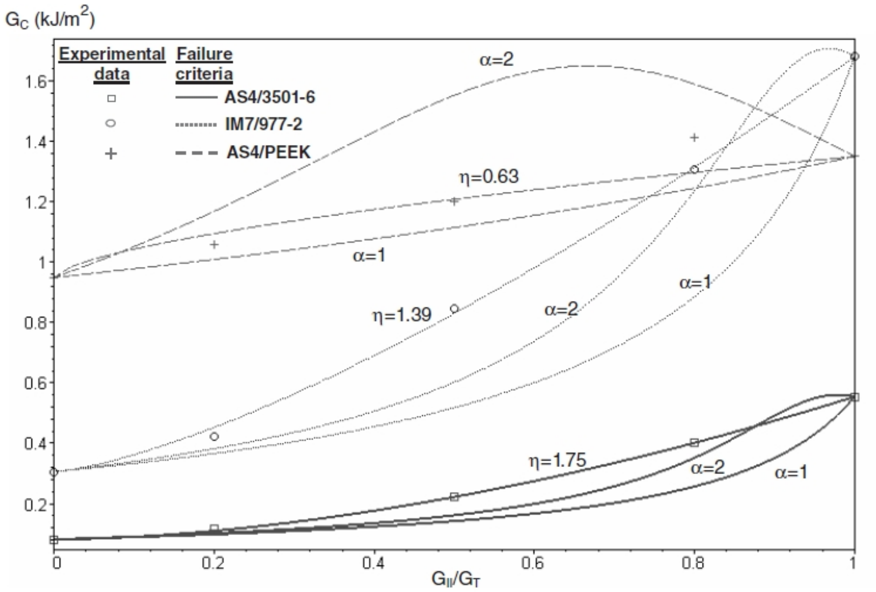

Figure 2.11.: Experimental data of mixed mode testings from Camanho et al. [27]

such interface is then defined as

$$\boldsymbol{\sigma} = \begin{cases} \mathbf{K}\boldsymbol{\delta}_r & \text{if} \quad 0 < \delta < \delta_1 \\ (\mathbf{I}-\mathbf{D})\mathbf{K}\boldsymbol{\delta}_r & \text{if} \quad \delta_1 \leq \delta < \delta_f. \end{cases} \tag{2.34}$$

where the **K** is a diagonal matrix containing the stiffnesses $k_i, i = I, II$, **I** is the identity matrix and **D** the matrix of the damage parameters $d_i, i = I, II$. The damage parameters d_i are defined as

$$d_i = \begin{cases} 1 - \frac{\delta_{1,i}}{\delta_i} & \text{if} \quad \delta_{1,i} < \delta_i < \delta_{2,i} \\ 1 - \frac{\delta_{1,i}(\delta_{f,i}-\delta_i)}{\delta_i(\delta_{f,i}-\delta_{2,i})} & \text{if} \quad \delta_{2,i} \leq \delta < \delta_{f,i}. \end{cases} \tag{2.35}$$

As deduced in detail in Campilho's work [30] it is possible to derive 'mixed values' for the entities δ_1, δ_2 and δ_f

$$\delta_{1\mathrm{m}} = \delta_{1,I}\delta_{1,II}\sqrt{\frac{1+\beta_{II}^2}{\delta_{1,II}^2+\beta_{II}^2\delta_{1,I}^2}} \tag{2.36}$$

$$\delta_{2\mathrm{m}} = \delta_{2,I}\delta_{2,II}\sqrt{\frac{1+\beta_{II}^2}{\delta_{2,II}^2+\beta_{II}^2\delta_{2,I}^2}} \tag{2.37}$$

$$\delta_{f\mathrm{m}} = \frac{2G_{Ic}G_{IIc}(1+\beta_{II}^2) - \delta_{1\mathrm{m}}(\delta_{2\mathrm{m}}-\delta_{1\mathrm{m}})(k_IG_{IIc}+\beta_{II}^2k_{II}G_{Ic})}{\delta_{1\mathrm{m}}(k_IG_{IIc}+\beta_{II}^2k_{II}G_{Ic})} \tag{2.38}$$

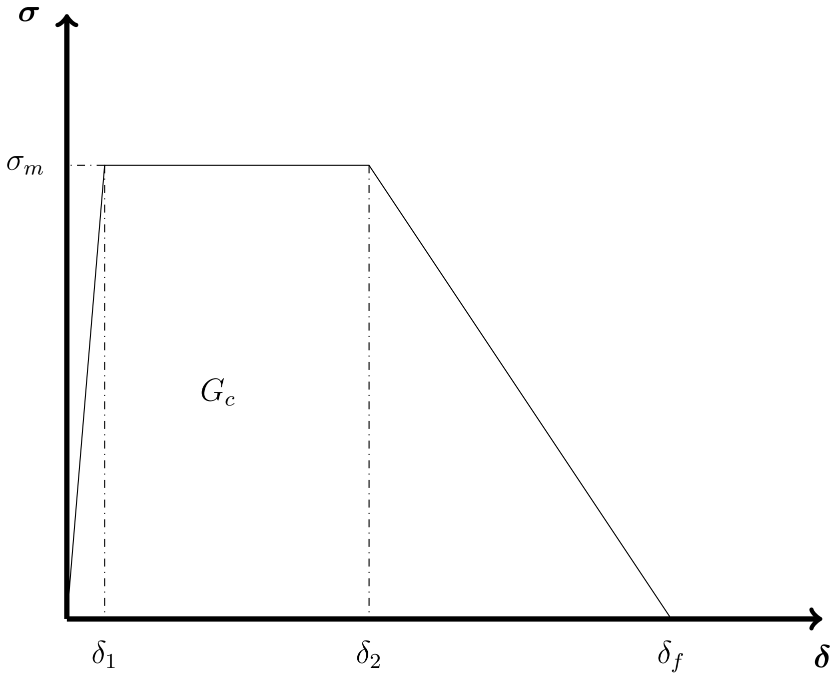

Figure 2.12.: Scheme if a trapezoidal cohesive law.

2.5. The artificial bee colony (ABC) algorithm

The ABC algorithm is an optimization scheme conceived by Karaboga and Basturk [31]. It emulates the behavior of a bee swarm when holding out for food sources. The underlying problem is to find a minimum of a given function $f(\mathbf{x})$

$$f(\mathbf{x}) = \sqrt{\sum_{l=1}^{m} \left(v_l - w_l\left(\mathbf{x}\right)\right)^2} \tag{2.39}$$

with $\mathbf{x}$ being the D-dimensional input vector. The entries v_l in equation 2.39 are the target values (e.g. experimental results) and the entities $w_l\left(\mathbf{x}\right)$ are calculated results (e.g. numerical simulations).

In order to find an optimal input vector $\mathbf{x}$ that minimizes function 2.39, the following steps are conducted.

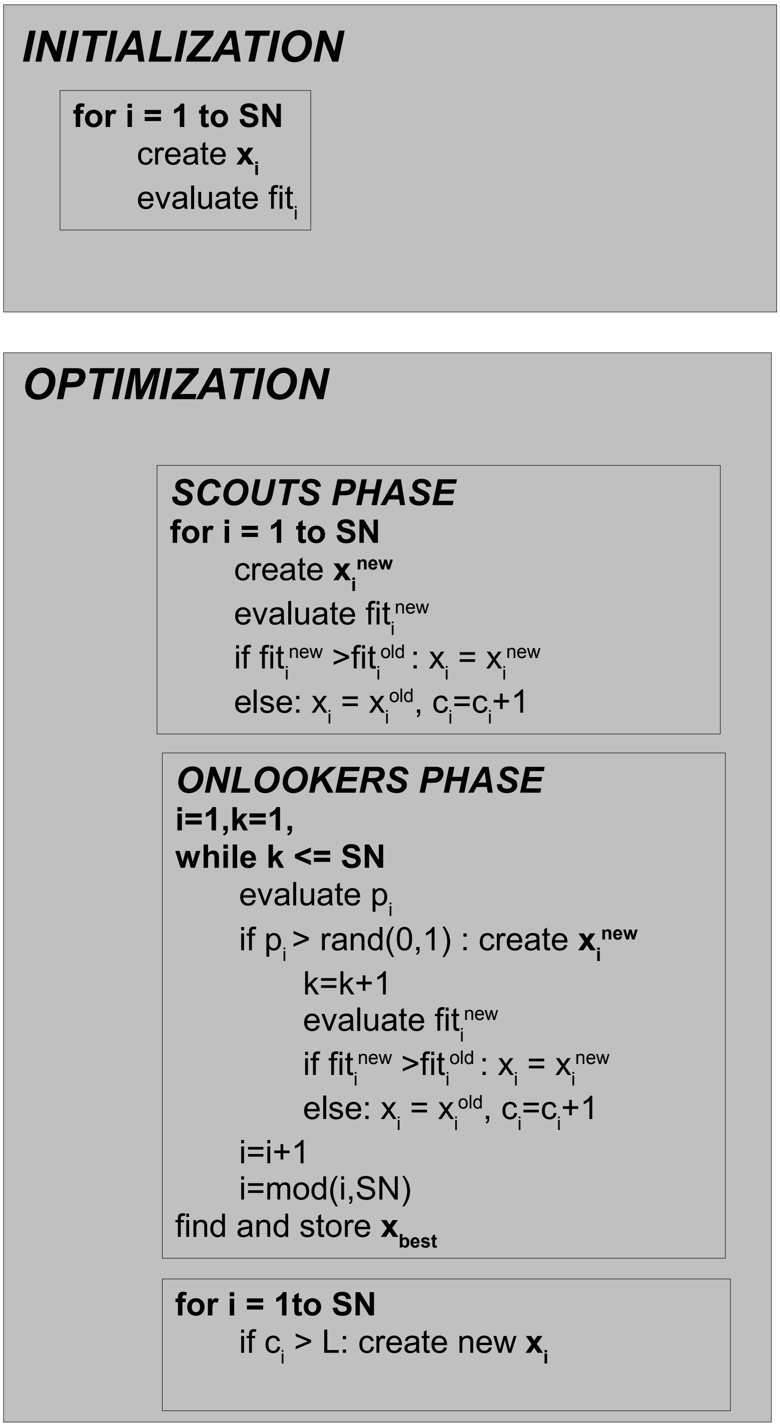

```
INITIALIZATION
    for i = 1 to SN
        create $\mathbf{x}_i$
        evaluate $fit_i$

OPTIMIZATION
    SCOUTS PHASE
    for i = 1 to SN
        create $\mathbf{x}_i^{new}$
        evaluate $fit_i^{new}$
        if $fit_i^{new} > fit_i^{old}$ : $x_i = x_i^{new}$
        else: $x_i = x_i^{old}$, $c_i = c_i + 1$

    ONLOOKERS PHASE
    i=1,k=1,
    while k <= SN
        evaluate $p_i$
        if $p_i >$ rand(0,1) : create $\mathbf{x}_i^{new}$
            k=k+1
            evaluate $fit_i^{new}$
            if $fit_i^{new} > fit_i^{old}$ : $x_i = x_i^{new}$
            else: $x_i = x_i^{old}$, $c_i = c_i + 1$
        i=i+1
        i=mod(i,SN)
    find and store $\mathbf{x}_{best}$

    for i = 1to SN
        if $c_i > L$: create new $\mathbf{x}_i$
```

Figure 2.13.: Schematic representation of the ABC optimization algorithm. The block *OPTIMIZATION* is repeated CN times.

Initialization

1. A set of SN trial input vectors between certain boundaries is created randomly. For the j^{th} element of the input vector we get

   $$x_{ij} = x_j^{\min} + \phi \left(x_j^{\max} - x_j^{\max} \right) \tag{2.40}$$

   with i denoting the number of the parameter set ($i = 1, 2, ..., SN$). The variable ϕ is a random number within the boundaries $[0, 1]$. The quantities $x_j^{\min}$ and $x_j^{\max}$ are the minimum and maximum value allowed for the parameter x_j, respectively. The values for $x_{\min}$ and $x_{\max}$ must be set by the user. After evaluating equation 2.40 for all trial sets one ends up with a matrix of SN rows and D columns.

2. The values of $f(\mathbf{x})$ for all SN sets are evaluated. In order to compare the quality of the parameter sets among each other the following fitness function

   $$\mathrm{fit}_i = \frac{1}{1 + f(\mathbf{x}_i)} \tag{2.41}$$

   is introduced.

After having completed the initialization the parameter set with the best fitness function is stored as $\mathbf{x}_{\text{best}}$. Now the actual optimization begins.

Optimization

1. A new set of parameter $\mathbf{x}_i = (x_{i1}, \ldots, x_{ij}, \ldots x_{iD})$ is generated by use of the routine below:

   $$x_{ij}^{\text{new}} = x_{ij}^{\text{old}} + \phi \left(x_{ij}^{\text{old}} - x_{kj}^{\text{old}} \right), \; i \neq k, \; i \in [1, SN], \; j \in [1, D] \tag{2.42}$$

   with ϕ being a random number in the range of $[-1, 1]$. The index i in the equation above denotes the i^{th} set of parameter. Furthermore k is chosen randomly from the pool of the other parameter sets. If any of the newly generated entities exceeds its boundary it is set to its lower or upper limit, respectively. Then the new set of parameters $\mathbf{x}_i^{\text{new}}$ is evaluated. Subsequently, the fitness function $\mathrm{fit}\left(\mathbf{x}_i^{\text{new}}\right)$ is computed and if $\mathrm{fit}\left(\mathbf{x}_i^{\text{new}}\right) \geq \mathrm{fit}\left(\mathbf{x}_i^{\text{old}}\right)$ the new parameter set is accepted, otherwise it remains unchanged ($\mathbf{x}_i^{\text{new}} = \mathbf{x}_i^{\text{old}}$). This step is called the *scout phase*.

2. As a next step the so called *onlookers phase* applies. In this step parameter sets with a very poor fitness function $\mathrm{fit}\left(\mathbf{x}_i\right) \ll 1$ are modified again. In order to filter those parameter sets having a poor fitness function, the quantity p_i is defined for each set $\mathbf{x}_i$:

   $$p_i = \frac{\mathrm{fit}_i}{\sum_{l=1}^{SN} \mathrm{fit}_l}. \tag{2.43}$$

   A set of parameters is changed according to Equation 2.42, if $p_i < \rho$, ρ being a random number of the interval $[0, 1]$. Thus, parameter sets with a good fitness function are more unlikely to be changed than those having a poor one. Considering Equation 2.43 it becomes evident why the fitness function has been introduced.

3. After the scouts and onlookers phase it is checked if any of the newly improved parameter sets is better than $\mathbf{x}_{\mathrm{best}}$. If this is the case, $\mathbf{x}_{\mathrm{best}}$ is updated.

4. Every time a newly generated set of parameters is rejected in the steps 1 and 2, a counter is increased by one. If the counter of a set of parameter exceeds a certain user defined limit L a new parameter set is created as follows:

   $$x_{ij}^{\mathrm{new}} = x_j^{\mathrm{min}} + \varphi\left(x_j^{\mathrm{max}} - x_j^{\mathrm{min}}\right),\ \varphi \in [0, 1] \tag{2.44}$$

   were the quantity φ is chosen randomly for every x_j. In other words, every set of parameter that failed to improve for L times is replaced by a new one between the lower and the upper limit according to Equation 2.44.

These steps are repeated CN times.
In Figure 2.13 the ABC algorithm is depicted schematically.

3. Experimental investigations

In the following chapter experimental investigations of pin structures are described. The first part will handle the investigations concerning single pins on several base materials. Further we will examine the influences of the CMT process on the mechanical performance of the base material. In this context we also compare the influence of CMT and EBW pins on the base material.

3.1. Investigations on single pins

In order to reveal the microstructure of a pin we conducted metallographic investigations, such as cross section polishes and hardness measurements.

3.1.1. Austenitic stainless steel

The first material we focused on was austeitic stainless steel of the grade AISI 304 on which we welded pins using AISI 308 filler material. The chemical composition is summarized in Table 3.1. In Figure 3.1a micrographical cross sections of such pins are shown. Based on such images as Figure 3.1b we measured the dimensions (height, width, ...) of the three different kind of pins. The result are listed in Table 3.2. These values were then used in order to set up the FE mesh for the simulations.

In order to get a deeper insight on the failure mechanisms during the shaping stage we made electron microscope images of the pin tips (Figure 3.2). Those images revealed that even in the case of pike pins (Figure 3.2c) the very top of the pin had been molten during the shaping stage.

Table 3.1.: Chemical composition of AISI 304 and AISI 308 in mass %

	C	**Si**	**Mn**	**Cr**	**Ni**
AISI 304	≤ 0.05	0.5	1.4	18.5	9.5
AISI 308	≤ 0.02	0.8	1.7	20.0	10.2

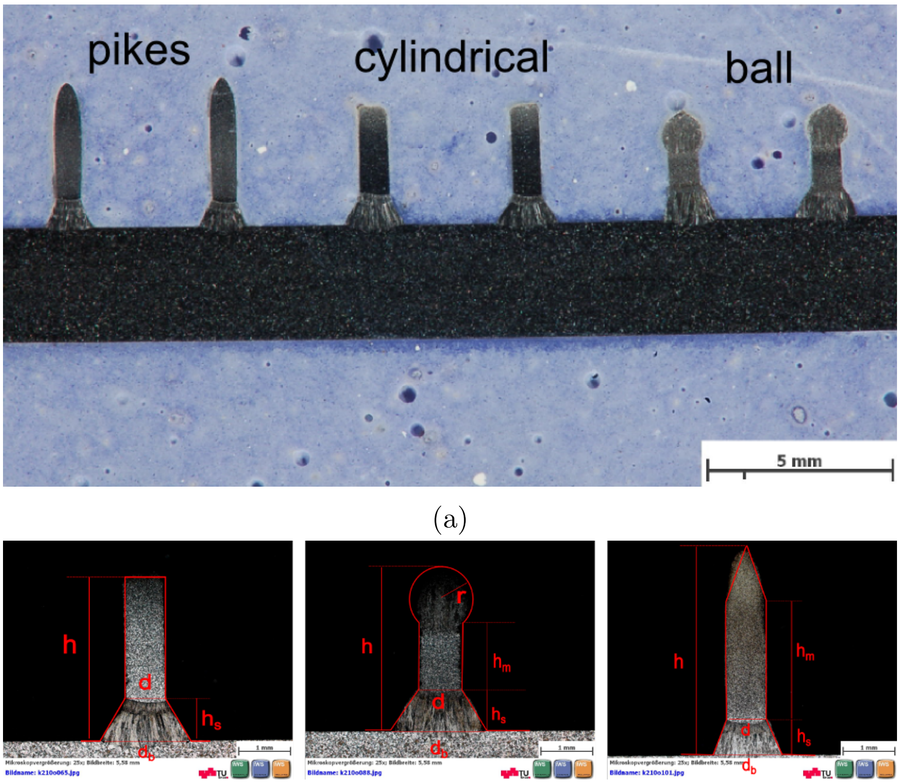

(a)

(b)

Figure 3.1.: Micrographs of stainless steel pins.

Table 3.2.: Geometrical dimensions of austenitic stainless steel pins. The values were averaged from 5 samples of each kind of pin.

h ... overall height
h_s ... socket height
h_m ... height of the middle section (pin and ball pins only)
d_b ... base diameter
d ... pin diameter
r ... radius of the ball head

	h (mm)	**h_s (mm)**	**h_m (mm)**	**d_b (mm)**	**d (mm)**	**r (mm)**
cylindric	3.23 ± 0.05	0.7 ± 0.1	-	1.61 ± 0.08	0.82 ± 0.04	-
ball	3.03 ± 0.07	0.82 ± 0.05	1.1 ± 0.1	1.6 ± 0.1	0.66 ± 0.09	0.56 ± 0.04
pike	4.05 ± 0.07	0.65 ± 0.08	2.4 ± 0.2	1.3 ± 0.1	0.66 ± 0.09	-

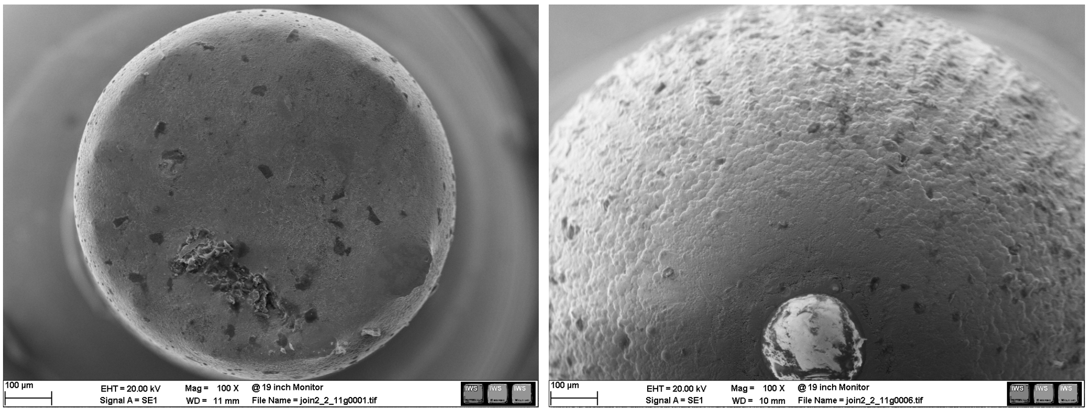

(a) cylindric

(b) ball

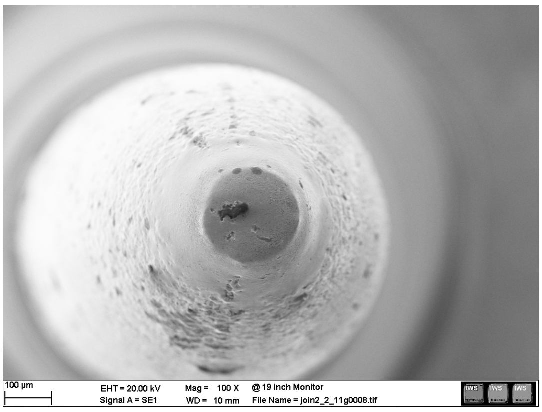

(c) pike

Figure 3.2.: Electron microscope images of pin tips.

3.1.2. Aluminum

Since aluminum alloys are of special interest in the automotive industry we investigated pins made of AlSi5 filler wire welded on a 6XXX series base material. For a detailed chemical composition see Table 3.3 and 3.4 It turned out that the surface treatment prior to welding has a crucial impact on the arc stability and consequently on the weld's quality. These issues were elaborated by the author of this thesis in a work at the ICAA in Pittsburgh,PA USA [32].

Table 3.3.: Chemical composition of AL 6xxx alloys in mass %

Si	**Fe**	**Cu**	**Mn**	**Mg**	**Cr**	**Zn**	**Ti**
≤ 1.50	≤ 0.50	≤ 0.30	≤ 0.80	≤ 1.00	≤ 0.15	≤ 0.30	0.25

Table 3.4.: Chemical composition of the AlSi5 filler wire in mass %

Si	**Fe**	**Mn**	**Ti**
5	≤ 0.40	≤ 0.20	≤ 0.1

As shown in Figure 3.3, pins attached to an untreated surface exhibit poor wetting and therefore poor fusion of the pin to the plate. Several examples dealing with these problems discussed above can be found in literature, e.g. in [33]. Since the time for joining the filler material to the base material within a single pin forming process is in the range of some 20 ms, the oxide layer has to be removed prior to the actual welding. The specimens investigated below were manufactured at Fronius International in Wels, Austria and afterwards we conducted metallurgical investigations.

The connection of the pin to the plate shows three significant defects:

- poor wetting,
- high porosity and
- the central axis of the pin is shifted with respect to the weld point.

Those deficiencies originate from impurities, such as oxide layers or other coatings on the aluminum surface. The asymmetric shape of the pin base suggest arc instabilities during the heating stage.

In order to overcome the problems described above, several measures were taken. Figure 3.4 shows a micrograph of a pin welded on a surface being chemically cleaned using a

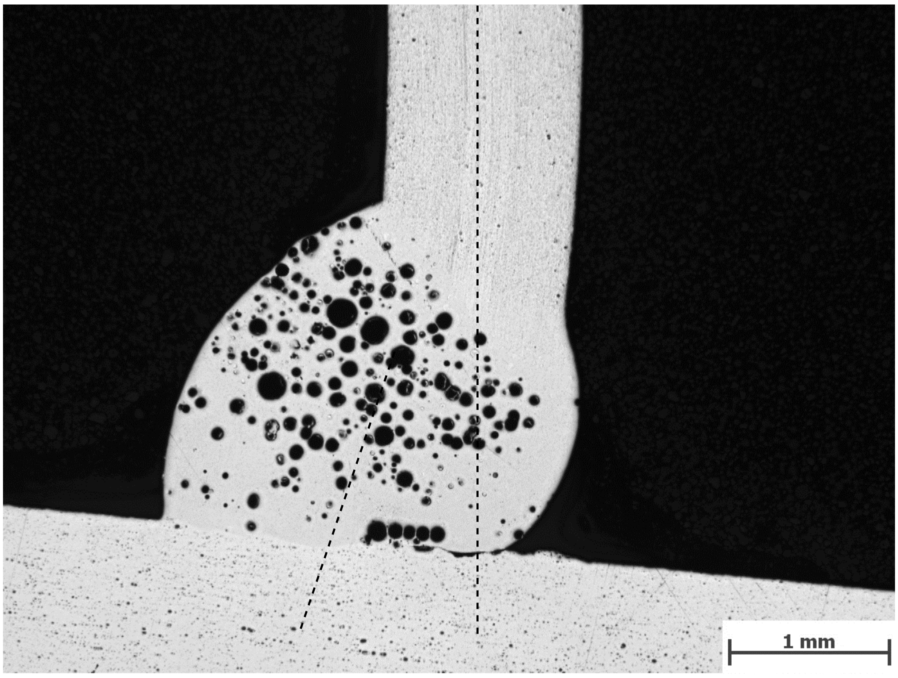

Figure 3.3.: Micrograph of an aluminum pin-plate interface at an untreated surface.

commercial cleaning spray prior to welding. This pretreatment considerably reduces the porosity at the base, nevertheless the poor wetting is still evident.

Further improvements were achieved by treating the welding area using a laser. In doing so, the spot of the base material where the pin was placed had been preheated by the laser. Additionally, the laser was active during the heating stage. The used laser was Nd:YAG laser with a wavelength of 1064nm (780 W), the angle of incidence with respect to the vertically fed wire was 34°. Figure 3.5 shows micrographs of pins placed with the aid of an additional laser. The images of Figure 3.5 clearly reveal, that the wetting improves with the use of a laser. Furthermore the pretreated samples showed enhanced dilution at the plate-pin interface. However, combining the two introduced measures by first cleaning the surface and subsequently activating the surface by means of a laser does not further improve the result compared to the application of laser alone.

Anyhow, the problem of the misalignment of the pin's central axis and the socket's center line still exists even after pretreating the substrate's surface using laser.

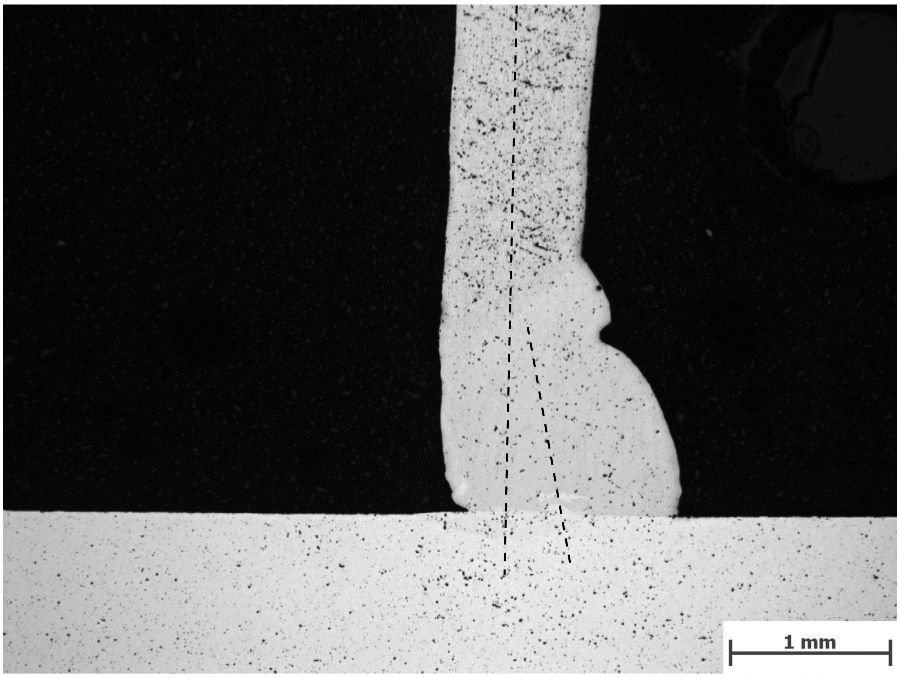

Figure 3.4.: Micrograph of an aluminum pin-plate interface at a surface treated with a commercial cleaning agent.

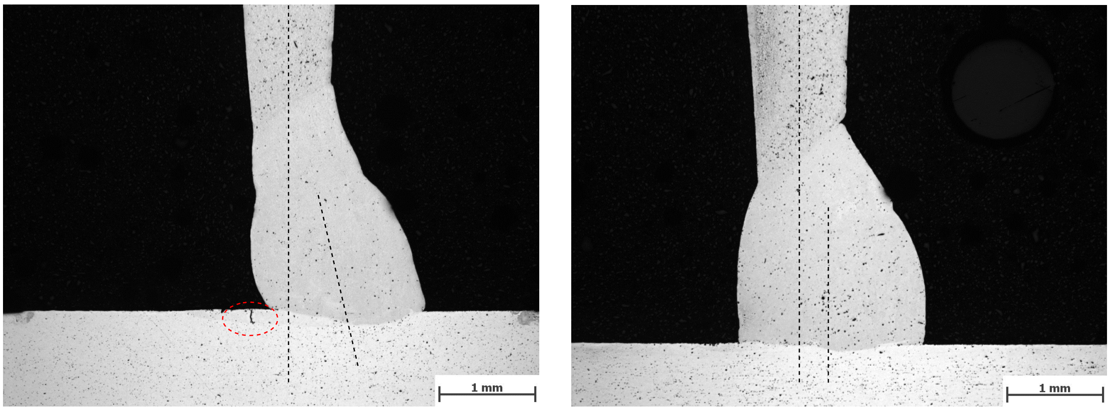

(a)

(b)

Figure 3.5.: Micrographs of aluminum pin-plate interfaces at a cleaned surface (a) and an untreated surface (b). The pins were welded using an additional laser prior to welding and during the heating phase

3.1.3. Drop by drop pins

A second drawback in the case of aluminum pins is that lowest achievable height lays around 3 mm. For practical applications such as in the automotive industry pins with a height of 2 mm or even lower are desired. Furthermore, pressing high pins in carbon

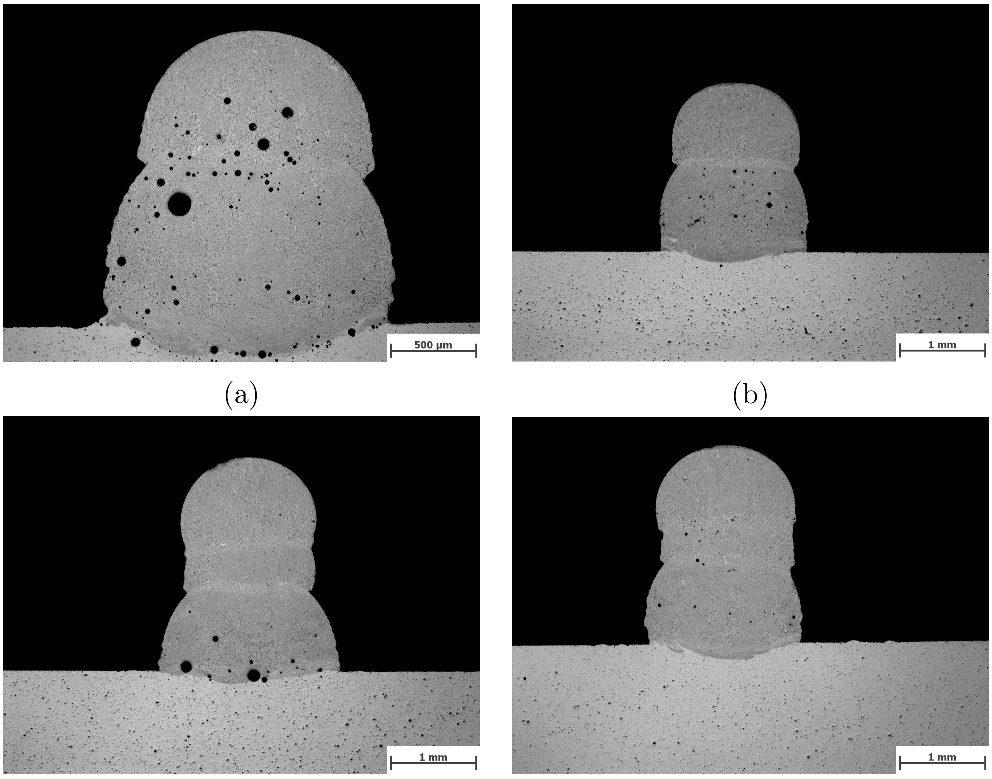

(a) (b) (c) (d)

Figure 3.6.: Cross sections of drop by drop pins on a 6xxx series base material.

fiber mats turned out to be unfeasible for high aluminum pins being too soft. The main limiting factor when it comes to low heights is the good electric conductivity of aluminum. Thus, during the shaping stage (compare Chapter 1) the wire does not heat up at a distinct point. By pulling the wire backwards it fails right at the outlet of the contact tube.

One strategy to overcome these deficiencies is to build the pins drop by drop. In contrast to the common CMT process as described in Chapter 1 the pin is not the residual of the filler material but it is built drop by drop. Figure 3.6 micorgraphs of pins on a 6xxx substrate. The pictures 3.6a and 3.6b show quite pins built of two drops, the pins in 3.6d and 3.6c of three. It is obvious that the quality and the shape of the pin vary significantly from one another. The pictures 3.6a and 3.6c show quite massive pores, while the pins in pictures 3.6b and 3.6d hardly exhibit pores.

3.2. Changes of the base material due to the heat input of pin welding

In order to characterize the mechanical behavior of an actual pin reinforced joint we investigated the welding process' influence on the base material. The aim of the following investigations was to find out if the heat input due to pin welding has any influence on the mechanical properties of the base material. In doing so, we conducted tensile tests of the following material:

- Austenitic stainless steel (AISI 304)
- Aluminum 6xxx series
- Galvanized steel of the type DX54
- Micro alloyed steels HC260LA and HC420LA

On the specimens, as depicted in Figure 3.7, we placed one, two and three rows of four pins at a distance of 5 mm from each other (see Figure 3.8). Except for the aluminum alloys[1] we chose cylindric pins. For reference we conducted tensile tests of untreated specimens.

The experiments were executed using a Zwick/Roell testing machine. The samples were tested at a speed of 1 mm/min, up to a displacement of 1.5 mm the elongation was recorded using a probe attached directly to the sample within the welding area. Further displacements were determined from the jaws' movement. The varying samples' geometry was due to the different sizes of the original plates.

---

[1] In the case of aluminum alloys only on kind of shape is possible.

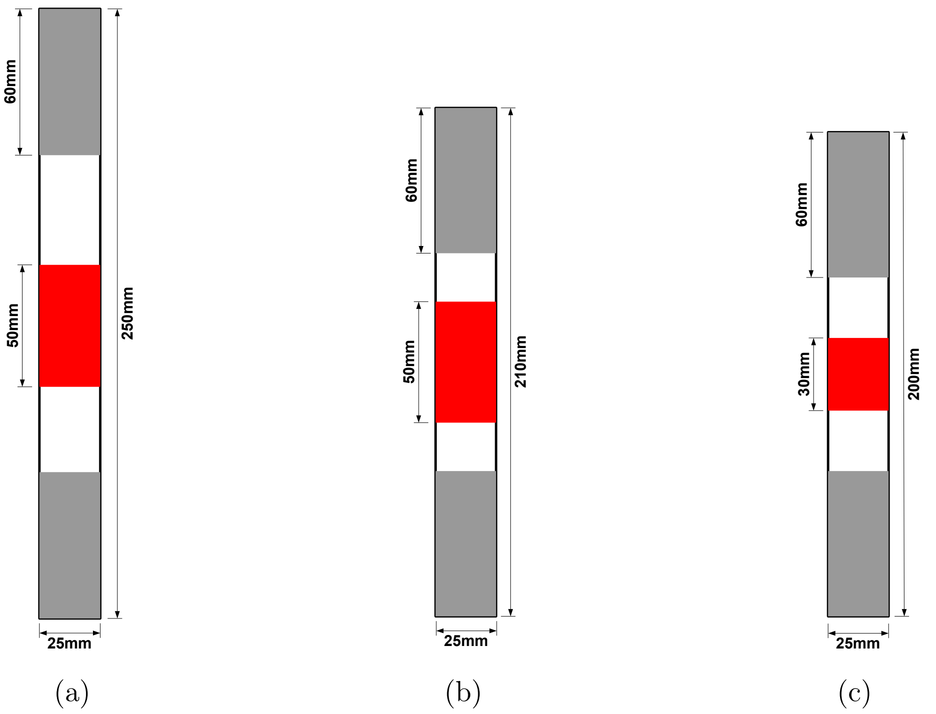

(a) (b) (c)

Figure 3.7.: Geometry of the specimens for tensile testing. Geometry (a) was used for stainless steel (d = 1.00 mm) and aluminum alloys (d = 2.50 mm), geometry (b) for DX54 (d = 0.75 mm) nd geometry (c) for HC260LA and HC420LA (d = 2.00 mm).The red area marks the region where pins were located, at the gray region the specimens were clamped in the testing machine.

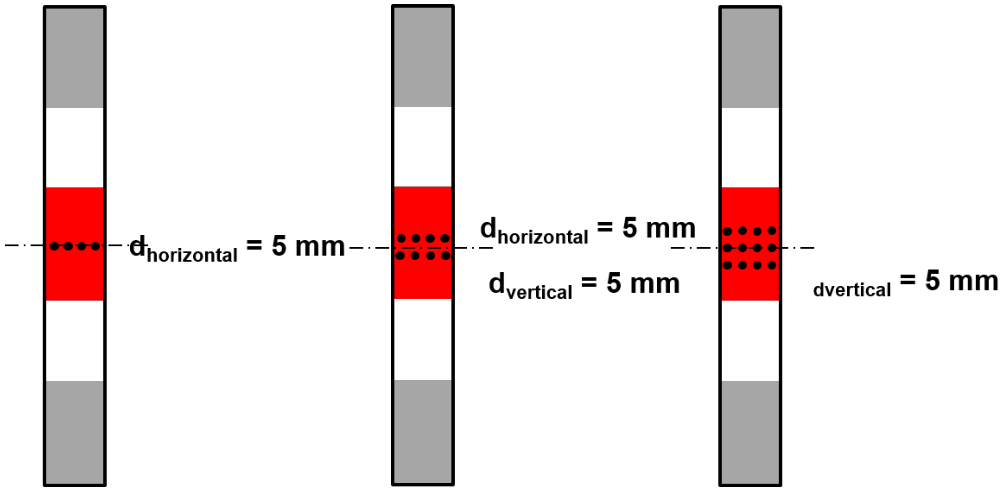

Figure 3.8.: Schematic representation of the investigated pin configurations

3.2.1. Stainless steel

In the case of stainless steel we conducted at least four tests for each configuration. Figure 3.9 shows the stress - strain curves obtained from the tensile tests. In Figure 3.10 the tensile stresses and strains are extracted separately and depicted with respect to the number of pins. It reveals that there is no significant change in tensile strength and that the maximum strain shows massive deviation. Only the specimens with two pin rows show a little drop of the braking strain but still within the error margins. A look on the fracture images in Figure 3.11 shows that the fracture takes place outside the welding zone within the base material leading to the conclusion that the heat input due to pin welding has no or hardly any influence on the base material. Table 3.5 summarizes the results of the tensile tests, both with and without pins, performed with stainless steel. Regarding the specimen with two pin rows, one can observe a relative error fo 40 %.

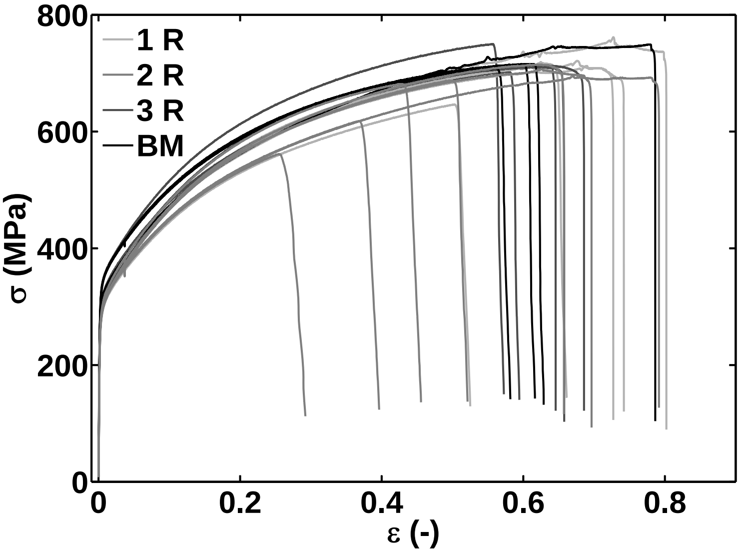

Figure 3.9.: Stress - strain curves of the stainless steel samples.

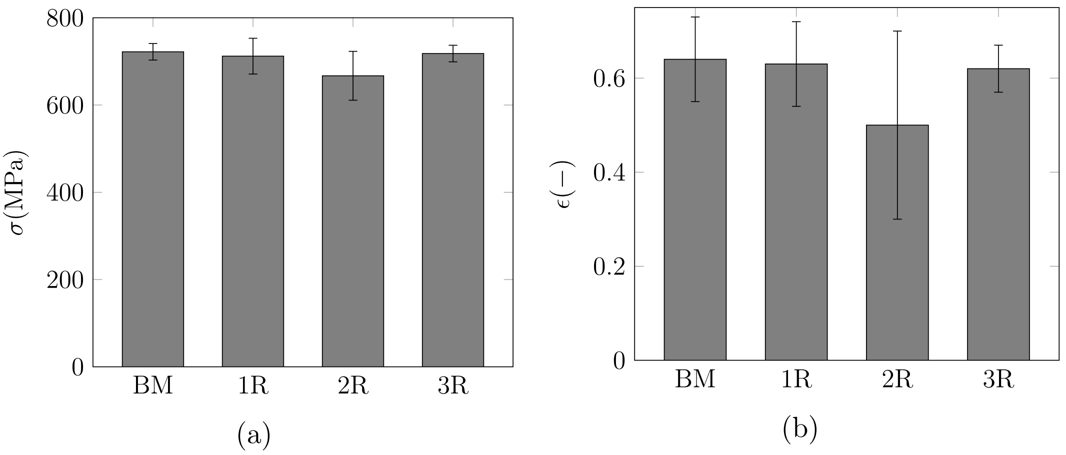

Figure 3.10.: Histograms of the ultimate tensile stresses (a) and fracture elongation (b) of stainless steel samples

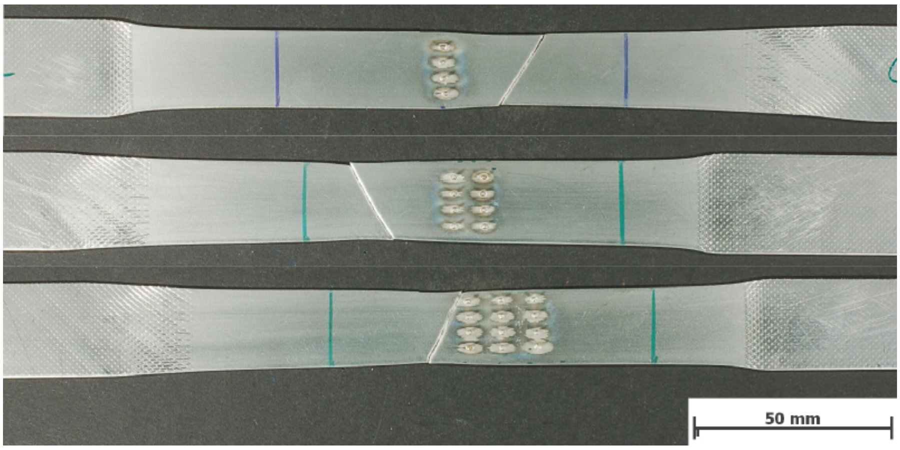

Figure 3.11.: Fracture images of the stainless steel samples with one, two and three rows of pins

Table 3.5.: Averages of rupture strain (ϵ) and fracture toughness (σ) of stainless steel samples with and without pins; n denotes the number of specimens.

	$\boldsymbol{\epsilon}$**(−)**	$\boldsymbol{\Delta\epsilon}$**(−)**	$\boldsymbol{\Delta\epsilon_{\text{rel}}}$**(%)**	$\mathbf{R_m}$**(MPa)**	$\mathbf{\Delta R_m}$**(MPa)**	$\boldsymbol{\Delta\sigma_{\text{rel}}}$**(%)**	**n**
BM	0.64	0.09	14	722	19	2.6	4
1 R	0.63	0.09	14	712	41	5.8	5
2 R	0.50	0.20	40	667	56	8.4	7
3 R	0.62	0.05	8	718	19	2.6	5

3.2.2. Steel - DX54

The chemical composition of the galvanized steel DX54 is presented in Table 3.6. The specimen for this material were a little different than those of stainless steel and aluminum (compare Figure 3.7). The stress strain curves are depicted in Figure 3.12, which reveals that attaching pins to the base material apparently does not have an influence on the mechanical performance. This is also evident in Figure 3.13, showing the tensile strength and ultimate strain, which remains virtually unchanged. Table 3.7 lists the averaged stress and strain values and their standard deviations. In the course of these investigations we found two specimens where the fracture line diagonally crossed the zone of pins as depicted in Figure 3.15. In contrast, in all other samples the breaking happened outside the pin area (see Figure 3.14). In Figure 3.12 the stress strain curves of the two samples of Figure 3.15 are highlighted. However, they do not show a significantly different behavior than the other curves.

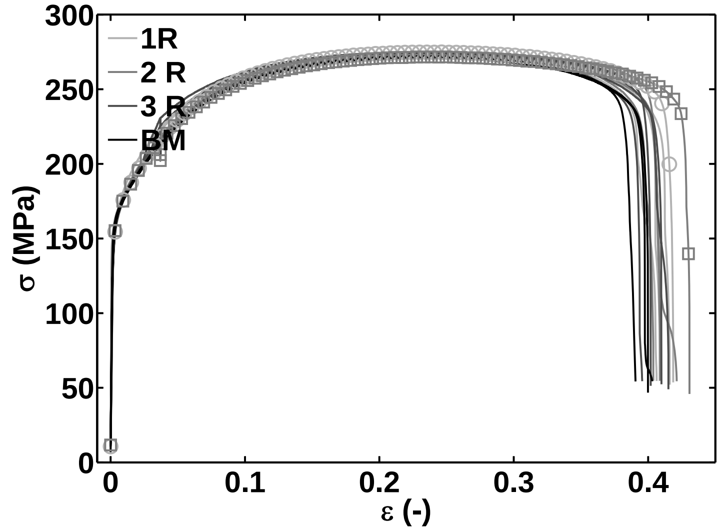

Figure 3.12.: Stress strain diagram of DX54 specimens with different amounts of pins. The curve marked with circles corresponds to the sample of Figure 3.15a the curve with squares to Figure 3.15b

Table 3.6.: Chemical composition of DX54 in mass %

C	**Mn**	**Cr**	**Ni**	**Ti**	**Al**
0.0018	0.11	0.02	0.07	0.051	0.041

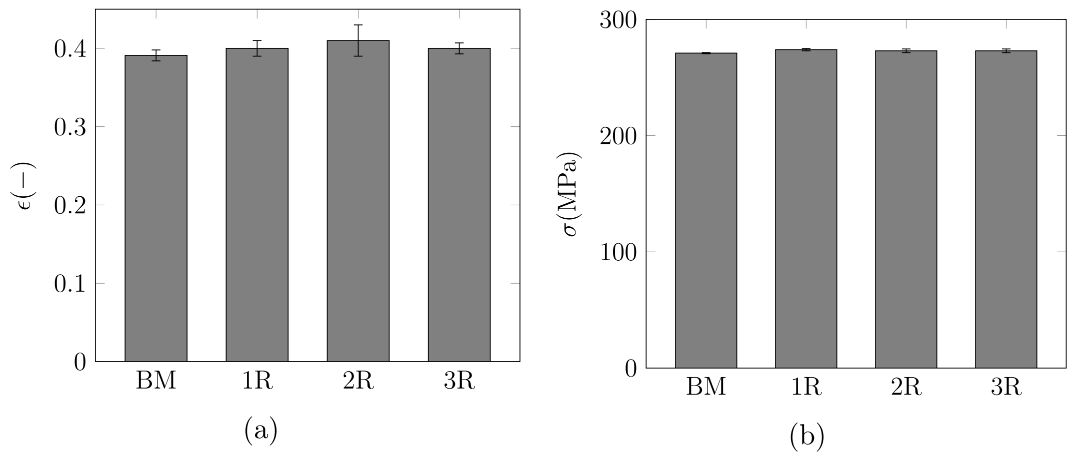

Figure 3.13.: Ultimate strain (a) and tensile strength (b) of the different pin configurations on DX54 plates

Table 3.7.: Averages of ultimate strain (ϵ) and tensile strength (R_m) and their standard deviations of DX54 specimens; n is the number of tested specimens

	$\epsilon(-)$	$\Delta\epsilon(-)$	$\Delta\epsilon_{rel}(\%)$	R_m (MPa)	ΔR_m (MPa)	$\Delta R_{m,rel}$ (%)	n
BM	0.391	0.007	1.8	271	0.5	0.2	5
1 R	0.400	0.010	2.5	274	1.0	0.4	5
2 R	0.410	0.010	2.4	273	1.6	0.6	5
3 R	0.400	0.007	1.8	273	1.5	0.5	5

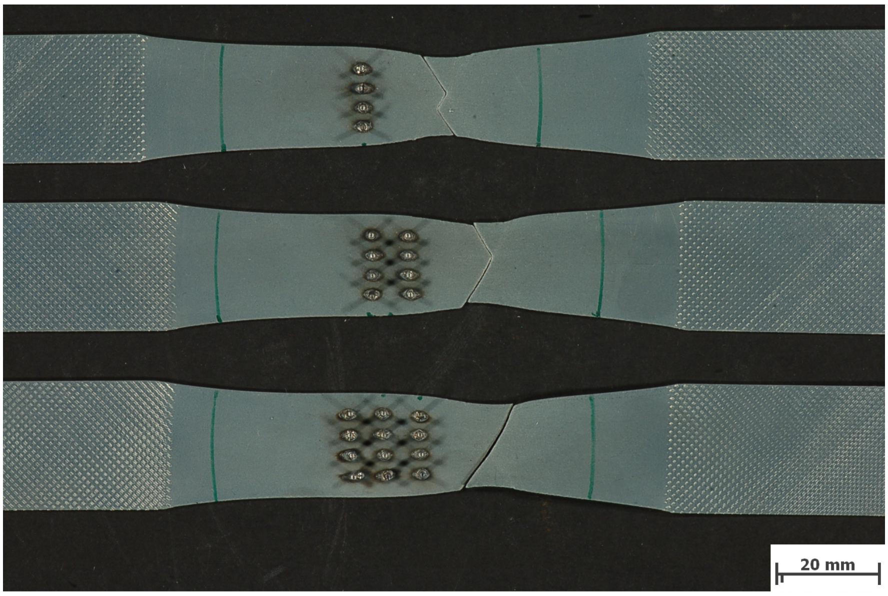

Figure 3.14.: Fracture patterns of the DX54 samples.

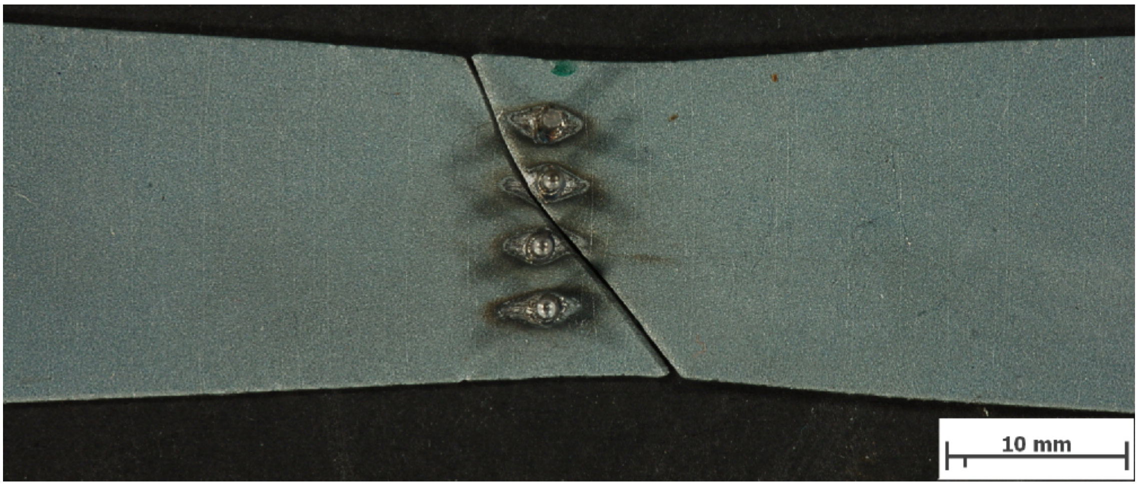

(a)

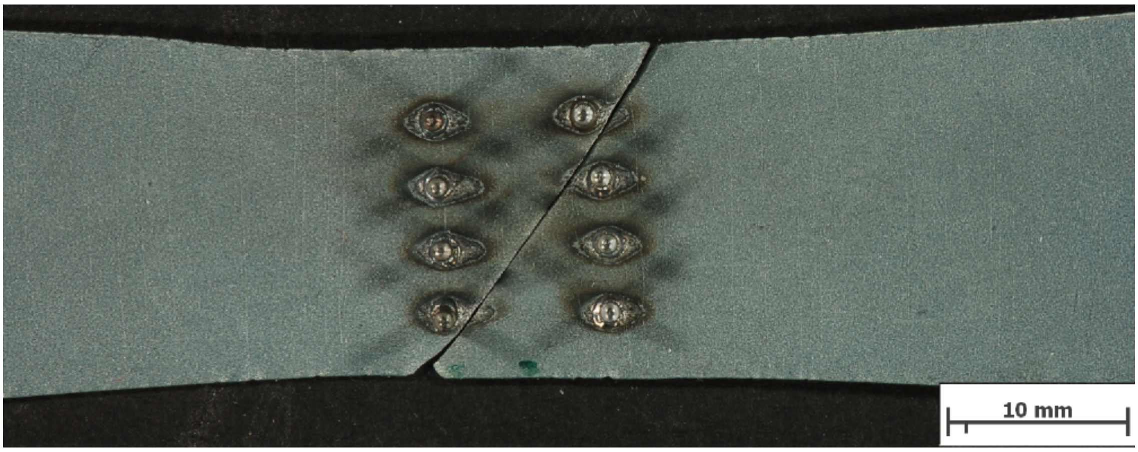

(b)

Figure 3.15.: Special fracture patterns crossing the pin zone in DX54 samples. The stress strain curve of sample (a) is marked with circles and the curve of sample (b)with squares in Figure 3.12

3.2.3. Micro alloyed steel HC260LA/HC420LA

The geometry of those specimens differed from the previous ones as far as the overall length is concerned. We performed four measurements for each pin configuration and the blank samples. Table 3.8 gives the alloying constituents of those two steels

Table 3.8.: Chemical composition of HC260 and HC420 in mass %

	C	**Mn**	**Si**	**Cr**	**Ni**	**Mg**	**Ti**	**P**	**Al**
HC260	0.0430	0.29	0.01	0.03	0.016	-	0.001	0.010	0.048
HC420	0.084	1.05	0.24	0.02	0.012	-	0.001	0.012	0.054

In Figure 3.16 the stress strain curves of the HC260LA and HC420LA samples are shown. In both cases the curves of all pinned and blank samples are almost congruent, there is only a slight variation of the ultimate strain. In the case of HC420LA this variation is a little more distinct, which is illustrated by the slight larger error bars in Figure 3.18a compared to 3.17a. The tensile strength on the other hand does not seem to experience any impact from the welding process at all (see Figures 3.18b and 3.17b).
In Table 3.9 and 3.10 the findings described above are summarized again. Eventually, Figure 3.19 shows fractured specimens of HC420LA. The fracture line is clearly out of the welding zone. The fracture pattern of HC260LA is very similar to that in Figure 3.19 and therefore it is not shown separately.

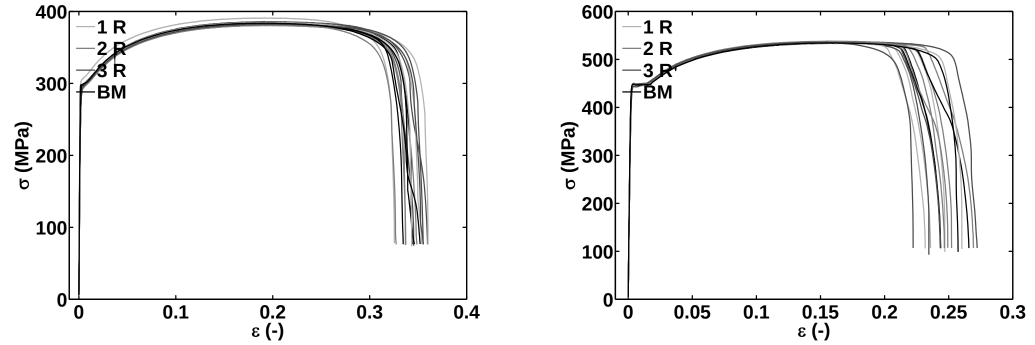

(a) HC260LA (b) HC420LA

Figure 3.16.: Stress strain curves of HC260LA and HC420LA

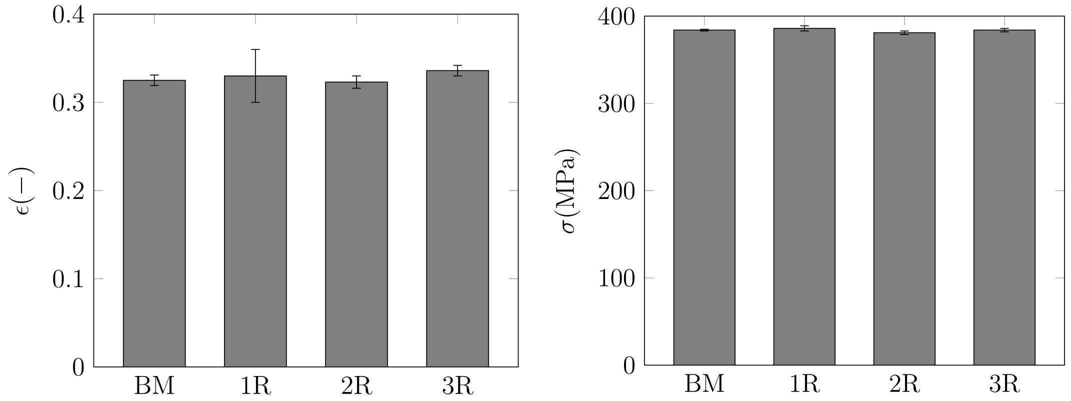

(a) (b)

Figure 3.17.: Histograms of the ultimate strain (a) and tensile strength (b) of HC260LA.

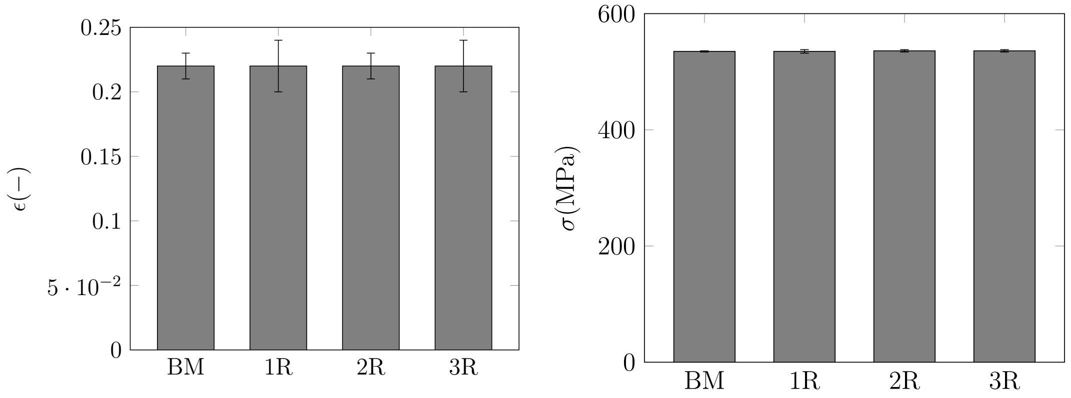

(a) (b)

Figure 3.18.: Histograms of the ultimate strain (a) and tensile strength (b) of HC420LA.

Table 3.9.: Averaged values of ultimate strain (ϵ) and tensile strength (σ) of HC260LA with n being the number of samples

	$\boldsymbol{\epsilon(-)}$	$\boldsymbol{\Delta\epsilon(-)}$	$\boldsymbol{\Delta\epsilon_{\mathrm{rel}}(\%)}$	$\mathbf{R_m(MPa)}$	$\mathbf{\Delta\ R_m(MPa)}$	$\mathbf{\Delta\ R_{m,rel}(\%)}$	**n**
BM	0.325	0.006	1.8	384	1	0.3	4
1 R	0.330	0.030	9.1	386	3	0.8	4
2 R	0.323	0.007	2.2	381	1	0.3	4
3 R	0.336	0.006	1.8	384	2	0.5	4

Table 3.10.: Averaged values of ultimate strain (ϵ) and tensile strength (σ) of HC420LA

	$\boldsymbol{\epsilon(-)}$	$\boldsymbol{\Delta\epsilon(-)}$	$\boldsymbol{\Delta\epsilon_{\mathrm{rel}}(\%)}$	$\mathbf{R_m(MPa)}$	$\mathbf{\Delta\ R_m(MPa)}$	$\mathbf{\Delta\ R_{m,rel}(\%)}$	**n**
BM	0.22	0.01	4.5	535	1	0.2	4
1 R	0.22	0.02	9.1	535	3	0.6	4
2 R	0.22	0.01	4.5	536	2	0.4	4
3 R	0.22	0.02	9.1	536	2	0.4	4

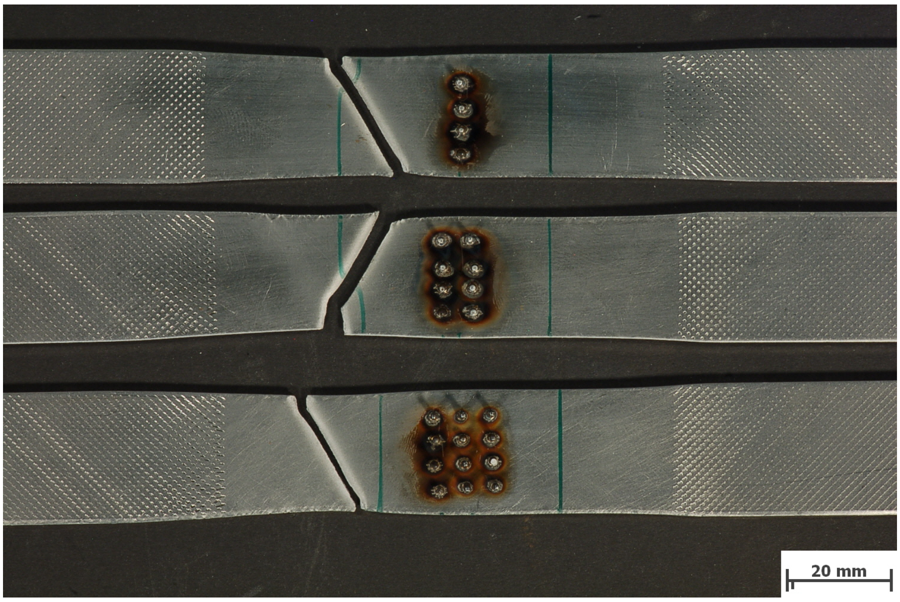

Figure 3.19.: Fracture image of HC420LA specimens.

3.2.4. Aluminum alloys

Within the framework of our investigations of aluminum alloys of the 6xxx series we compared the influence of three different welding processes on the base material's mechanical performance:

- the classic CMT process
- a modified version of it (drop by drop see Section 3.1.3)
- electron beam welding (Section 2.2).

Classic CMT pins

In a first series of experiments we investigated the impact of classic CMT pins being placed on an alloy of the 6xxx series. Figure 3.20 shows the stress strain curves of the pinned and blank samples and in Table 3.12 the ultimate stresses and fracture elongations are listed. It turned out that the ultimate strain is lowered at the samples with pins while the tensile strength remains more or less unchanged. This fact becomes more evident when looking at Figure 3.21. The fracture elongation level drops when pins are attached, but this drop seems to be independent of the number of pins. In contrast to the materials examined so far, the fracture line of the aluminum samples crosses the region where the pin had been attached as depicted in Figure 3.22.

Table 3.11.: Averages of ultimate strain (ϵ) and tensile strength (σ) of AA6xxx with classical CMT pins

	$\boldsymbol{\epsilon}(-)$	$\boldsymbol{\Delta\epsilon}(-)$	$\boldsymbol{\Delta\epsilon_{\mathrm{rel}}}(\%)$	$\mathbf{R_m(MPa)}$	$\mathbf{\Delta\ R_m(MPa)}$	$\mathbf{\Delta\ R_{m,rel}}(\%)$	**n**
BM	0.252	0.002	1	255	5	2.0	4
1R	0.180	0.030	17	254	6	2.4	6
2R	0.170	0.020	12	251	6	2.4	4
3R	0.180	0.020	11	250	4	1.6	4

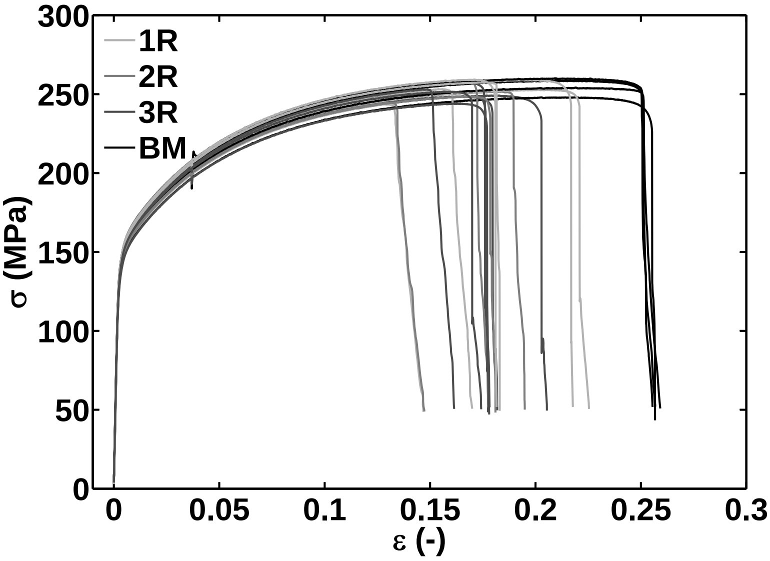

Figure 3.20.: Stress strain curves of aluminum samples of the 6xxx series with different amount of pins.

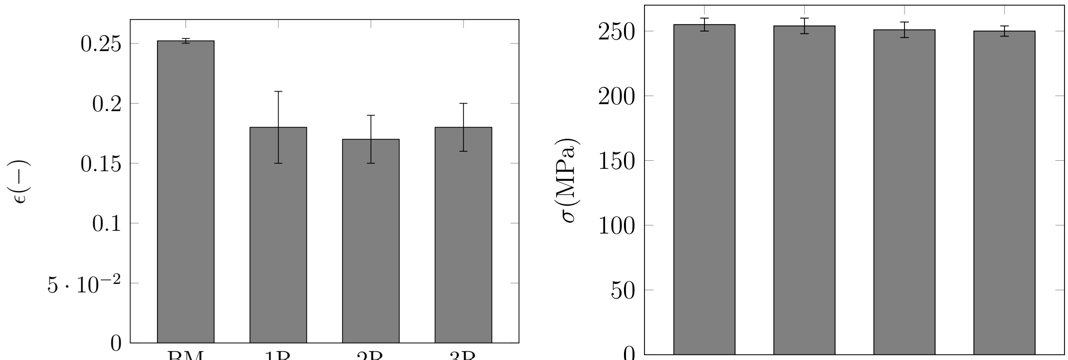

(a)

(b)

Figure 3.21.: Histograms showing the fracture elongation (a) and tensile strength (b) of Al 6xxx alloys with classic CMT pins.

Figure 3.22.: Fracture patterns of AA6xxx alloy samples with classic CMT pins

3.2.5. EBW vs drop by drop pins

In order to investigate the weakening of the base material due to the EBW welding, Tändel et al [34] conducted tensile test of specimens with one and three rows of pins and compared the results to those of the according drop by drop pins. Their results are briefly presented in this section and are eventually compared to the findings of the classic CMT pins.

The stress strain diagram of the specimens with three rows of pins (Figure 3.23b) shows a decrease of the drop by drop pins' ultimate strain whereas the according curve of the single row samples (Figure 3.23a) are at the same level as the untreated base material. Since with the EBW treated samples the breaking happens within the pin region mainly due to the reduced cross section there the thermal influences on the material are negligible as far as tensile strength is concerned. When looking at Table 3.12 on a first glance one can see that there is beside the drop in fracture elongation a loss of ultimate tensile strength in case of three rows of EBW pins. In this context one has to keep in mind that the stresses were calculated using the original cross section area which is however diminished due to the EBW modifications.

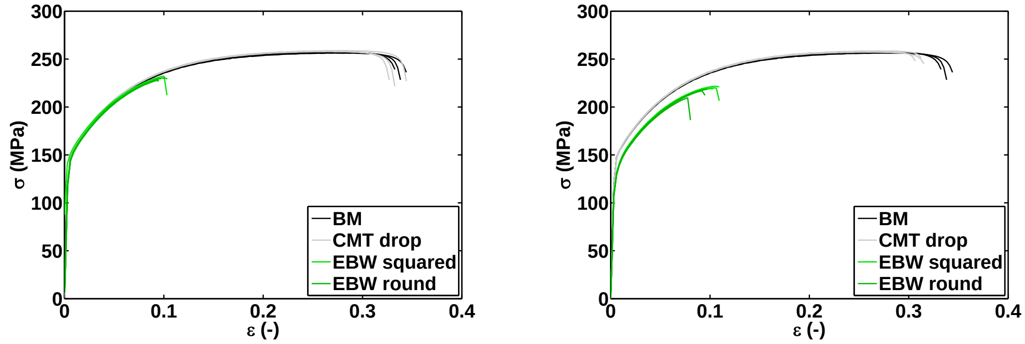

(a) Single row

(b) Three rows

Figure 3.23.: Stress strain curves of pinned samples (EBW and drop by drop) of AA6xxx alloy.

There is a principal difference of the fracture behavior between the EBW and the drop by drop pins. As shown in Figure 3.24 the EBW specimens' fracture always took place within the zone of surface modification because of the reduced cross section there. Eventually, Table 3.13 gives a comparison of CMT, drop by drop and EBW pins regarding their base material's mechanical behavior under the influence of pins. The CMT welding process, in the form of classic and drop by drop pins, hardly influences the base

Table 3.12.: Averaged fracture elongation (ϵ) and ultimate tensile strength (σ) of the AA6xxx samples, from [34].

	$\boldsymbol{\epsilon}(-)$	$\boldsymbol{\Delta\epsilon}(-)$	$\boldsymbol{\Delta\epsilon}_{\mathrm{rel}}(\%)$	$\mathbf{R_m}$**(MPa)**	$\mathbf{\Delta\ R_m}$**(MPa)**	$\mathbf{\Delta\ R_{m,rel}}(\%)$	**n**
BM	0.340	0.004	1.18	257.1	0.5	0.2	3
1 R drop	0.335	0.007	2.1	258.6	0.5	0.2	3
1 R EBW	0.098	0.006	6.1	228.0	1.0	0.4	3
3 R drop	0.313	0.004	1.3	258.3	0.5	0.2	3
3 R EBW	0.092	0.008	8.7	215.0	4.0	1.9	3

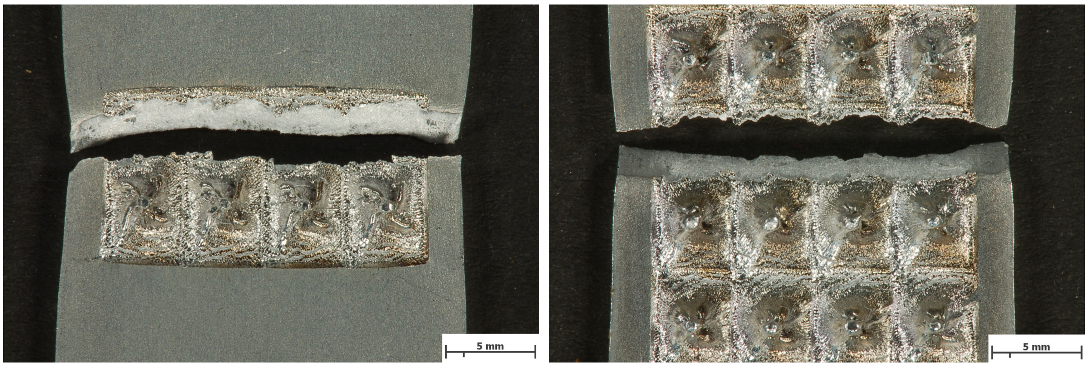

(a) (b)

Figure 3.24.: Fracture images of AA6xxx specimens with a single (a) and three (b) rows of EBW pins

Table 3.13.: Comparison of ultimate strength and fracture elongation of CMT, drop by drop and EBW samples in reference to the base material without pin. The data of the drop by drop and EBW samples were taken from the work of Tändl [34]

	CMT		**drop**		**EBW**	
	ϵ[%]	**R_m(%)**	**ϵ(%)**	**R_m(%)**	**ϵ(%)**	**R_m(%)**
1 R	71	100	99	101	29	89
2 R	68	98	-	-	-	-
3 R	71	98	92	101	27	84

material's mechanical performance as far as ultimate strength is concerned. Structuring the surface by means of EBW diminishes the ultimate strength by 11 to 16%. In terms of fracture elongation the sample with classic CMT pins show significant drop of roughly 30%. This drop is independent of the number of pins. The fracture elongation of the specimens with drop by drop pins does not change. However the EBW structured samples exhibit a reduced ultimate strain of one third of the untreated samples. This severe drop in fracture elongation originates from the reduced cross section of these samples due to the EBW process as shown in [16].

Figure 3.25 shows the tensile strength versus the ultimate strain of the samples with classic CMT pins. The ferrous alloys did not show any particular impact by the welding process, only the partially big deviations of the ultimate strain in the case of stainless steel (Figure 3.25a) are noticeable.
The aluminum plates with classic CMT pins exhibited a significant drop in ultimate strain compared to the untreated base material. However, the according samples with drop by drop pins only showed a diminished ultimate strain in the case of three pin rows. One explanation for this might be that the drop by drop process itself has a lower heat input than the conventional CMT technique.
The EBW samples' fracture elongation decreased independently of the number of pins and the alloy. The main mechanism of weakening here is the reduced cross section resulting from the EBW process.

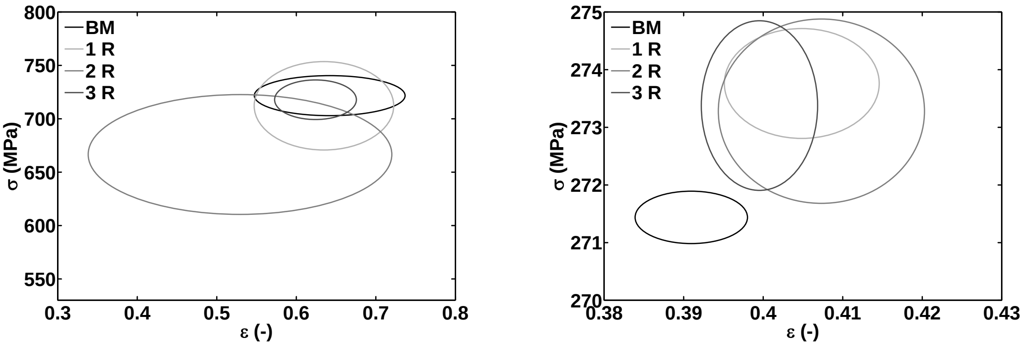

(a) Stainless steel

(b) DX 54

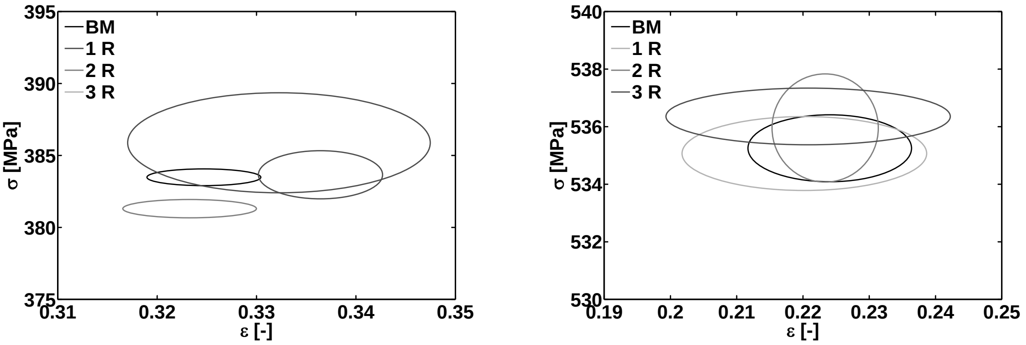

(c) HC260LA

(d) HC420LA

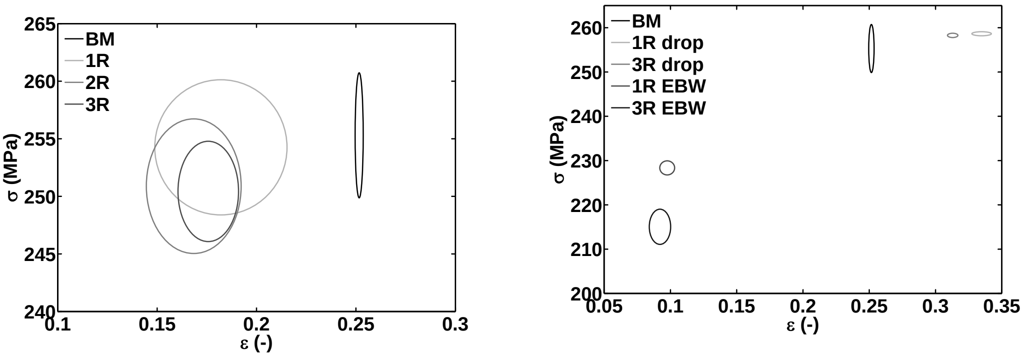

(e) Aluminum 6xxx series

(f) Comparison of EBW and drop by drop pins.

Figure 3.25.: Summary of the tensile test.

3.3. Tensile tests of pin reinforced joints

The chapters so far have only dealt with the pin welding process and its interaction with the base material. However, in terms of actual applications of pins as a reinforcement of dissimilar joint we wanted to find out how pin influence the behavior of an actual joint. In doing so we performed single lap tensile tests of stainless steel plates attached to carbon fiber reinforced plastics (CFRP). On the overlap area we placed an array of 4x4 of ball headed and cylindrical pins, respectively. Such a specimen is depicted schematically in Figure 3.26. The tests without pins were conducted at the TU Wien. The laminate thickness as well as the plate thickness was 2 mm for all specimens.

In Figure 3.27 the results of single lap tensile tests without pins is shown. The force maximum is at some 3516 ± 741 N and the fracture elongation is at 0.286 ± 0.082 mm. The curves in Figure 3.27 indicate a brittle fracture behavior.

In contrast the curves in Figure 3.28 exhibit a rather different shape than those in Figure 3.27. After reaching a first force maximum one can observe a drop after which a second maximum is reached prior to the eventual failure. The averaged values of these curves are listed in Table 3.14.

At the distinct first maximum the adhesive bonding between steel and CFRP fails. The second force peak results then from the mechanical resistance of the pins. In the case of ball headed pins this second maximum in force is significantly higher than the first one. This is due to the geometry of this kind of pins where the ball's additional undercut aggravates the pulling out of pins from the CFRP laminate. The fracture images in Figure 3.29 also suggest the aforementioned pullout and failure mechanisms. The cylindric pins are slightly bent and pulled out of the laminate without damage (Figure 3.29a).

The ball pins on the other hand were partly broken. Furthermore, the pullout of the pins was not as 'clean' as the cylindric pins, i.e. the laminate was damaged (see Figure 3.29b).

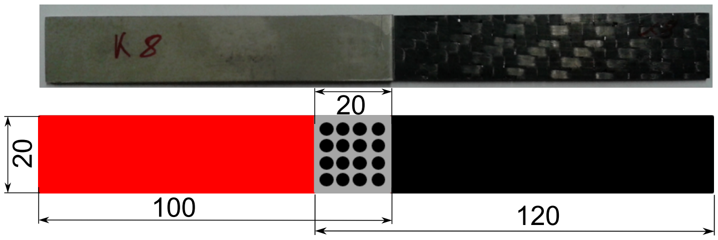

Figure 3.26.: Geometry of the specimens used for single lap shear tests, all values in mm.

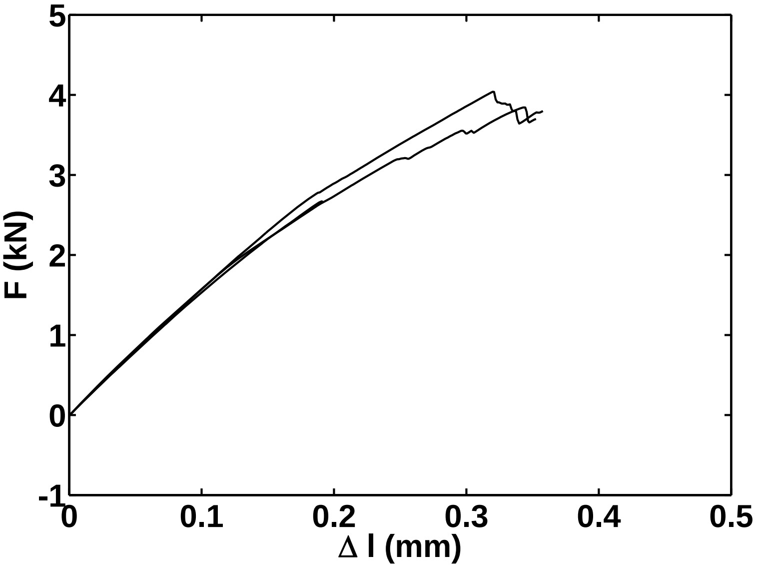

Figure 3.27.: Force displacement curves of single lap tensile tests conducted at the TU Wien.

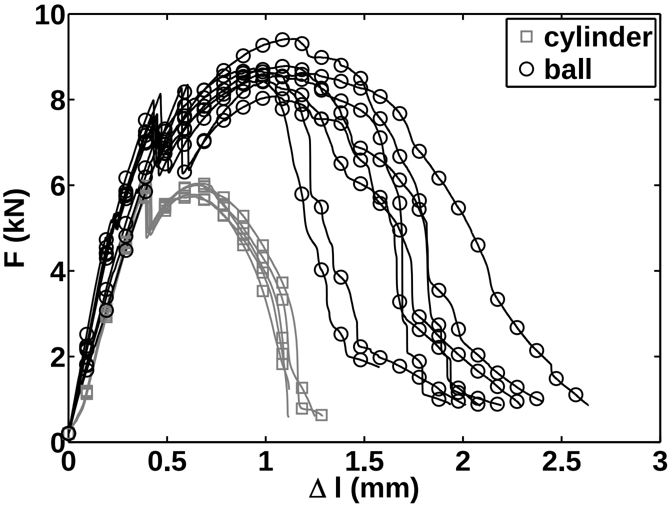

Figure 3.28.: Force displacement curves of pin reinforced stainless steel - CFRP joints.

Table 3.14.: Averaged force maxima and minima of the curves in Figure 3.28. The samples without pins had an average force maximum of 3516±741 N and a fracture elongation of 0.286±0.082 mm.

	$\mathbf{F_{maxI}}$ (N)	$\mathbf{l_{maxI}}$ (mm)	$\mathbf{F_{min}}$ (N)	$\mathbf{l_{min}}$ (mm)	$\mathbf{F_{maxII}}$ (N)	$\mathbf{l_{maxII}}$ (mm)
cylinder	5933 ± 132	0.402 ± 0.012	4888 ± 84	0.409 ± 0.012	5911 ± 142	0.645 ± 0.008
ball	7936 ± 330	0.485 ± 0.073	6499 ± 262	0.494 ± 0.071	8690 ± 337	0.991 ± 0.192

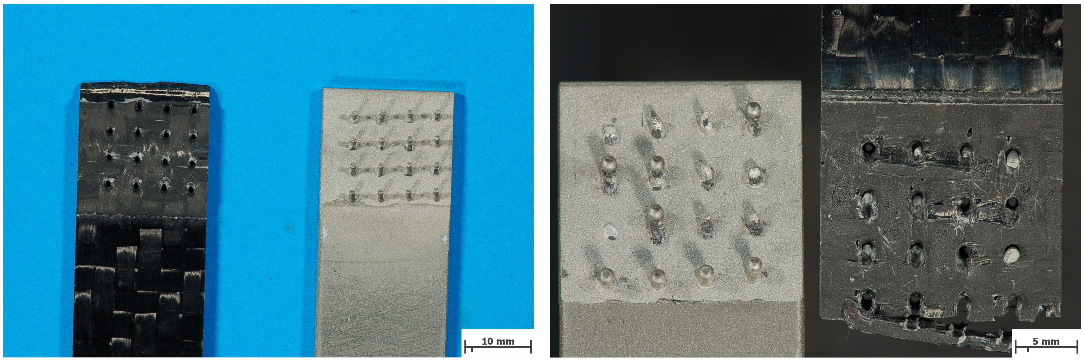

(a) cylindric pins (b) ball pins

Figure 3.29.: Images of the broken dissimilar joint reinforces with cylinder and ball pins.

3.4. Summary

Investigations of single pins lead to the conclusion that the quality of the pins depends, amongst others on the used material. In the case of austenitic stainless steel pins the connection between base material and pin is very good. Aluminum pins on the contrary show significant flaws as far as the pin plate interface is concerned.

In terms of pin geometry we could observe that in the case of stainless steel pins the overall height is pretty well adjustable (compare Table 3.2). In the case of aluminum pins on the other hand the minimum height is limited by the material. Thus we could not achieve pin heights below 2mm using the classic CMT process[2]. In order to produce shorter pins the concept of CMT drop by drop pins was introduced. However, the shape of such pins turned out to be inappropriate for joints with CFK laminates. In general, the quality of aluminum pins as far as the porosity of the pin - substrate interface is concerned crucially depends on the substrate's surface pretreatment. Even cleaning the surface with a commercial cleaning agent distinctly reduces porosity.

Finally we investigated surface modifications using electron beam welding. Here pin like structures of under 2mm height can be achieved within very close scatter (see Figure 3.30).

Investigations on the mechanical performance of the base material after pin welding revealed that in the case of classic CMT pins only aluminum showed a significant change in fracture elongation (see Figure 3.25). The other materials (especially the steel samples HC260, HC420 and DX54) exhibited hardly any affection due to the pin welding process.

Single lap tensile tests of dissimilar joints of stainless steel and CFRP reinforced with pins revealed that pins enhance the mechanical performance of such joints significantly. The force displacement curves show a very distinct shape (Figure 3.28). Even the first force maximum is higher than in the case of specimen without pins. After a drop the force increases again until the ultimate failure. However, this second increase of force is not really an increase of fracture toughness because failure sets in after the first force maximum, but it can serve as a safety margin for technical applications.

---

[2] Too high pins can not be used for attaching CFK laminates because they deform during the imprint process. Therefore we agreed on a maximum height of 2mm within the project group

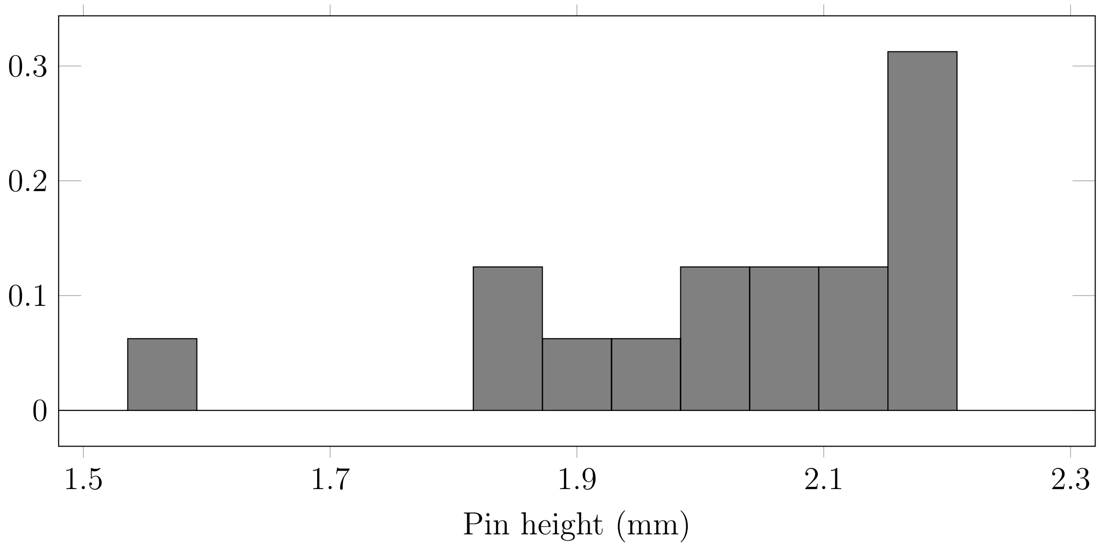

(a) CMT pins

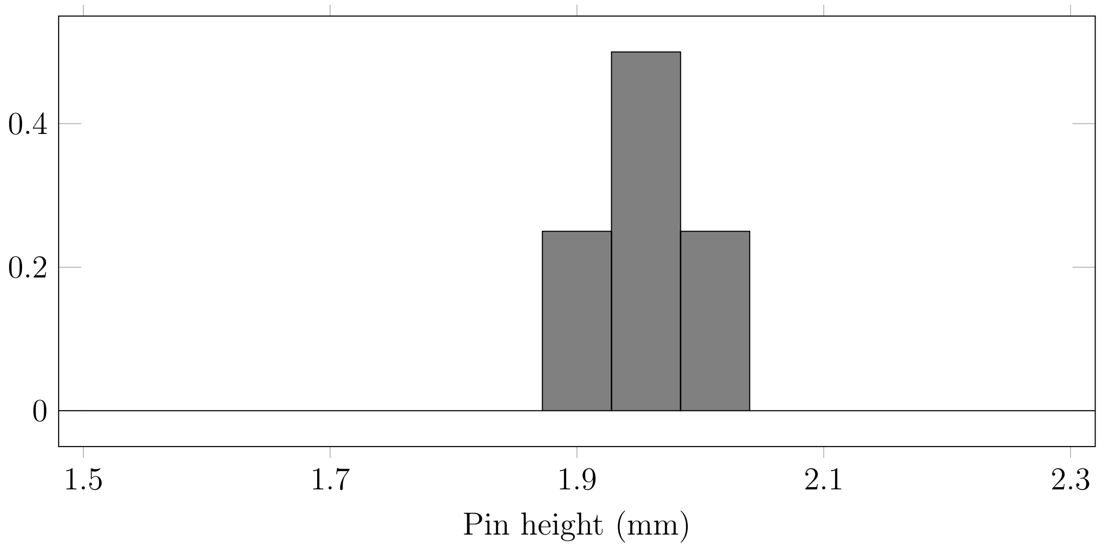

(b) EBW pins

Figure 3.30.: Pin height distribution CMT and EBW pins on aluminum of the 6xxx series, n=16

4. Simulations

In order to obtain insights to the welding process of a single pin we conducted finite element simulations. Since the geometry of such a pin is quite small and the process quite quick such simulations are an appropriate tool for our needs.
Furthermore, we performed FE simulations in order to determine the different heat input in the context of laser pretreatment with aluminum pins.
The mechanical calculations of a single pin under shear loads and the simulation of an actual pin reinforced joint are the topics of the last part of this chapter. In doing so we applied the cohesive zone model for modeling the contact behavior between the two components.

4.1. Simulating the welding process of a single pin

Simulating the welding process of a single pin was presented at the *Sysweld users forum* in Weimar [35] by the author. Since experimental investigations revealed that stainless steel pins are best reproducible we decided use this setup for numerical investigations. The material properties of the base (AISI 304) and the filler material (AISI 308) are given in Appendix A.

4.1.1. The model

Heat input

In order to mimic the heat input during the welding process of a pin, we used Goldak's double ellipsoidal heat source [6]. The mathematical implementation is given in equation 2.12 on page 11.
Originally this heat source was conceived for modeling a moving heat source. The term q_0 (Equation 2.12b) describes the amount of power deposited at the center of the source, whereas the exponential part in Equation 2.12a describes the spatial power distribution. Since the Goldak heat source was originally designed to mimic the heat input of seam

Figure 4.1.: Axissymmetric FE model of a single pin. The rotational axis is represented by the dashed line.

welding it is split in two parts, one in front of the heat source (in welding direction) and the second one being behind. The parameter f then describes the power distribution among the front and the rear part of the heat source. The shape of the ellipsoid is determined by the entities a, b and c in Equation 2.12.

In order to simulate the pin welding process it became necessary to modify the original Goldak source. First of all we made use of the symmetry of the problem, i.e. we used an axial symmetric model with the y-axis being the rotational axis as depicted in Figure 4.1. The dimension of the model, such as the pin foot's height and width were taken from micrographs of cross-sections like those in Figure 3.1 on page 28. According to the assumptions described above (axial symmetry)we modified the original Goldak heat source accordingly. These modification were done in the same manner as in Goldak's original work [6]. Due to the rotational symmetry it is more practicable to use cylindric coordinates. In order to be consistent with mesh's orientation we denote the y-axis as rotational axis and x is the radial direction ($x \widehat{=} r$). Thus an immobile Gaussian like power density reads as follows

$$q = q_0 e^{-Ax^2} e^{-By^2}. \tag{4.1}$$

with q_0 being the power density at the center of the ellipsoid. The overall power input is then

$$\tilde{Q} = q_0 \int_0^{2\pi} d\varphi \int_0^{\infty} x e^{-Ax^2}\, dx \int_{-\infty}^{\infty} e^{-By^2} dy. \tag{4.2}$$

Computing the Gaussian integrals in Equation 4.2 yields the following term

$$\tilde{Q} = q_0 \frac{\pi\sqrt{\pi}}{A\sqrt{B}}. \tag{4.3}$$

This expression has to equal the twice the total heat input Q[1]

$$q_0 \frac{\pi\sqrt{\pi}}{A\sqrt{B}} \overset{!}{=} 2Q \tag{4.4}$$

leading to the following relation

$$q_0 = \frac{2QA\sqrt{B}}{\pi\sqrt{\pi}} \tag{4.5}$$

In order to determine the parameters A and B we demanded, that at the ellipsiod's surface the power density must drop to 5% of its central value as in the work of Goldak [6].

$$q(x_0, 0) = q_0 e^{-Ax_0^2} = 0.05 q_0.$$

thus

$$A = \frac{\ln 20}{x_0^2} \simeq \frac{3}{x_0^2} \tag{4.6}$$

In a similar way we obtained

$$B = \frac{3}{y_0^2}. \tag{4.7}$$

---

[1] The factor 2 is due to the fact that only the half ellipsoid in the -y region is used for describing the heat input. The integration limits in equation 4.2 on the other hand are $]-\infty, \infty[$.

Combining Equations 4.1, 4.5, 4.6 and 4.7 yields for the power input

$$q = \frac{6\sqrt{3}Q}{x_0^2 y_0 \pi \sqrt{\pi}} e^{-3\frac{x^2}{x_0^2}} e^{-3\frac{y^2}{y_0^2}}. \tag{4.8}$$

In the case of pin welding, the power input Q is given by

$$Q = \eta U I f \tag{4.9}$$

with U and I being the arc voltage and arc current, respectively. The term η denotes the arc efficiency taking into account the energy losses of the welding arc. The mostly complex processes going on inside the weld pool are mapped onto the ellipsoid described by the auxiliary parameters x_0 and y_0 (compare Equation 4.8). The auxiliary parameters x_0 and y_0 describe the spatial expansion of the ellipsoid. In the real pin welding process, wire and plate are not in contact while the arc is active. In order to model this we introduced an interface layer between wire and plate which acted as an thermal insulator. Furthermore, we split the heat source in two part, one acting on the plate and the second one on the pin. Therefore the parameter f in Equation 4.8 was introduced, which ranges from 0 to 1 depending on how much energy is deposited on the plate or the pin, respectively. For the sake of energy conservation f_{total} must satisfy

$$f_{\text{total}} = f_{\text{plate}} + f_{\text{pin}} \overset{!}{=} 1 \tag{4.10}$$

The schematic energy distribution in radial direction is given in Figure 4.2. Figure 4.3 illustrates the region where the heat source was applied. After the heating stage was finished material's parameters of the elements in the interface region were reset to those of the pin elements.

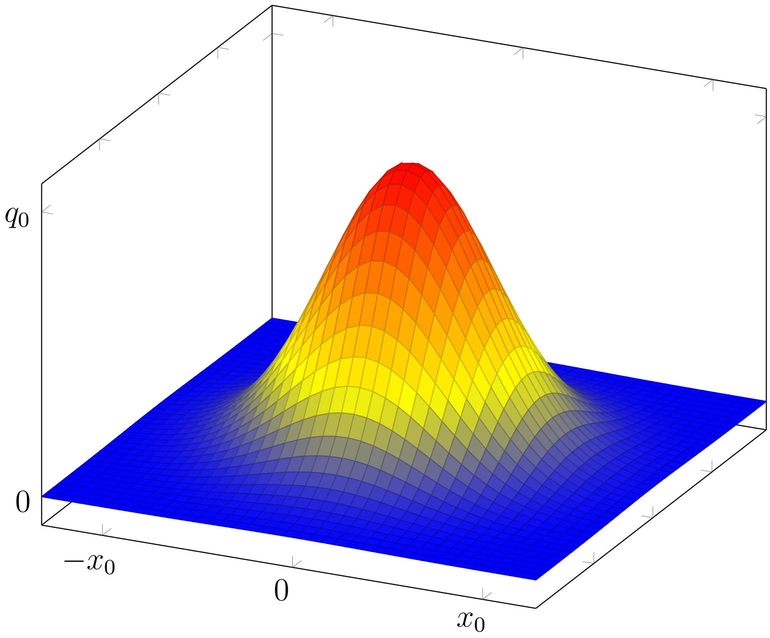

Figure 4.2.: Power distribution in radial direction of the modified Goldak heat source.

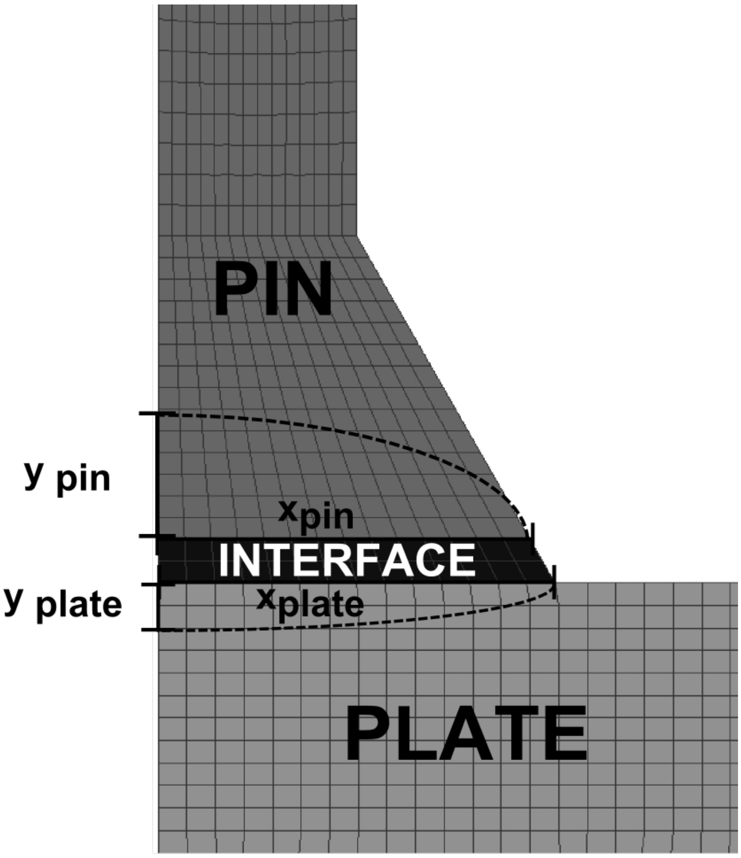

Figure 4.3.: Illustration of the modified Goldak heat source at the interface region of the pin and the plate.

Mechanics

For the mechanical analysis we assumed plasticity with isotropic strain hardening. The respective temperature dependent material parameters were taken from the SYSWELD material database. In detail, the material law looks as follows:

- The material is assumed to be elastic having a certain Young's modulus until the stress exceeds its yield stress. In our case we used the von Mises equivalent stress as yield criterion.
- Beyond yield stress the stress-strain law is given piece wise linearly (see Figure 4.4)

Boundary conditions

In order to describe the heat exchange of the workpiece with its environment we considered the following mechanisms:

- radiation
- convection and
- thermal conduction.

In terms of finite element analysis they must be taken into account by appropriate boundary conditions. In doing so we made use of the *lumped capacitance* approach [36]. In this model the heat transfer coefficient describing losses due to radiation reads as follows

$$h_{\mathrm{rad}} = \sigma\epsilon\left(T + T_0\right)\left(T^2 + T_0^2\right) \tag{4.11}$$

where T_0 is the temperature of the surrounding medium. The quantity σ denotes the Boltzmann's constant and ϵ the emissivity.

Heat losses caused by convection were taken into account by an additional parameter h_{c} being the convective heat transfer coefficient. In contrast to radiation h_{c} was assumed to be temperature independent. Furthermore we divided the boundary of the system in two sections of different convective heat transfer coefficients. In the region of the interface of pin and plate the convective heat transfer coefficient was assumed to be higher than at the rest of the surface. This assumption appears to be reasonable since the loss of energy in this region is enhanced due to vortices of the shielding gas in this area.

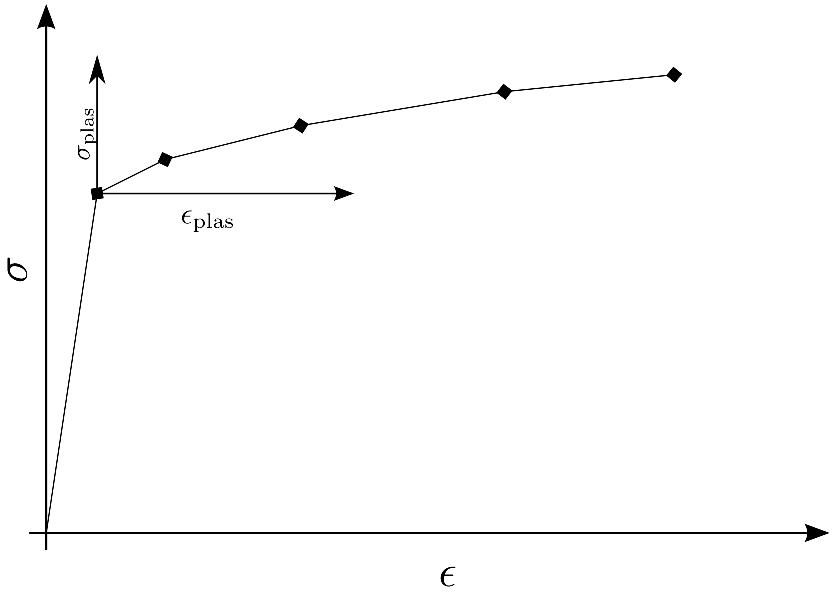

Figure 4.4.: Illustration of the stress-strain law implementation in the SYSWELD software package

Thus, the overall heat exchange coefficient addressing energy interactions with the surrounding medium is then given by

$$h = h_{\text{rad}} + h_{\text{c}}. \tag{4.12}$$

The temperature at the nodes located on the lower side of the plate as well as those at the very top edge of the wire was constrained. These rigid boundary conditions take into account that those are not real surfaces exposed to the surrounding air. In the case of the top nodes , there is continuing wire and at the bottom the plate is in direct contact to the work bench.

The mechanical boundary conditions for this calculations were as follows:

- During the pullback phase the velocity in y direction of the wire's top node was 5 mms^{-1}. Nodes at the plate's surface were restricted from moving, i.e. the velocity was set to be zero.

- In the shaping stage the clamped nodes at the surface were fixed and the velocity of the top nodes was 33 mms^{-1}.

The velocities above were predefined by the actual parameters of the welding program.

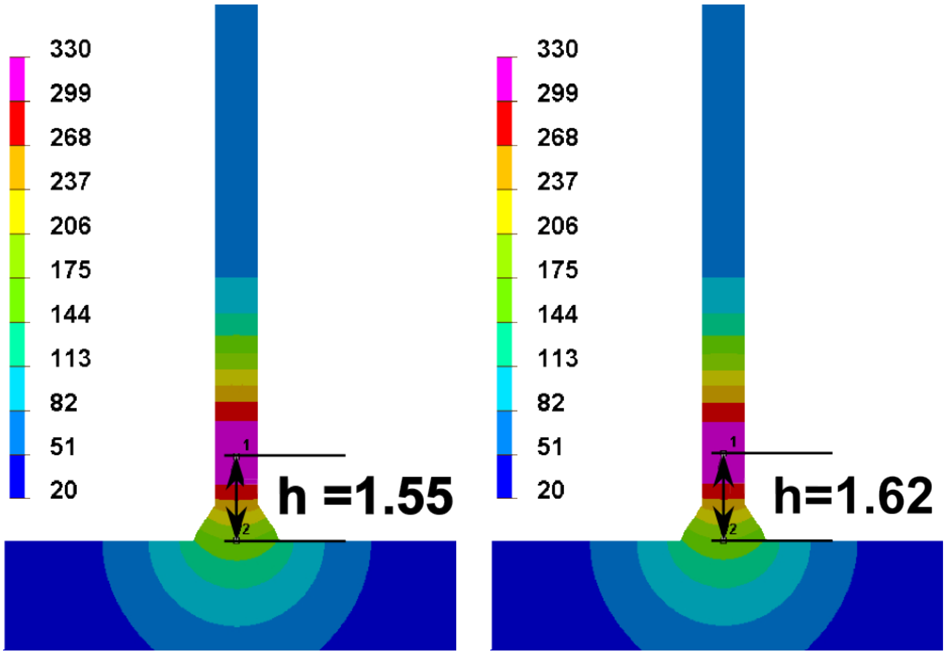

(a) (b)

Figure 4.5.: Temperature fields for different values of h_c. The plotted distance markers indicate the distance of the zone with maximum temperature to surface of the base material.(a) $h_c = 80\ \mathrm{Wm^{-2}K^{-1}}$ (b) $h_c = 200\ \mathrm{Wm^{-2}K^{-1}}$

Parameter study of h_c As mentioned above, the convective heat transfer coefficient can be assumed to be different in the region of the pin socket than in other areas of the system. In order to investigate the influence of different values for h_c within the interface area we conducted several calculations using values for h_c ranging from 80 to 200 $\mathrm{Wm^{-2}K^{-1}}$, all other parameters were kept constant. In Figure 4.5 the temperature distribution after the cooling phase is depicted for different h_c values. Higher values of h_c in the region of the pin socket enhances the heat flow out of the wire and thus causes the zone of maximum temperature to migrate higher upwards the wire. The absolute value of the maximum temperature gets lower with rising h_c. This vertical position of the hottest zone eventually defines the pin's hight for the electrical resistance being largest there.

However, the overall effect of varying h_c is very small (h=1.55 mm at $h_c = 80\ \mathrm{Wm^{-2}K^{-1}}$ and h=1.62 mm at $h_c = 200\ \mathrm{Wm^{-2}K^{-1}}$) and so we did not continue on investigating this issue. For all further calculation we used $h_c = 200\ \mathrm{Wm^{-2}K^{-1}}$.

4.1.2. The process

The numerical implementation of the pin welding process is schematically illustrated in Figure 4.6.

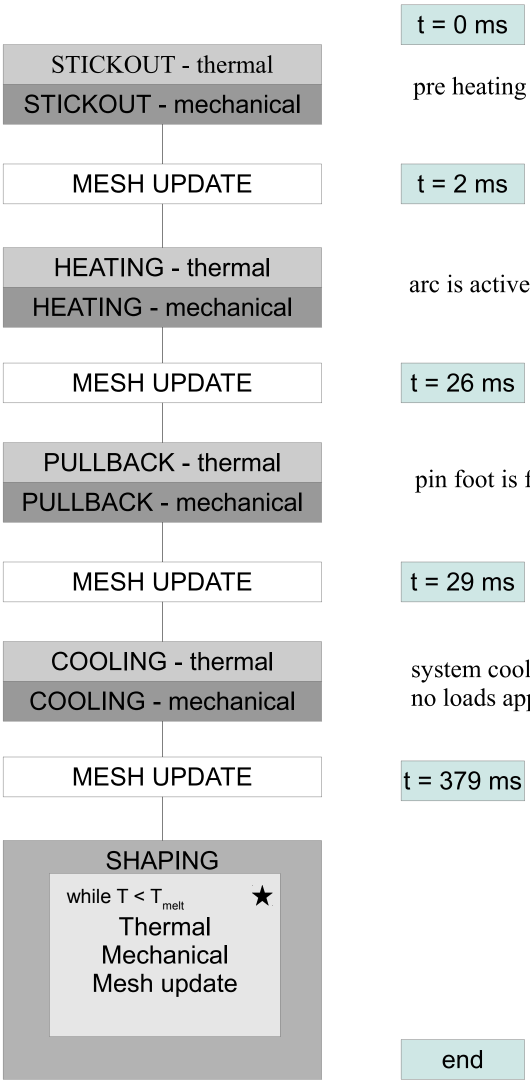

Figure 4.6.: Flow chart of the welding process of a single pin. The light gray boxes represent electro-thermal calculations and the dark gray ones mechanical computations. The star in the shaping box indicates that these processes were repeated. The time is given in absolute values.

Stickout

Prior to the actual heat input due to the arc the wire gets preheated for 2 ms by ohmic heating by applying current of 30 A - the so called *stickout phase.*

Heating

The actual heat input due to the arc was simulated using the aforementioned Goldak heat source. Since in the real welding process wire and base material are not in contact during the arc stage the thermal conductivity and the heat capacity of the interface elements (compare Figure 4.3) was set to 10^{-6} $\mathrm{Wm^{-1}K^{-1}}$, i.e. wire and plate elements were thermally insulated from each other. After 24 ms the arc is turned of and the wire and plate are in contact. In terms of modeling this means that the Goldak heat source is no longer active and that the interface elements are assigned the same thermal material properties as the wire elements.

Pullback

After the heating stage the system is exposed to external mechanical deformations. Due to a short pullback of the wire the conical pin foot is formed. In this stage of the process the system is not exposed to any thermal nor electric loads.

Cooling

With the arc turned off no more thermal loads are applied for 350 ms. During this time the system cools down and the zone of maximum temperature migrates from the fusion zone into the wire. This migration is illustrated in Figure 4.7 where the temperature distribution during the colling stage is depicted. It can be observed that with advancing time the peaks' positions shift to the right, i.e. to positions farther away from the plate.

Shaping

Applying a current after the cooling time of 350 ms increases the wire's temperature at its hottest zone resulting in reduced yield strength in this area. When applying a tensile load on this configuration, the wire would crack preferably in this particular zone. At this point it becomes evident that changes in the geometry due to the pullback directly influence the wire's physical behavior (increased electric resistance due to reduced cross

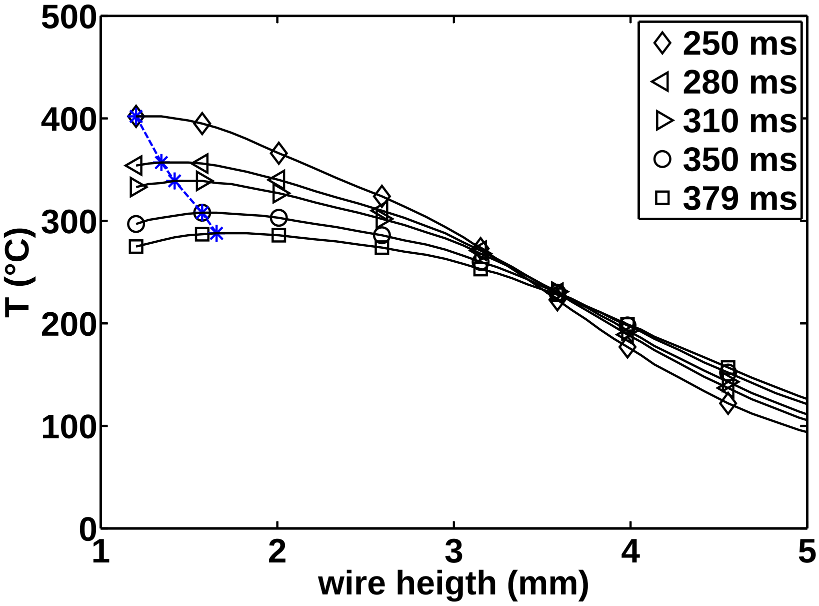

Figure 4.7.: Temperature distribution during the cooling stage at different time steps. The stars mark the maximum temperature.

section). Therefore it is necessary to couple thermo-electrical and mechanical computations as depicted in Figure 4.6. The above coupling was done using SIL (Sysweld interface language) [37] a script language that comes with Sysweld. The used routine may be found in Appendix C.1. This coupling was repeated as long as the maximum temperature did not exceed the wire's melting temperature. This assumption seems plausible since electron microscope investigations suggest that for all pin shapes at least the very top of the fracture surface was molten during shaping (compare Section 3.1.1 on page 27).

Figure 4.8 shows the temperature distribution during the shaping stage at several time steps prior to the wire's breaking. One can see that the temperature reaches its maximum right in the necking zone and thus causes the wire to rip at this very defined hight. Another interesting point in Figure 4.8 is, that when approaching the breaking point the zone of maximum temperature gets more localized, i.e. the vertical expansion of the area of maximum temperature decreases. In Figure 4.9 this development described above is clearly visible as the peak at maximum temperature becomes more distinct with advancing time. Furthermore the region of the highest temperature is shifted slightly upwards into the wire.

During the shaping process interactions between mechanics and thermo-electric effects

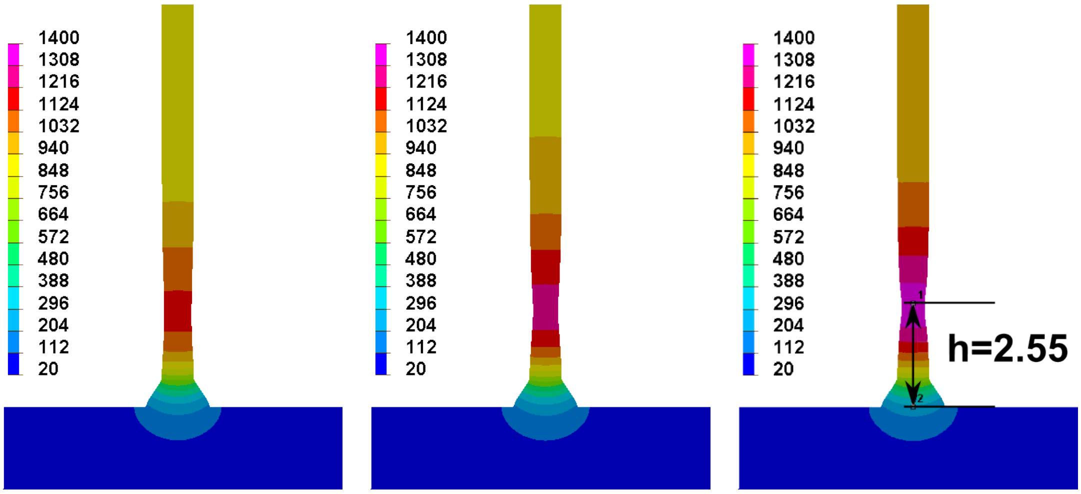

(a) (b) (c)

Figure 4.8.: Temperature distribution during the shaping phase of an electro-thermal mechanical coupled simulation. Picture (a) at 450 ms, (b) at 455 ms and (c) at 459 ms when the wire breaks

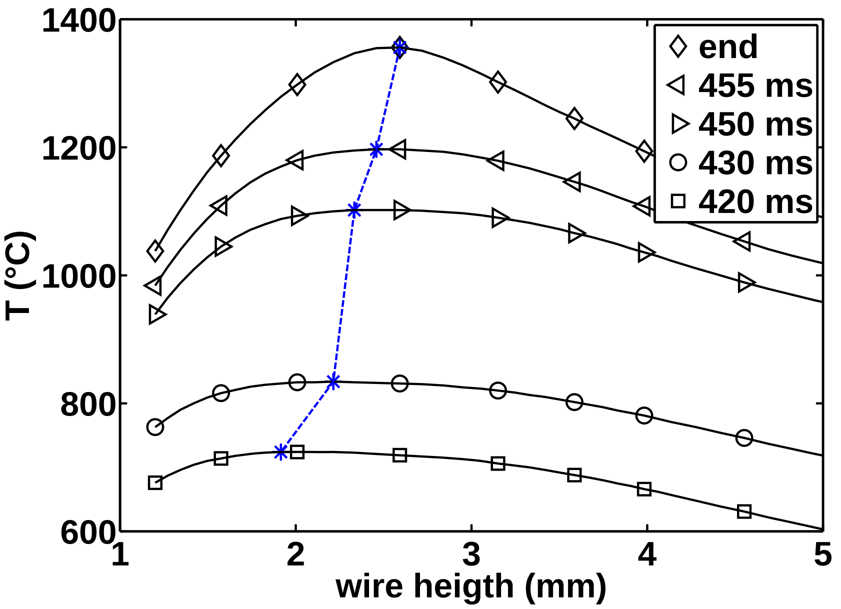

Figure 4.9.: Temperature distribution during the shaping stage at different time steps. The stars mark the maximum temperature.

must be considered. On the one hand the electrical resistance increases at the point of maximum temperature causing the wire to heat up further. The contractions in the zone of elevated temperature lead then to a reduced cross section and therefor to a rising electrical resistance. In order to mimic the shaping process described above, the shaping phase was subdivided in several electro-thermal and mechanical calculation steps. After each mechanical analysis the mesh was updated for the following thermal calculation. The process ended if the temperature within the necking zone exceeded the melting temperature of the wire material. The material parameters used in this study are illustrated in Appendix A.

4.1.3. Optimizing the Goldak heat source

As mentioned above, the Goldak heat source is not a strict physical model for the heat input due to welding. The parameters x_0, y_0 and η are auxiliary quantities, simplifying much more complex processes within the weld pool. As a consequence, these values must be adopted for every specific case in order to describe the correct heat input distribution. A common way to do this is to adjust these parameters manually until the simulated results (size of molten or heat affected zone) meet the experimental data, e.g. temperature measurements or microscopic cross sections. In our case, we did the comparison with experiments by comparing the molten zone from micrographs and FE calculations. The following study was published in *Mathematical modelling of weld phenomena 10* [38] by the author of this thesis.

In order to conduct the adjustment of the Goldak heat source more systematically we applied the *artificial bee colony* algorithm for optimization as described in Section 2.5. In the case of the pin welding process we conducted the optimization with respect to the following six ($D = 6$) parameters: $x_1 \overset{\wedge}{=} x_{0,\mathrm{pin}}$, $x_2 \overset{\wedge}{=} y_{0,\mathrm{pin}}$, $x_3 \overset{\wedge}{=} f_{\mathrm{pin}}$, $x_4 \overset{\wedge}{=} x_{0,\mathrm{plate}}$, $x_5 \overset{\wedge}{=} y_{0,\mathrm{plate}}$ and $x_6 \overset{\wedge}{=} \eta$ (compare Equation 4.8 and 4.9 in Section 2.3.1).

The first step is to create a pool of SN parameter sets, hence one deals with SN vectors $[\mathbf{x}_1, \mathbf{x}_1, ..., \mathbf{x}_{SN}]$ with six entries $(x_1, x_2, ..., x_6)$ each. The number of trial parameter sets SN does not change during the optimization. Initially, the values for the parameters x_1 to x_6 are chosen randomly within certain boundaries which are summarized in Table 4.1.

Table 4.1.: Set of parameters to be optimized using the ABC algorithm and their upper and lower boundaries

	$\mathbf{x_1}(\mathbf{x_0}_{,\mathrm{pin}})$	$\mathbf{x_2}(\mathbf{y_0}_{,\mathrm{pin}})$	$\mathbf{x_3}(\mathbf{f}_{\mathrm{pin}})$	$\mathbf{x_4}(\mathbf{x_0}_{,\mathrm{plate}})$	$\mathbf{x_5}(\mathbf{x_0}_{,\mathrm{plate}})$	$\mathbf{x_6}(\eta)$
lower boundary	0.3	0.4	0.5	0.6	0.001	0.7
upper boundary	1.5	1.0	1.0	1.5	0.05	0.9

The comparative parameters we used were the penetration depth of the molten zone into the plate d_{plate} and into the wire h_{pin} and h_{pinout} as well as the horizontal expansion within the base material r_{plate}. The comparative parameters described above are illustrated in Figure 4.10.

In addition to those geometric parameters the maximum temperature within the welding zone was used as another comparative parameter. In the case of the maximum temperature the target value v was set to 2000°C. However, the target value for the temperature is only estimated since accurate temperature measurements are extremely tedious due

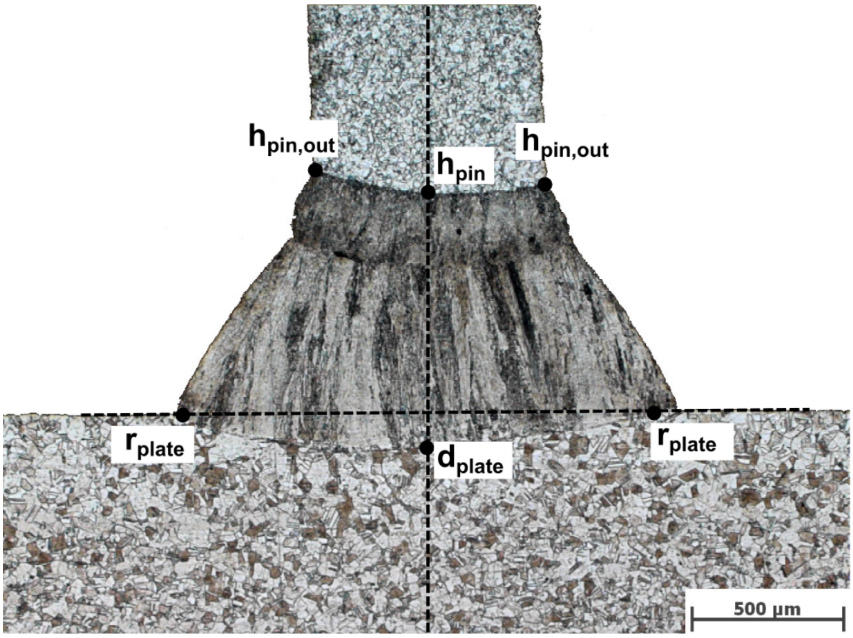

Figure 4.10.: Micrograph of the pin plate interface. The black dots mark the points used to describe the spatial expansion of the molten zone. For the values r_{plate} and h_{pinout} the average of left and right hand side entities were used.

to the small sample geometry and the short welding times. Table 4.2 gives an overview over the experimentally evaluated target parameters and the target temperature.

Table 4.2.: Target parameters and their values used for the optimization evaluated from Figure 4.10.

$\mathbf{h}_{\text{pin}}$**(mm)**	$\mathbf{h}_{\text{pinout}}$**(mm)**	$\mathbf{d}_{\text{plate}}$**(mm)**	$\mathbf{r}_{\text{plate}}$**(mm)**	$\mathbf{T}_{\text{max}}$**(°C)**
0.74	0.79	0.12	0.79	2000

After all, the temperature was introduced as an optimization criterion in order to avoid the computed temperatures to become unrealistically high. Since the values of the temperatures are several orders of magnitude higher than the geometry parameters the difference in temperature in Equation 2.39 was calculated according to the following formula:

$$v_l - w_l = \frac{T_{\text{target}} - T}{T_{\text{target}}} \tag{4.13}$$

In this work we determined the fitness function according to the steps below:

- The welding process was simulated by means of finite elements method with $(x_1, x_2, \ldots, x_D)$ as input parameters of the Goldak heat source.

- The comparative entities ($\mathrm{h_{pin}}$, $\mathrm{h_{pinout}}$ etc.) $w_1, \ldots w_m$ were extracted from the FE simulation.

- The fitness function fit_i (equation 2.41) was computed.

After the initialization and evaluation of the fitness function (Equation 2.41 on page 24) for the initial parameter set, the actual optimization starts. The ABC routine was programmed in Python 2.7 [39], the FE calculations were conducted in Sysweld ®. The according scripts are provided in Appendix B.

Influences of the number of parameter sets

Table 4.3.: Numerical parameters used in the investigated optimizations.
SN ... number of trial sets
CN ... number of optimization cycles
L ... limit of rejections of a set of parameter

	SN	**CN**	**L**
run01	15	20	10
run02	30	20	10
run03	45	20	10

In a first series of calculation we investigated how the number of parameter sets SN influences the optimization. Therefore, we ran several calculations varying SN from 15 to 45 in steps of 15. The number of cycles CN was kept constant at 20 (run01 to run03 in Table 4.3). In Figure 4.11 the evolution of the smallest error ($f\left(\mathbf{x}_{\mathrm{best}}\right)$) over the cycles of optimization is depicted. An increasing number of parameter sets yields better results in terms of minimizing the total error. During the first couple of runs the behavior of $f\left(\mathbf{x}_{\mathrm{best}}\right)$ does not show significant differences with respect to the number of parameter sets SN. Starting from the sixth cycle, the error of run03 ($SN = 45$) decreases distinctly compared to the other two runs. During the last cycles the total error of run01 and run02 do not change any more, only $f\left(\mathbf{x}_{\mathrm{best}}\right)$) of run03 shows a slight decrease at the end of the optimization.

In Figure 4.12 the shape of the simulated weld zone and the real one are compared. Remarkably, even optimizations with a relatively large error show acceptable agreement with the experiments in terms of weld pool geometry. Table 4.4 gives the numerical values of the optimized heat source parameters and in Table 4.5 the results of the simulations using the parameters of run01, run02 and run03 are summarized.

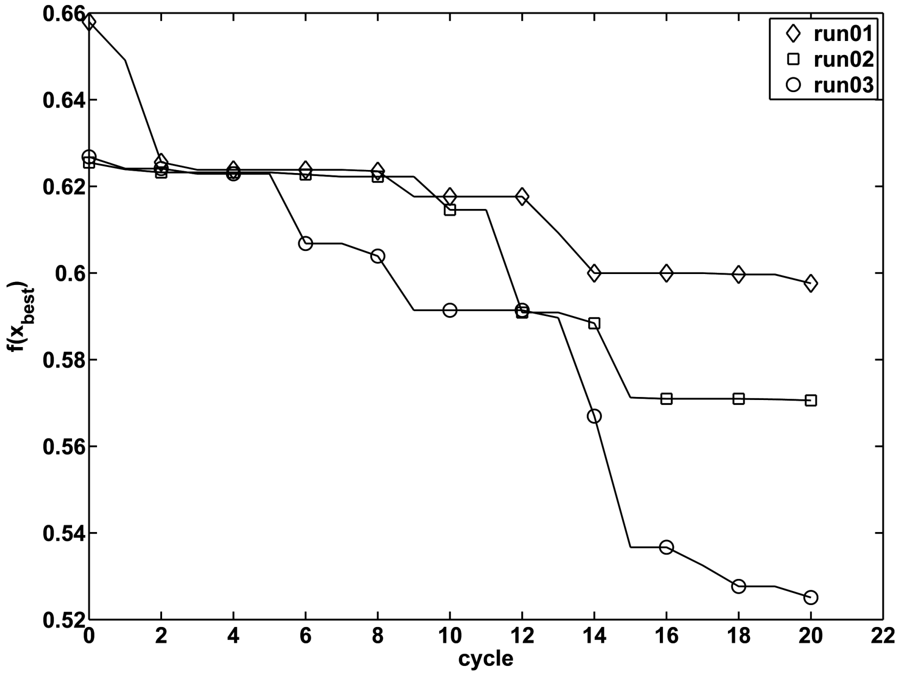

Figure 4.11.: Evolution of $f\left(\mathbf{x}_{\text{best}}\right)$ over the optimization cycles.

Table 4.4.: Optimized auxiliary parameters of Goldak's heat source (compare Figure 4.10).

	$\mathbf{x_1}(\mathbf{x_{0,\text{pin}}})$	$\mathbf{x_2}(\mathbf{y_{0,\text{pin}}})$	$\mathbf{x_3}(\mathbf{f}_{\text{pin}})$	$\mathbf{x_4}(\mathbf{x_{0,\text{plate}}})$	$\mathbf{x_5}(\mathbf{y_{0,\text{plate}}})$	$\mathbf{x_6}(\eta)$
run01	0.990	0.712	0.814	1.131	0.029	0.832
run02	1.027	0.582	0.758	1.295	0.034	0.857
run03	0.663	1.000	0.500	1.500	0.050	0.900

Table 4.5.: Results of the finite element calculations using the optimized parameters of Table 4.4

	$\mathbf{h}_{\text{pin}}$**(mm)**	$\mathbf{h}_{\text{pinout}}$**(mm)**	$\mathbf{d}_{\text{plate}}$**(mm)**	$\mathbf{r}_{\text{plate}}$**(mm)**	$\mathbf{T}_{\text{max}}(°\mathbf{C})$	$\mathbf{f}\left(\mathbf{x}_{\text{best}}\right)$
run01	0.781	0.776	0.073	0.462	2992	0.598
run02	0.718	0.713	0.072	0.520	2989	0.571
run03	0.780	0.779	0.161	0.636	2998	0.525
target	0.74	0.79	0.12	0.79	2000	

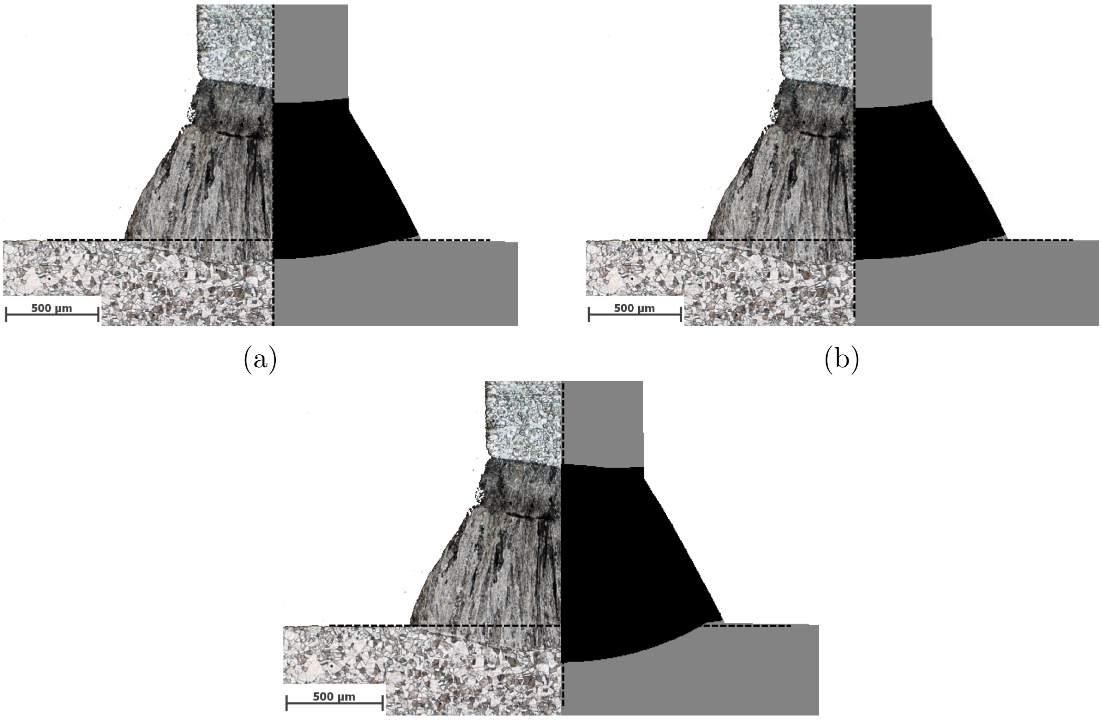

(a) (b) (c)

Figure 4.12.: Comparison of the molten zone of experiment and simulation resulting from calculation with optimized parameters of run01 (a), run02 (b) and run03 (c)

Considering the severe deviations in temperature of the calculations from the target value ($T_{\text{target}} = 2000°\text{C}$) we performed deeper investigations on how each of the comparative values contribute to the overall error. Therefore we split the overall error in a part stemming from the geometric misfits and the deviation in temperature. In doing so, we evaluated the error function (Equation 2.39) using only the parameters defining the weld pool's geometry (h_{pinout}, h_{pin}, d_{plate} and r_{plate}) and only the temperature, respectively.

Figure 4.13 shows the geometrical percentage and the contributions from the temperature to the overall error. Apparently, the ratio of the geometric error decreases during the optimization in comparison to the deviations in temperature. On the first glance this behavior seems more or less independent of the used optimization setup. However, when having a closer look on run03 one can see that temperature error is much more dominant ($\sim 90\%$) than in the other runs. Since the temperature has only been introduced as control parameter and its target value is just an educated guess due to the lack of appropriate experimental data, the domination of temperature within the total error is not tolerable.

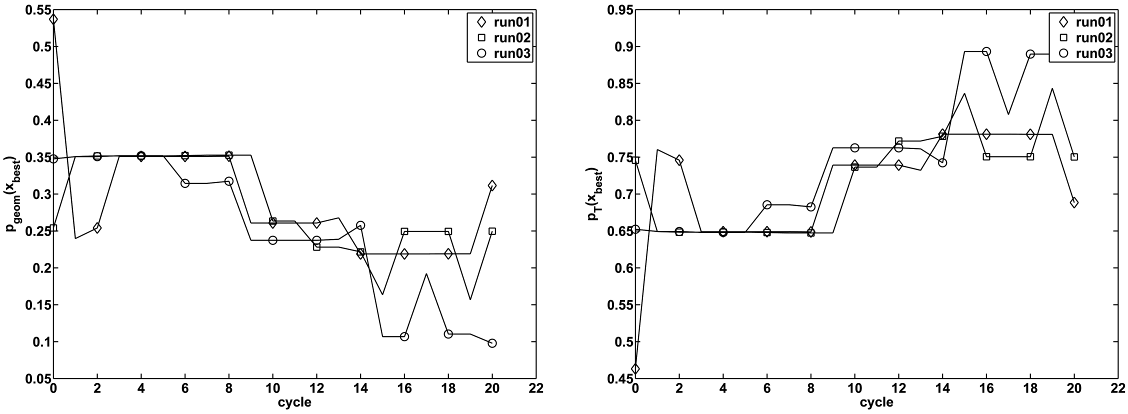

(a) (b)

Figure 4.13.: Geometric (a) and temperature (b) percentage of the overall error over optimization cycles.

Table 4.6.: Optimized parameters of Goldak's heat source of run04 to run06

	$\mathbf{x_1}(\mathbf{x_{0,\mathrm{pin}}})$	$\mathbf{x_2}(\mathbf{y_{0,\mathrm{pin}}})$	$\mathbf{x_3}(\mathbf{f}_{\mathrm{pin}})$	$\mathbf{x_4}(\mathbf{x_{0,\mathrm{plate}}})$	$\mathbf{x_5}(\mathbf{y_{0,\mathrm{plate}}})$	$\mathbf{x_6}(\eta)$
run04	0.961	0.733	0.780	1.100	0.019	0.827
run05	0.907	0.628	0.730	1.118	0.023	0.787
run06	0.901	0.717	0.760	1.133	0.018	0.770

Controlled temperature

In order to overcome the deficiencies arising with the improper choice of the temperature's target value as discussed in the previous section, we reran the optimizations above setting the target temperature to 3000°C(run04 to run06). The result of those runs ($\mathbf{f}\ (\mathbf{x}_{\mathrm{best}})$ over cycles) is shown in Figure 4.14. The overall error is significantly lower than in the previous optimizations and virtually independent of the optimization setup.

Figure 4.15 depicts the development of the geometric misfits and the error in temperature of the modified optimization setups. It clearly reveals that the overall error is mostly dominated by geometric misfits and that temperature deviations play only a minor role. The optimized heat source parameters are listed in Table 4.6 and the results of the FE analyses with those parameters are in Table 4.7.

Furthermore, we conducted another computation investigating the impact of the maximum temperature as an optimization criterion. Therefore, we blanked out the temperature as a comparative parameter; the results are summarized in Table 4.8 (run04 and run07). The resulting temperature in the case of controlled temperature (run04) was

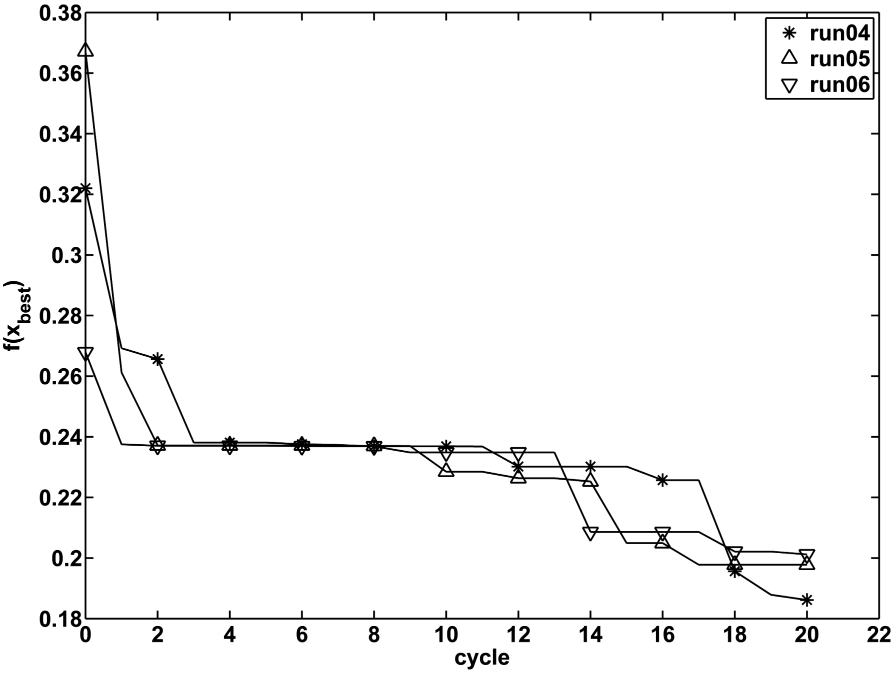

Figure 4.14.: Evolution of the overall error during the optimization of run04, run05 and run06.

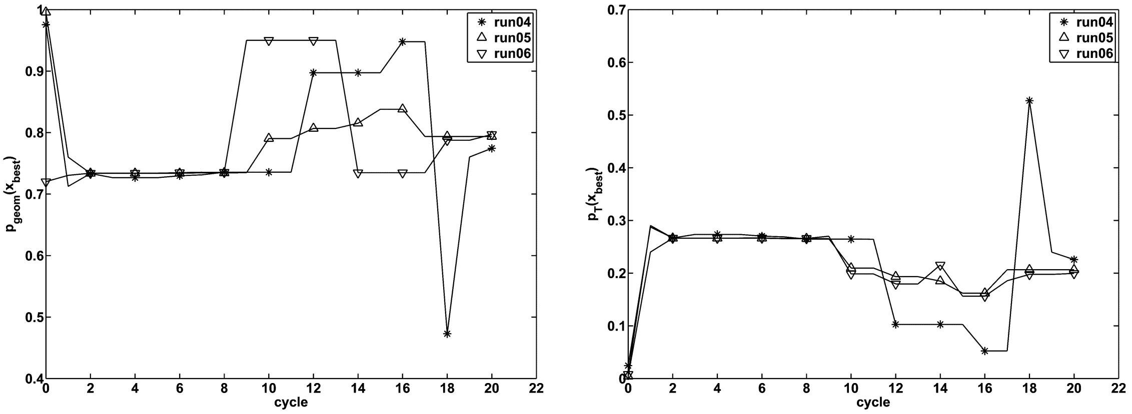

(a) (b)

Figure 4.15.: Geometric (a) and temperature (b) contribution to the overall error during the optimizations using modified setup parameters.

Table 4.7.: Results of the finite element calculations using the optimized parameters of Table 4.6

	$\mathbf{h_{pin}}$ **(mm)**	$\mathbf{h_{pinout}}$ **(mm)**	$\mathbf{d_{plate}}$ **(mm)**	$\mathbf{r_{plate}}$ **(mm)**	$\mathbf{T_{max}}$ **(°C)**	$\mathbf{f}$ **(**$\mathbf{x_{best}}$**)**
run04	0.778	0.782	0.160	0.636	3265	0.186
run05	0.715	0.719	0.161	0.636	3270	0.198
run06	0.782	0.714	0.208	0.636	3272	0.201
target	0.74	0.79	0.12	0.79	3000	

Table 4.8.: Comparison of optimization cycles using the temperature as a criterion (run04 and run08, T_{target}=3000°C) and those without (run07 and run09), all other simulation parameters were equal for all of the calculations below: $SN = 15$, $CN = 20$.

run	$\mathbf{h_{pin}}$ **(mm)**	$\mathbf{h_{pinout}}$ **(mm)**	$\mathbf{d_{plate}}$ **(mm)**	$\mathbf{r_{plate}}$ **(mm)**	$\mathbf{T_{max}}$ **(°C)**	$\mathbf{f}$ **(**$\mathbf{x_{best}}$**)**	$\mathbf{T_{target}}$ **(°C)**	**Error function**
04	0.778	0.782	0.160	0.636	3265	0.186	3000	absolute
07	0.714	0.782	0.159	0.636	3301	0.161	-	absolute
08	0.713	0.781	0.115	0.578	3130	0.278	3000	normalized
09	0.712	0.781	0.117	0.636	3324	0.201	-	normalized

slightly higher than in the run where the temperature was not a criterion (run07).

Error function

Another point we examined was how computing the error function (Equation 2.41) influences the optimization. Since the temperature is three orders of magnitude higher than the residual target values, we used Equation 4.13 to normalize the deviation. Applying this normalization scheme (Equation 4.13) to all comparative parameters (h_{pinout}, h_{pin}, d_{plate} and r_{plate}) we performed two optimizations.

In the first run the maximum temperature was a comparative parameter (run08) and in the second one the temperature was not controlled (run09). Table 4.8 shows the results of these optimizations. Like in the case of the calculations without normalized errors, the maximum temperature is a little higher in the temperature controlled simulation than in the uncontrolled case.

Normalizing all comparative parameters has just a small impact on the overall results. This may be because the comparative parameters h_{pin}, h_{pinout} etc. have the same orders of magnitude. The resulting quantity d_{plate} is significantly closer to its target value of 0.12 mm in the runs with normalized errors. Table 4.8 gives the optimized parameters of Goldak's heat source from the optimizations run07, run08 and run09.

Table 4.9.: Optimized parameters of Goldak's heat source of run07 to run09. The number of optimization cycles ($CN = 20$) and parameter sets ($SN = 15$) was constant. In run07 there wasn't a target temperature and in the run08 and run09 the error function was normalized according to Equation 4.13

	$\mathbf{x_1}(\mathbf{x_{0,\mathrm{pin}}})$	$\mathbf{x_2}(\mathbf{y_{0,\mathrm{pin}}})$	$\mathbf{x_3}(\mathbf{f_{\mathrm{pin}}})$	$\mathbf{x_4}(\mathbf{x_{0,\mathrm{plate}}})$	$\mathbf{x_5}(\mathbf{y_{0,\mathrm{plate}}})$	$\mathbf{x_6}(\eta)$
run07	0.834	0.639	0.688	1.137	0.026	0.790
run08	0.843	0.751	0.685	1.159	0.037	0.816
run09	0.866	0.489	0.637	1.460	0.048	0.891

Influence of the rejection limit

In a last investigation we examined the influence of the parameter L (limit of rejections) on the optimization. In doing so we ran an optimization with the same parameters as in run04 but L was set to 5 instead of 10. The development of the overall error is illustrated in Figure 4.16. During the first few cycles $\mathbf{f}(\mathbf{x}_{\mathrm{best}})$ drops faster with $L = 10$ but as the optimization continues the overall error of the calculation the computation with $L = 5$ shows a stronger decrease.

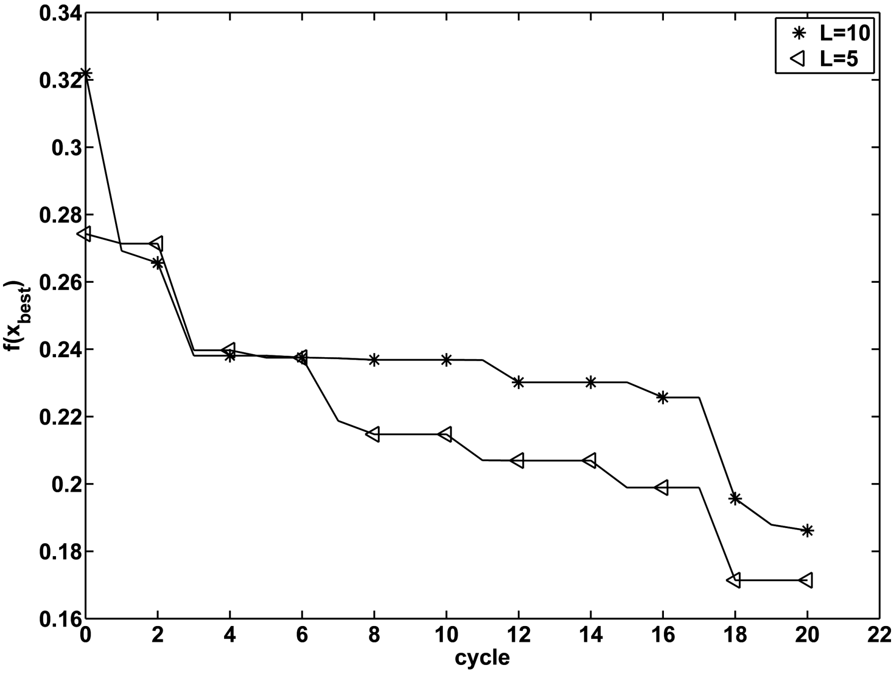

Figure 4.16.: Comparison of the overall error's evolution using different values of the parameter L

Table 4.10.: Relative errors of the simulated weld pool geometry with respect to the target values of Table 4.2.

run	$\mathbf{\Delta h}_{\mathrm{pin}}$ (%)	$\mathbf{\Delta h}_{\mathrm{pinout}}$ (%)	$\mathbf{\Delta d}_{\mathrm{plate}}$ (%)	$\mathbf{\Delta r}_{\mathrm{plate}}$ (%)
run01	5.5	1.8	39	42
run02	3.0	9.7	40	34
run03	5.4	1.4	34	19
run04	5.1	1.0	33	19
run05	3.4	9.0	34	19
run06	5.7	9.6	73	19
run07	3.5	1.0	33	19
run08	3.6	1.1	4	27
run09	3.8	1.1	3	19

Summary

Eventually, Table 4.10 gives the relative errors of the calculated weld pool parameters of all optimizations. First one can observe that the errors of h_{pin} and h_{pinout} are smallest for all optimization runs virtually independent of the optimization parameters (number of parameter sets, normalized error function and T_{target}).

The best results in terms of simulated weld pool geometry were achieved by using a normalized error function and no target temperature. The largest error is that of r_{plate}. Even in run09 which shows the best results for all parameters $\Delta r_{\mathrm{plate}}$ is still at 19%.

In conclusion we state that there are three major factors influencing the optimization. First the number of parameter sets SN has a considerable impact on the optimized results. As depicted in Figure 4.11 $f(\mathbf{x}_{\mathrm{best}})$ gets smaller with increasing SN.

The temperature as an optimization criterion plays only a minor role with respect to the shape of the molten zone as we compare run03 to run07 in Table 4.10.

The third factor is the error function itself. We found that normalizing all comparative parameters according to equation 4.13 resulted in a major enhancement of the results. Nevertheless, even after using normalized error functions the error of $\mathbf{r}_{\mathrm{plate}}$ is still high. This deviation may come stem from the mesh used in the FE simulation. Since the molten zone's expansion in the simulation is dependent on the refinement of the used mesh, using a finer mesh could bring improvement here. However, using a finer mesh leads to an increased computing time and so one has compromise between accuracy and computational effort.

4.2. Numerical analysis of the heat input on the base material in the case of aluminum pin welding

In order to understand the processes concerning the combined heat input of laser and arc in the context of welding aluminum pins (Section 3.1.2) we conducted some simple finite element analyses. In doing so we only focused on the heat input on the plate. The arc's heat input was modeled using the Goldak heat source [6] which reads for the two dimensional case like this:

$$q = \eta \frac{6UI}{x_0 y_0 \pi} \mathrm{e}^{-3\left(\frac{x}{x_0}\right)^2} \mathrm{e}^{-3\left(\frac{y}{y_0}\right)^2} \tag{4.14}$$

In Equation 4.14 x_0 and y_0 are geometry parameters, U and I are the arc voltage and the arc current, respectively. The entity η denotes the efficiency of the heat source. The heat input of the laser was simulated by a modified version of Goldak's heat source, it reads as follows:

$$q = \frac{6\ P_l\ \alpha\ \cos(\phi)}{\pi x_0 y_0} \mathrm{e}^{-3\left(\frac{x}{x_0}\right)^2} \mathrm{e}^{-3\left(\frac{y}{y_0}\right)^2}. \tag{4.15}$$

Equation 4.15 looks similar to equation 4.14, P_l is the laser's power. The term $\cos(\phi)$ in Equation 4.15 describes the loss of power due to the incidence angle ϕ of the laser. The entity α is the fraction of absorption depending on the material's surface properties. The values for the parameters in Equations 4.14 and 4.15 are listed in Table 4.11.

Table 4.11.: Values of the parameters in Equation 4.14 and 4.15 as used in the FE analyses.

	$\mathbf{x_o}$ (mm)	$\mathbf{y_o}$ (mm)	$\boldsymbol{\eta}$	$\mathbf{P_l}$ (W)	**U** (V)	**I** (A)	$\boldsymbol{\phi}$	$\boldsymbol{\alpha}$ (from [40])
arc	0.9	0.1	0.85	-	80	15	-	-
laser	0.1	0.03	-	780	-	-	34°	0.4

In order to determine the laser's influence on the overall heat input we performed a calculation with only the arc burning for 30 ms without laser. We then conducted a second analysis with the laser active 200 ms prior to the arc ignition and during the arc burning for another 15 ms.

The resulting temperature distributions are depicted in Figure 4.17. The temperature field resulting from the combined laser and arc process shows a deeper penetration of the molten zone into the base material than in the arc only case. The deeper heat penetration is consistent with experimental observation as depicted in Figure 3.5 on page 32. Here, one can observe a much more distinct dilution within the fusion zone of the laser pretreated surfaces, whereas the samples without laser treatment show hardly any dilution.

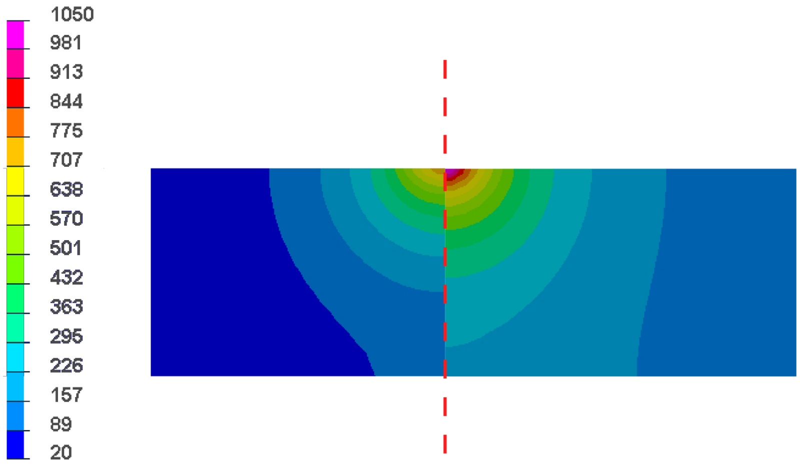

Figure 4.17.: Comparison of the temperature distribution within the base material. The right half of the picture shows the distribution of laser and arc, the left side the distribution of arc only.

Figure 4.18 shows the surface temperature at the weld spot over time. In the case of the laser pretreatment the temperature is considerably higher compared to the case with the arc only. The laser preheating is clearly visible, it heats the surface almost to melting temperature. The significant rise of the temperature after 200 ms marks the point when the arc kicks in elevating temperatures to some 1050°C, but only for a few microseconds. As reported in the work of Rechner et al. [41] such short heating removes impurities from the surface and activates it.

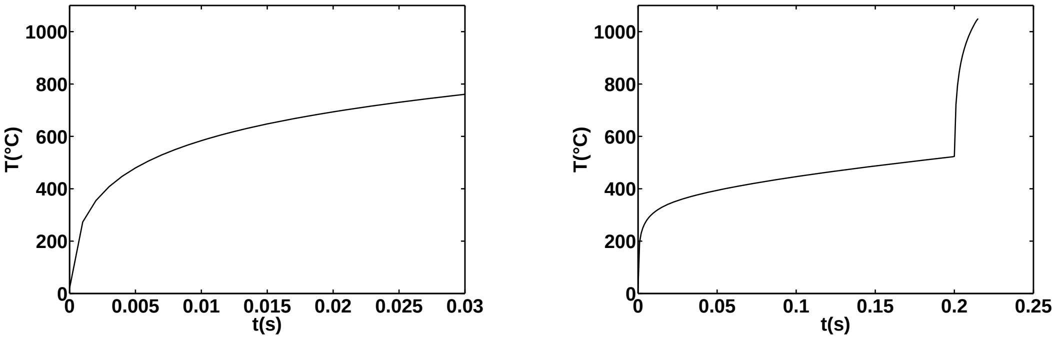

(a) (b)

Figure 4.18.: Temperature over time of the surface at the welding spot without (a) and with laser (b)

4.3. Mechanical calculations of a single pin

In order to find out more of the mechanical behavior of a single pin we performed simulations of shear tests. Since the setup for shear tests is not axial symmetric anymore we were forced to abandon the radial symmetric model used in the electro-thermomechanical calculations described in Section 4.1. In doing so we elaborated a SIL script (Appendix C.2) being capable of transferring the results (e.g. stresses, strains ...) of the simulations of Section 4.1 from a radial symmetric model to an actual 3D model as follows:

1. Prior to the actual transformation a 3D mesh was generated by spinning the axial symmetric mesh around its rotational axis. Using this new mesh a single simulation step was executed in order to obtain an empty result file of the 3D system.

2. The next step was to identify the elements of the 3D model with their counterparts in the radial symmetric mesh.

3. Now we were able to transfer the data read from the axial symmetric result file to the empty 3D model. All the data from the nodes, elements and integration points were transferred.

Figure 4.19 shows exemplary the transfer of the residual stresses in y-direction from the axial-symmetric calculations (4.19a) to the 3D model (4.19b). Using the 3D model we performed simulations of shear test. In doing so, the front nodes of the base material (compare Figure 4.20) were fixed and at the opposite nodes at the pin a velocity of 0.1 mms^{-1} in x-direction was applied. In order to detect failure we used two very simple criteria

von Mises This criterion has already been mentioned in Section 2.3.2. According to Läpple [42] failure occurs if the von Mises stresses σ_{Mises} exceeds the yield stress, i.e.

$$\sigma_{\text{Mises}} = \sqrt{\frac{1}{2}(\sigma_{11}-\sigma_{22})^2 + (\sigma_{22}-\sigma_{33})^2 + (\sigma_{33}-\sigma_{11})^2 + 6(\sigma_{12}^2+\sigma_{23}^2) + \sigma_{13}^2} \geq R_{p,0.2} \tag{4.16}$$

Tresca In this criterion the equivalent stress is computed according to Tresca

$$\sigma_{\text{Tresca}} = \max(|\sigma_{11}-\sigma_{22}|, |\sigma_{22}-\sigma_{33}|, |\sigma_{33}-\sigma_{11}|) \tag{4.17}$$

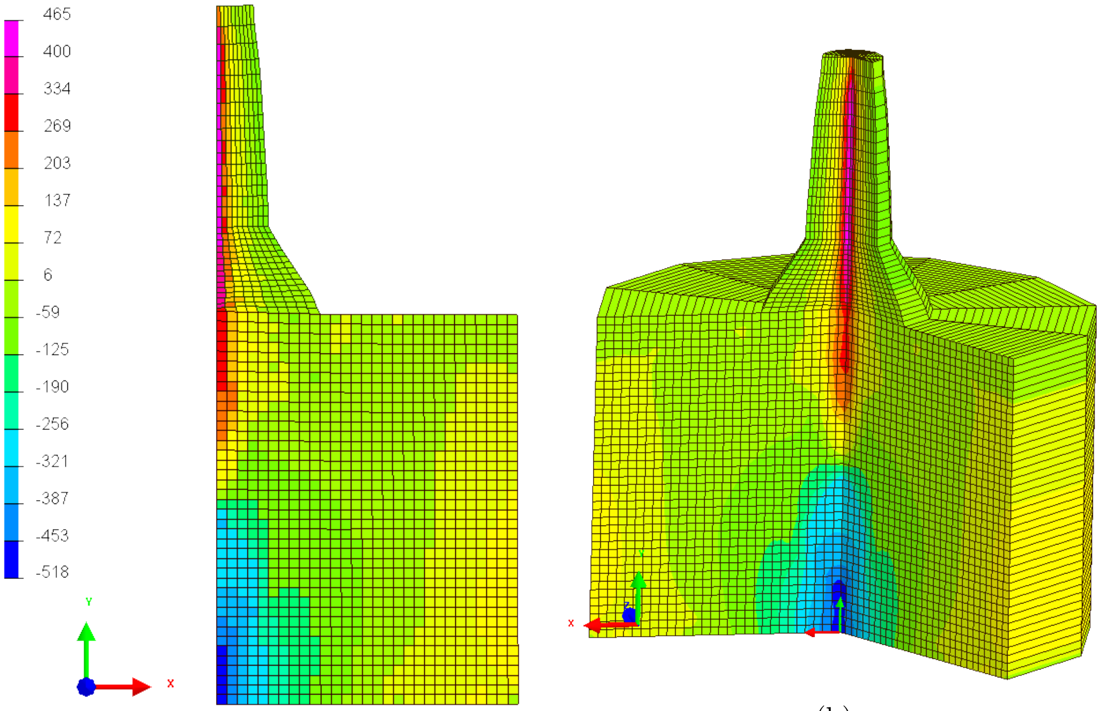

(a)

(b)

Figure 4.19.: Axial-symetric to 3D transform of the stresses in y-direction.

The criteria explained above may also be applied using strains instead of stresses. In this case the threshold for deactivating an element is in analogy to the $R_{p0.2}$ limit

$$\epsilon_{\text{equiv}} \geq 0.2 \tag{4.18}$$

with ϵ_{equiv} being either the von Mises or Tresca equivalent strains.

The results of the simulations using stress based failure criteria (Equations 4.16 and 4.17) are depicted in Figure 4.21a. The Tresca criterion yields a little lower maximum force than the von Mises criterion. Furthermore the force level drops quicker in the case of applying the Tresca criterion and the ultimate strain is only half as it is in the case of the von Mises criterion. In the surrounding of the force maximum the calculation using the Tresca criterion exhibit a very sharp peak whereas in the case of the von Mises criterion the maximum is approached smoothly followed by a sharp drop.

Using strain based criteria (see Figure 4.21b) on the other hand does not result in such strong deviation between von Mises and Tresca criterion as it is the stress based case.

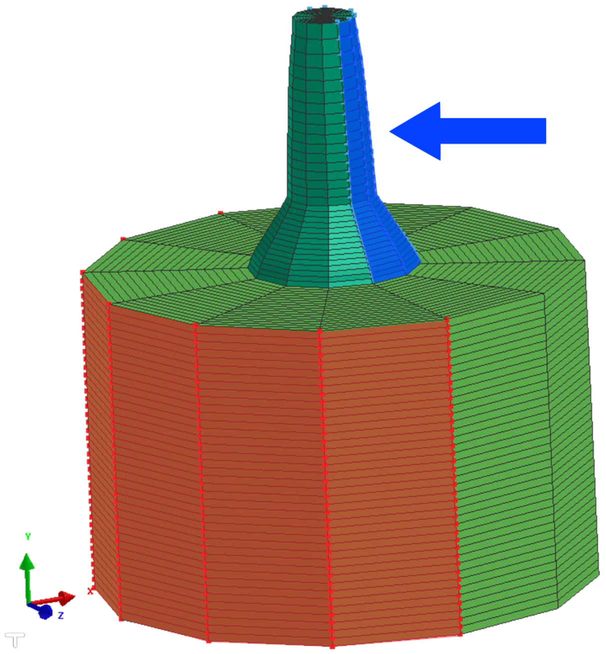

Figure 4.20.: Simulation setup for the shear test simulations. The marked nodes at the left hand side were restrained from moving, at the nodes at right hand side of the pin a velocity of 0.1 mms^{-1} in x-direction was set.

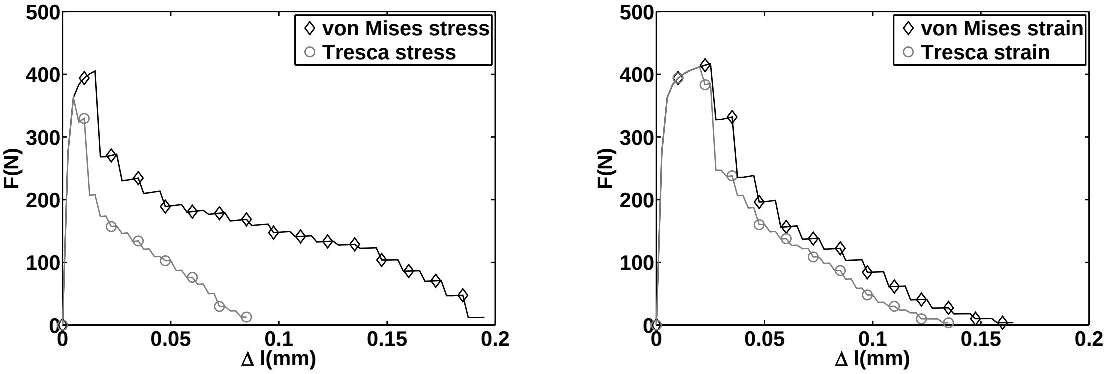

(a) Stress based criterion

(b) Strain based criterion

Figure 4.21.: Resulting force-displacement curves of the simulated shear tests using the setup as illustrated in Figure 4.20

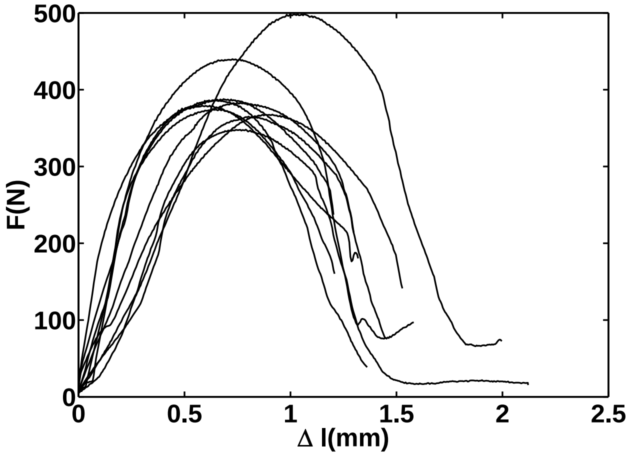

Figure 4.22.: Experimental force-displacement curves of shear tests performed with a single pin.

Comparing the simulated findings (Figure 4.21) with the force displacement-curves of Figure 4.22 reveals that the simulations predict the level of the maximum force pretty well.

However, when it comes to displacements the simulation underestimates the fracture stroke by roughly one order of magnitude. This deviation is due to the fact that in these very simple criteria used here the failure occurs instantaneously after the equivalent stresses or strains are exceeded. For more realistic modeling it is necessary to apply more sophisticated failure models.

4.4. Modeling of a dissimilar joint

This section is about applying a cohesive zone contact formulation (as described in Section 2.4.3) in order to model a pin reinforced joint between carbon fiber reinforced plastic (CFRP) and a stainless steel plate. Various authors have already used the cohesive zone model to numerically simulate joints (see Goyal et al [43], Anyfantis and Tsouvalis [44] or Gonçalves et al [45]). However, the above mentioned investigations dealt only with adhesively bonded cases, in our studies we aimed to extend the existing model to joints enhanced with pin structures. Instead of simulating every single pin in full detail we sought to find a model that uses only different contact conditions on the pins' sites.

4.4.1. Material model

The material properties of the stainless steel plate were assumed to be isotropic using the elasto-plastic behavior summarized in Appendix A.1.

We did not account for delamination within the CFRP and therefore we used an elastic homogenized approach [46] with the values of Uscnik and Staffenberger [47] listed in Table 4.12.

Table 4.12.: Stiffness parameters of a quasi-isotropic CFRP from [47]

$\mathbf{E}_x$ **(GPa)**	$\mathbf{E}_y$ **(GPa)**	$\mathbf{E}_z$ **(GPa)**	$\mathbf{G}_{xy}$ **(GPa)**	$\mathbf{G}_{xy}$ **(GPa)**	$\mathbf{G}_{xz}$ **(GPa)**	$\boldsymbol{\nu_{xy}}$	$\boldsymbol{\nu_{yz}}$	$\boldsymbol{\nu_{xz}}$
55.0	55.0	10.6	20.9	4.2	4.2	0.31	0.25	0.25

4.4.2. Simulation setup

In order to compare the simulated results with the experiment of Section 3.3 we chose the same geometry as in the experiments. The FE mesh used in the simulations is depicted in Figure 4.23. The calculations were carried out in Abaqus 6.11-2 [48] using a mesh of eight node brick elements of linear order. The nodes at the end of the metal plate were fixed while at the according nodes at the plastic's part a displacement of 1 mm/min in x-direction was defined.

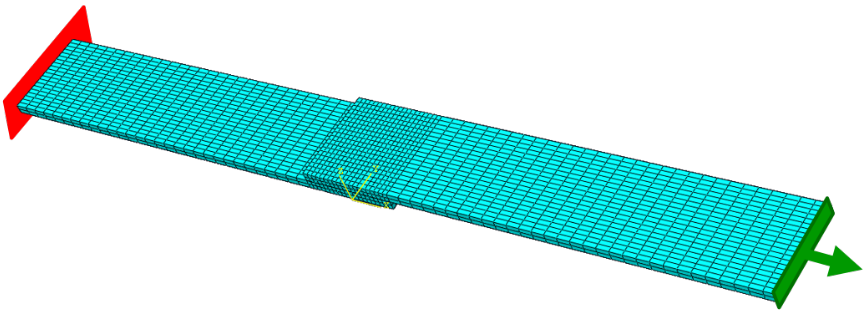

Figure 4.23.: Mesh used in the simulations of pin reinforced joints. The node at the left end (red square) were fixed and at the right hand nodes (green square) a displacement in x-direction was applied.

4.4.3. Contact formulations

Since a pin reinforced joint is a combination of an ordinary adhesive joint and parts where the pins are located we had to define two different cohesive potentials. In Figure 4.24 overlap area of the metal side is shown. Between the interface nodes of metal part and the interface surface of CFRP part we defined *node to surface* contact formulations.

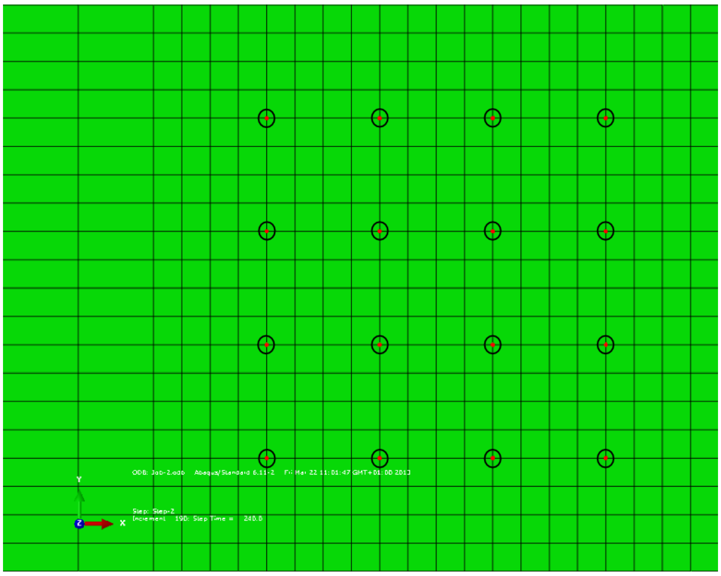

Figure 4.24.: Overview of the contact area in the shear lap simulations of pin reinforced joints. The highlighted nodes were assigned with the trapezoidal cohesive law describing the pins.

For the adhesive part we chose a traditional triangular cohesive potential described in term of energy as summarized in Table 4.13.

Table 4.13.: Cohesive parameters for the adhesively bonded parts of a pin reinforced joint; from [47]

$G_{I,c}$ ... critical energy release rate in normal direction
$G_{II,c}$ ... critical energy release rate in tangential direction
$\sigma_{\max,I}$ ... maximum stress in normal direction
$\sigma_{\max,II}$ ... maximum stress in tangential direction

$\mathbf{G_{I,c}(kJm^{-2})}$	$\mathbf{G_{II,c}(kJm^{-2})}$	$\boldsymbol{\sigma_{\max,I}}$**(MPa)**	$\boldsymbol{\sigma_{\max,II}}$ **(MPa)**
0.384	1.254	1.0	14.0

In order to find an appropriate cohesive formulations for the pins we chose an trapezoidal cohesive law following the work of Campilho and coworkers [30]. The reason for choosing such a cohesive law was that ductile materials have already been successfully described using the trapezoidal approach (e.g. Woelke et al [49]). The cohesive parameter of the pins are listed in Table 4.14. In case of cylindric pins the stiffness and maximum stress in normal and tangential[2] direction were equal (10 MPa). For the ball headed pins on we chose the maximum allowed stress in normal direction to be significantly higher than in the tangential direction. This strategy takes into account the fact that due to the ball headed shape the pin CFRP connection normal to the contact surface is very strong due to the pins' geometry. However, those parameters were chosen and modified in order to obtain agreeable result with respect to the experiments (see Figure 4.25).

The agreement with the experimental curves is in the case of the cylindric pins pretty good. Position and force level of the two significant peaks in the force-displacement diagram (Figure 4.25b) are predicted accurately, however after reaching its maximum the modeled curve drops to zero much quicker than in the experiments. The first drop of the force-displacement diagram results from failures of the adhesive layer between CFRP and metal. The following increase is then due to the pins acting as a mechanical barrier. Thus the second peak of the cylindric pin joint is at a lower force level than in case with ball headed pins.

In order to illustrate this behavior we executed calculation with adhesive and pin interaction only. The outcome is given in Figure 4.26 showing that the overall force-displacement curve is a combination of the adhesive only and pin only curve.

Regarding the deformation of the specimens after failure reveals that for ball headed pins the predicted deformation in the simulations show good agreement with the experiment as shown in Figure 4.27

---

[2] The term *normal* denotes the direction perpendicular to the plate surface (z-direction in Figure 4.23) and *tangential* parallel to the surface (x-direction)

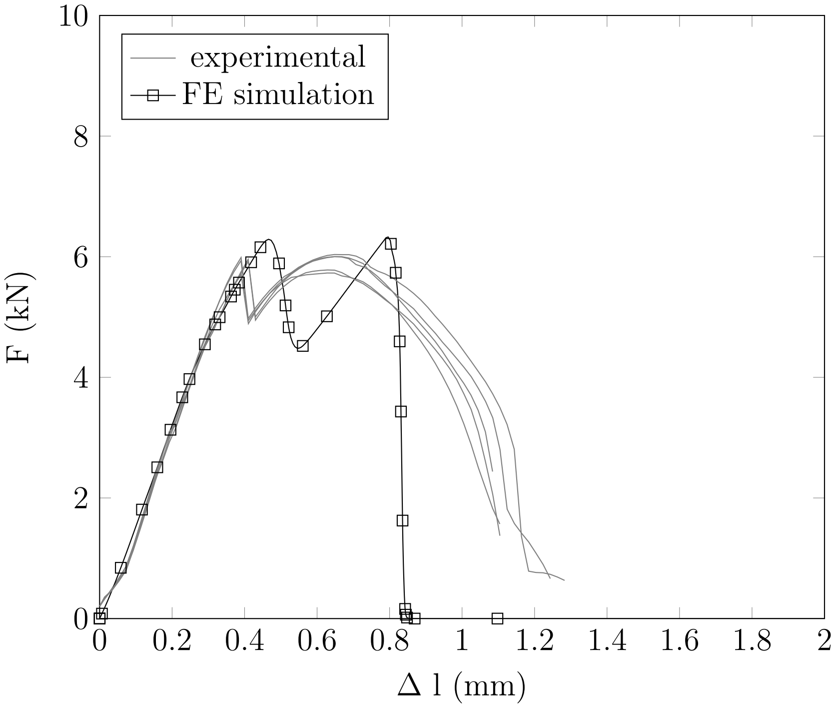

(a) Cylindric pin array

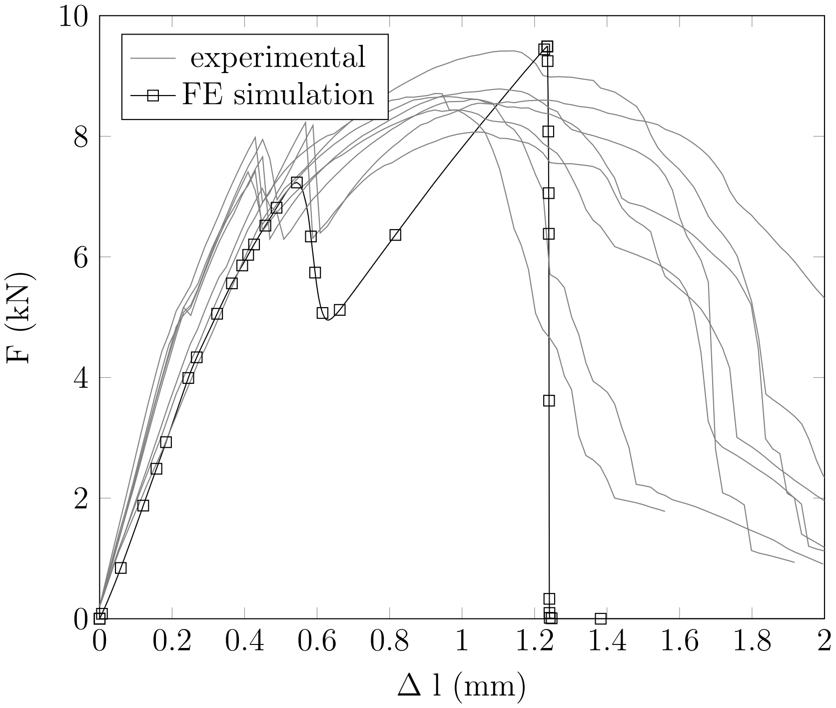

(b) Ball headed pin array

Figure 4.25.: Comparison of experimental and simulated force-displacement curves of pin enhanced joints.

Table 4.14.: Cohesive parameters of the pins ($\Delta = \delta_2 - \delta_1$), compare Figure 2.12 on page 22

		k (MPa/mm)	**$\boldsymbol{\sigma}_{\mathbf{max}}$ (MPa)**	**$\boldsymbol{\delta}_{\mathbf{f}}$ (mm)**	**$\boldsymbol{\Delta}$ (mm)**
ball headed	normal	$190 * 10^3$	190	0.05	0.001
	tangential	$84 * 10^3$	84	0.05	0.001
cylindric	normal	$100 * 10^3$	10	0.016	0.0009
	tangential	$100 * 10^3$	10	0.016	0.0009

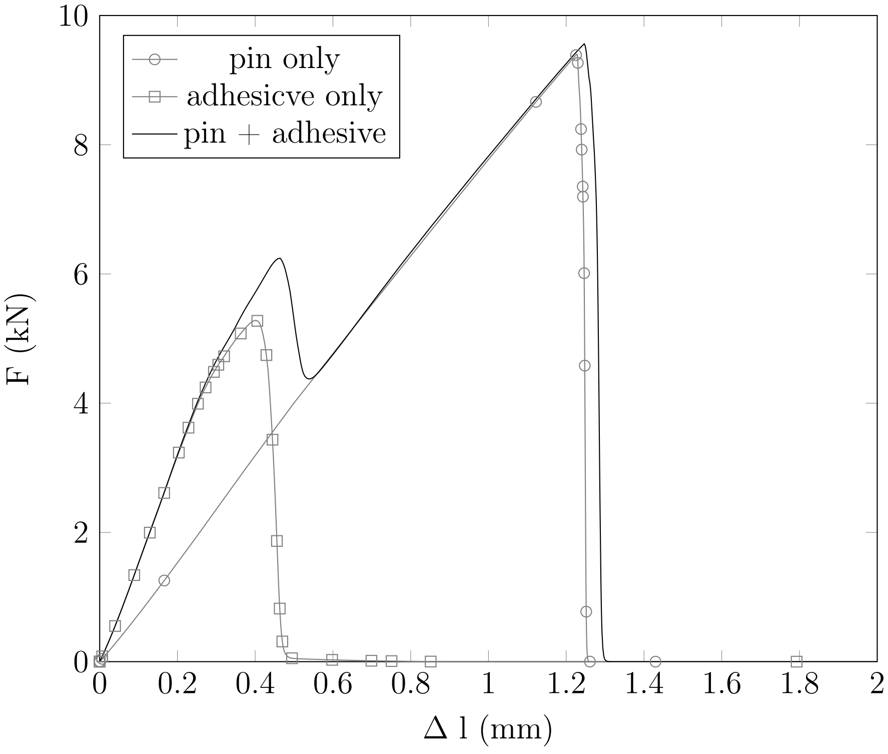

Figure 4.26.: Resulting simulated force-displacement curve as a result of adhesive and pin only curve of pin reinforced joint.

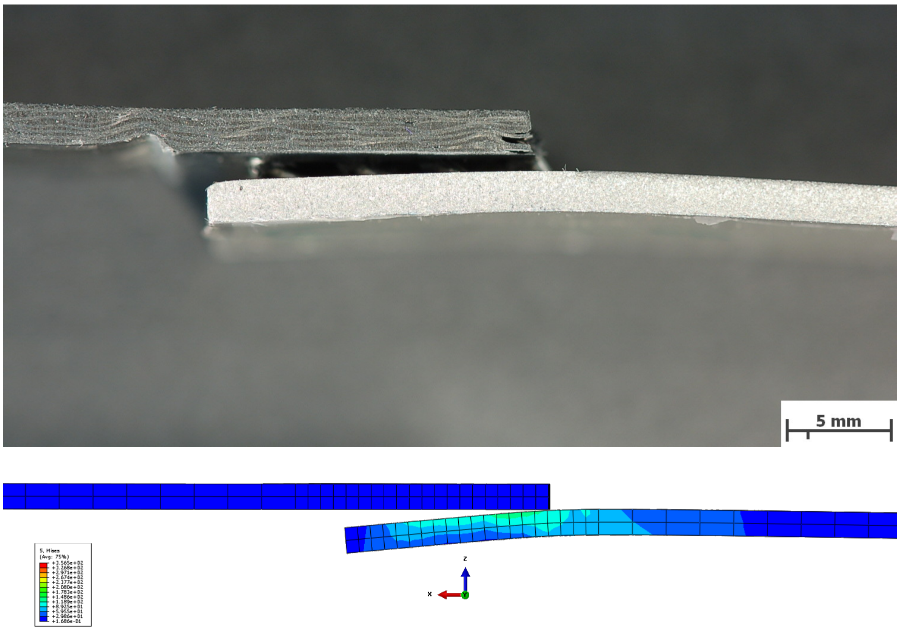

Figure 4.27.: Deformation of the broken specimens in experiment (top) and simulation (bottom)

4.4.4. Optimizing the cohesive parameters

Since the cohesive parameters in Table 4.14 were determined empirically we sought to optimize them in order to better meet the experimental curves. As already in the case of heat source optimization in Section 4.1.3 we used the ABC algorithm for this purpose.
The parameters we wanted to optimize were $\sigma_{\max}$ in normal and tangential direction and the parameters $\Delta = \delta_2 - \delta_2$ and δ_f.The initial stiffness k was given using $k = 10^3 \sigma_{\max}$ in the case of ball pins and $k = 10^4 \sigma_{\max}$ for cylindric pins.
The values of each parameter can be found in Table 4.15. Since it turned out that the stability of the calculation is very sensitive to those parameter we decided to choose them from a small range around the working parameter of Table 4.14. The target parameters were based on the force displacement curves from the experimental investigations (Section 3.3). In doing so we extracted the force displacement curves from the FE simulation and determined the following significant points:

- first maximum - $\max_1$
- minimum after drop - min
- second maximum - $\max_2$.

Table 4.15.: Parameters to be optimized and their upper and lower boundaries (compare Figure 2.12 on page 22)

	$\boldsymbol{\sigma}_{\mathbf{max,t}}$ **(MPa)**	$\boldsymbol{\sigma}_{\mathbf{max,n}}$ **(MPa)**	$\boldsymbol{\delta}_{\mathbf{1}}$ **[mm]**	$\boldsymbol{\delta}_{\mathbf{2}}$ **(mm)**
ball				
lower	150	30	0.002	0.045
upper	220	60	0.005	0.055
cylinder				
lower	5	5	0.0003	0.04
upper	20	20	0.0015	0.003

We then compared these values with those of Table 3.14 on page 51 using

$$f = \sqrt{\sum_{i=1}^{2}\left(\frac{x(i)^s_{\mathrm{max1}} - x(i)^e_{\mathrm{max1}}}{x(i)^e_{\mathrm{max1}}}\right)^2 + \sum_{i=1}^{2}\left(\frac{x(i)^s_{\mathrm{min}} - x(i)^e_{\mathrm{min}}}{x(i)^e_{\mathrm{min}}}\right)^2 + \sum_{i=1}^{2}\left(\frac{x(i)^s_{\mathrm{max2}} - x(i)^e_{\mathrm{max2}}}{x(i)^e_{\mathrm{max2}}}\right)^2} \tag{4.19}$$

with f being the error function as introduced in Section 2.5 (equation 2.39). The components with a superscript s in equation 4.19 refer to the simulated values and those with an e to experimental results. The entities $x(i)$ in equation 4.19 are the two components describing the position of the significant points of the force displacement curves. For the vector $\mathbf{x}_{\mathrm{max1}}$ this reads as

$$\mathbf{x}_{\mathrm{max1}} = (x_{\mathrm{max1}}(1), x_{\mathrm{max1}}(2)) = (\Delta l_{\mathrm{max1}}, F_{\mathrm{max1}})$$

So the basic steps in order to get a value for f in the context of the ABC optimization were:

1. Setting up an input file with the parameters in Table 4.15.
2. Running a FE simulation with that input file
3. Extract the simulated force displacement curve from the result files.
4. Determine the characteristic points described above.
5. Evaluate f according to equation 4.19.

The rest of the ABC optimization was executed as described in Figure 2.13 of Section 2.5 on page 23.

In Figure 4.28 the numerical results using the optimized cohesive parameters and the experimental curves are compared. For those optimizations we used 20 parameter sets

Table 4.16.: Optimized results of the characteristic points in the force displacement curves using the ABC algorithm.

	cylinder		**ball**	
	Δ l (mm)	**F (kN)**	**Δ l (mm)**	**F (kN)**
$\max_1$	0.52	7.1	0.51	7.1
min	0.61	4.9	0.62	5.0
$\max_2$	0.66	5.2	1.10	8.3
f	0.614		0.372	

Table 4.17.: Optimized cohesive parameters for cylindric and ball pins.

	$\boldsymbol{\sigma}_{\text{max,n}}$**(MPa)**	$\boldsymbol{\sigma}_{\text{max,t}}$ **(MPa)**	**Δ(mm)**	$\boldsymbol{\delta_f}$ **(mm)**
ball	210.8	41.9	0.0028	0.049
cylindric	9.07	8.7	0.0014	0.014

($SN = 20$) and 15 optimization cycles ($CN = 15$). In Table 4.16 the best values of the simulated target parameters and the value of their error function f. Further, the cohesive parameters resulting from the optimization are listed in Table 4.17. Evaluating term 4.19 for the results of the calculations with the parameters in Table 4.14 gives

$$f_{\text{cylinder}} = 0.463$$
$$f_{\text{ball}} = 0.477$$

Comparing these results to the optimized ones of Table 4.16 reveals that only in the case of they ball pins further improvement was achieved. The optimization in case of cylindric pins does not yield any improvement.

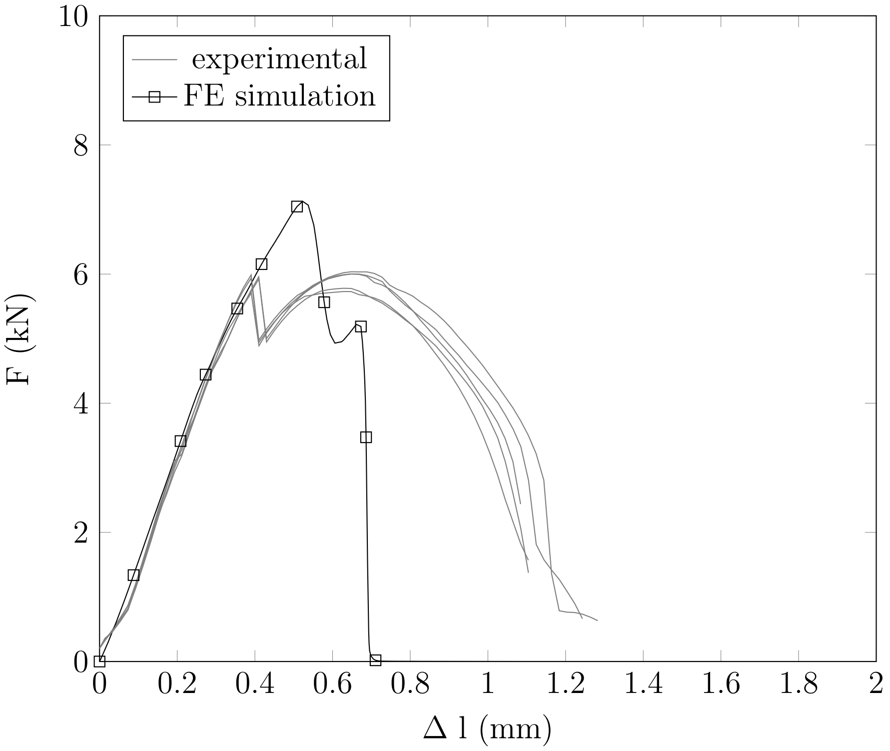

(a) cylindric pins

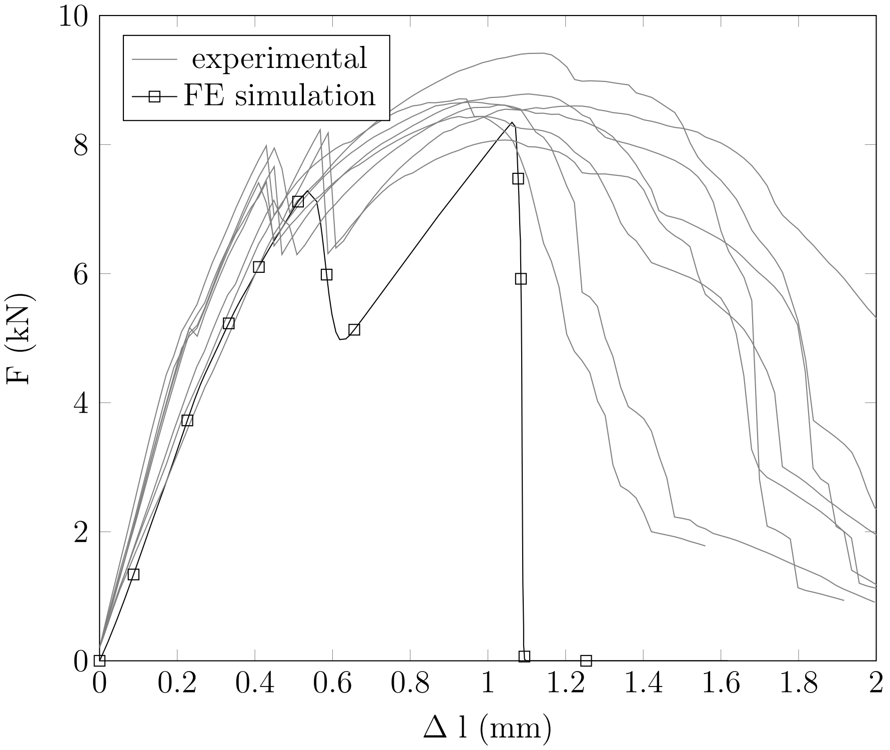

(b) ball pins

Figure 4.28.: Comparison of experimental and simulated force displacement curve after ABC optimization of the cohesive parameters

5. Summary and conclusion

The overall goal of this work was to acquire a deeper understanding of the pin welding process on the one hand and to describe the influences of pins on dissimilar joints.

Metallographic investigations of pins of stainless steels and aluminum lead to the conclusion that in case of stainless steel a well defined geometry can be achieved. Comparing the interface between pin and base material reveals that the interface quality of the stainless steel pins is better than in the case of aluminum, as far as porosity and alignment is concerned.

The final quality of classic CMT aluminum pins depends very much on the surface pretreatment. We could show that surface activation using a laser results in a significant reduction of pores in the connection area of pin and base substrate. However, the misalignment of pin axis and center point of the weld spot could be reduced but not eliminated totally.

A further drawback of CMT aluminum pins was their height. Since for many application in the automotive industry maximum tolerated height are below 2 mm, which can not be achieved using the classic CMT process.

Another way of generating pins is by use of the drop by drop method. Microscopic investigations of such pins revealed that in some cases the pin plate junction is good but in other cases quite poor. Since these differences were independent of the base material we conclude that possibly the surface pretreatment (cleaning) which was not taken care of has a crucial influence on the eventual weld quality as it is the case with classic CMT pins.

Another point was to investigate the influence of the pin welding process on the base material's mechanical properties. In doing so we conducted tensile tests using specimens with different number of pins on them. We performed such tests on several material ranging from stainless steel over micro-alloyed steels to aluminum. We found that only in the case of aluminum alloys of the 6xxx series a reduction of the fracture elongation occurs, independent of the number of pins. Drop by drop pins of the 6xxx series did not show such a distinct drop of the ultimate strain as the ordinary CMT pins.

For the sake of completeness we compared these results with those of electron beam modified surfaces of Tändl et al [16]. Pins generated by EBW showed a significant drop regarding the ultimate strain, and with increasing number of pins we observed decreased tensile strength as well. In contrast to CMT pins the base material's failure results from a cross section reduction due to the EBW process which explains the lower performance of the EBW pins.

After having investigated the issues occurring in the context of the welding process of pins we studied the influence of pins in a real dissimilar joint of stainless steel and carbon fiber reinforced plastics (CFRP). In doing so we conducted single lap shear test of specimens with an array of 4x4 pins on the overlap area. The force displacement curves of these tests show a distinct shape. After reaching a first maximum the force level drops roughly 1.5 kN before it increases again up to a second maximum. The overall level of these two maxima as well as the relative difference of them depends on the kind of the involved pins.

Ball headed pins exhibit a higher force level than cylindric pins. The second force maximum is considerably higher than the first one whereas in the case of cylindric pins the two maxima are at the same level. Comparing these findings with force displacement diagrams of specimens without pins reveals that the pins increase the ultimate fracture elongation.

Regarding the fracture patterns, it is evident that in the case if cylindric pins, the pins are bent and then pulled put out of the CFRP laminate. Ball headed pins on the other hand seem to be more difficult to be pulled out of the laminate, some are sheared of completely and others are also bent but still attached to the substrate.

However, fracture elongation increases only little when using pins because after the first peak fracture already sets in but the second force elevation may serve as a safety margin for crash relevant applications.

Based on the findings of experimental investigations we simulated the welding process of a single pin making use of finite element analysis. In doing so, we adopted Goldak's heat source for the axial symmetry of the problem. Furthermore, we elaborated a routine being capable of coupling electro-thermal and mechanical calculations in order to take into account the cross section's change of the wire during the shaping phase in the pin welding process. In the course of these investigations we obtained a deeper insight of the welding process, especially, the migration of the zone of maximum temperature into the wire during the cooling stage. Furthermore, we were able to show that the hottest zone becomes more localized during the shaping stage by taking into account the thermal-electrical and mechanical coupling.

Further refinement, in terms of congruence of experimental and simulated molten zone, was achieved by applying an optimization algorithm aiming to find optimal geometry parameter for the Goldak model. The algorithm of choice was the *artificial bee colony* (ABC) algorithm conceived by Karaboga and Basturk [31].

Numerical investigations were carried out in the case of aluminum in order to calculate the temperature distribution during pin welding within the base material. As a result we could explain the increased interface quality due to surface activation and cleaning by laser pretreating.

From simulating shear tests of a single pin using quite simple failure criteria (von Mises and Tresca) we learned that they predict the maximum force quite accurate. However, as far as fracture elongation was concerned there was clear divergence between simulations and experiments.

In order to find a simplified mechanical model for dissimilar joints reinforced with pins we set up a model based on this *cohesive zone* model. In a first attempt we used empirical data for the cohesive parameters. Using those parameters yielded force displacement curves that matched the experimental ones pretty well, especially in the case of ball headed pins.

Furthermore we applied the ABC algorithm in order to find optimized parameters for the pins' cohesive zone model. This worked out pretty fine for the ball pins, but did not bring any improvement for the cylindrical pins.

However, the parameters for the cohesive zone model were actually obtained empirically. Thus in order to get more accurate results, specifically experimental investigations such as double cantilever beam, end notch flexure and mixed mode bending test are required (compare the work of Camanho et al.[27]). Especially, the mode mixing (see Section 2.4.3) and the related failure mechanisms as shearing-off and bending of pins should be further investigated. Anoher point is that in our studies we only used the cohesive zone model for describing the contact between two solids. Further refinement may be achieved by using 3D cohesive interface elements on the one hand and by implementing more complex cohesive potentials on the other hand. Similar studies for pure adhesive joints have been carried out by Anyfantis et. al [44, 50].

Bibliography

1. Franco, G., Fratini, L., Pasta, A. & Ruisi, V. F. On the self-piercing riveting of aluminium blanks and carbon fibre composite panels. *International Journal of Material Forming* **6,** 137–144 (Oct. 2011).
2. Matsuzaki, R., Shibata, M. & Todoroki, A. Improving performance of GFRP/aluminum single lap joints using bolted/co-cured hybrid method. *Composites Part A: Applied Science and Manufacturing* **39,** 154–163 (Feb. 2008).
3. Szlosarek, R., Karall, T., Enzinger, N., Hahne, C. & Meyer, N. Mechanical Testing of Flow Drill Screw Joints Between Fibre-Reinforced Plastics and Metals. *Materials Testing* **55,** 737–742 (Oct. 2013).
4. Schierl, A. The CMT - Process - A Revolution in welding technology. *Welding in the World* **49,** 38 (2005).
5. Ucsnik, S., Scheerer, M., Zaremba, S. & Pahr, D. H. Experimental investigation of a novel hybrid metal–composite joining technology. *Composites Part A: Applied Science and Manufacturing* **41,** 369–374 (2010).
6. Goldak, J., Chakravarti, A. & Bibby, M. A new finite element model for welding heat sources. *Metallurgical and Materials Transactions B* **15,** 299–305 (1984).
7. Haslinger, B. An der Grenze des Lichtbogenschweißens. *Schweiss- und Prüftechnik* **4,** 52–54 (2010).
8. Schultz, H. *Electron beam welding* (Abington publishing, Cambridge, UK, 1993).
9. Kou, S. *Welding Metallurgy* 2nd (John Wiley and Sons, New York, USA, 2003).
10. Dance, B. G. I. & Buxton, A. L. *An Introduction to Surfi-Sculpt Technology - New Opportunities, New Challenges* in *7th International Conference on Beam Technology* (Halle, Germany, 2007).
11. Wang, X. *et al. Application of electron beam surfi-sculpt technology during composites materials joining* in *8th International Conference on Beam Technology* (Halle, Germany, 2010).

12. Wang, X., Guo, E., Gong, S. & Zhao, H. *Study of electron beam surfi-sculpt technology based on control of magnetic field* in *2nd International Electron Beam Welding Conference* **285** (DVS Media, Aachen, Germany, 2012), 54–57.
13. Buxton, A. L., Oluleke, R. & Prangnell, P. *Generating and assessing the quality and functionality of EB structured surfaces for dissimilar material joints* in *2nd International Electron Beam Welding Conference* (Aachen, Germany, 2012).
14. Reisgen, U., Otten, C., Fischer, H. & Panfil, C. *Electron Beam Structurisation of Titanium Materials for Medical Applications: Potential for Improved Bone Ingrowth Behaviour* in *64th Annual Assembly and International Conference of the International Institute of Welding* (2011).
15. Reisgen, U., Otten, C., Fischer, H. & Panfil, C. *Electron beam structurisation of titanium materials for medical applications: potential for improved bone ingrowth behaviour* in *2nd International Electron Beam Welding Conference* (DVS-Berichte, Band 285, Aachen, 2012), 68–71.
16. Taendl, J., Wittwer, L. & Enzinger, N. Erzeugung von Pinstrukturen mittels Elektronenstrahloberflächenbehandlung. *Schweiss- und Prüftechnik,* 32–35 (2013).
17. Goldak, J. & Akhlaghi, M. *Computaional Welding Mechanics* (Springer New York, New York, USA, 2005).
18. Sormann, H. *Ausgewählte Kapitel aus Numerische Methoden in der Physik, Finite Elemente* tech. rep. (Institute of Theoretical and Computational Physics, TU Graz, Graz, 2012). <`http://itp.tugraz.at/LV/sormann/AKNumPhysik/`>.
19. Schwarz, H. R. *Methode der finiten Elemente* (Teubner, Stuttgart, 1980).
20. Zienkiewizc, O. & Taylor, R. *The finite element method, Volume 1 The Basis* 5th (Butterworth Heinemann, 2000).
21. Joshi, S., Hildebrand, J., Aloraier, A. S. & Rabczuk, T. Characterization of material properties and heat source parameters in welding simulation of two overlapping beads on a substrate plate. *Computational Materials Science* **69,** 559–565 (Mar. 2013).
22. Zienkiewizc, O. & Taylor, R. *The finite element method, Volume 2 Solid Mechanics* 5th, 477 (Butterworth Heinemann, 2000).
23. Alfano, G. & Crisfield, M. A. Finite element interface models for the delamination analysis of laminated composites: mechanical and computational issues. *International Journal for Numerical Methods in Engineering* **50,** 1701–1736 (Mar. 2001).

24. Barenblatt, G. I. in *Advances In Applied Mechanics* (eds H.L. Dryden Th. von Kármán, G. K. F. H. v. d. D. & Howarth, L.) 55–129 (Elsevier, 1962). doi:`10.1016/S0065-2156(08)70121-2`. <`http://www.sciencedirect.com/science/article/pii/S0065215608701212`>.

25. Hillerborg, A., Modéer, M. & Peterson, P. E. Analysis of crack formation and crack growth in concrete by means of fracture mechanics and finite elements. *Cement and Concrete Research* **6,** 773–782 (1976).

26. Tvergaard, V. & Hutchinson, J. W. The influence of plasticity on mixed mode interface toughness. *Journal of the Mechanics and Physics of Solids* **41,** 1119–1135 (June 1993).

27. Camnho, P. P., Davila, C. G. & de Moura, M. F. Numerical Simulation of Mixed-Mode Progressive Delamination in Composite Materials. *Journal of Composite Materials* **37,** 1415–1438 (Jan. 2003).

28. Wu, E. M. & Reuter, R. *Crack extension in fibreglass reinforced plastics* tech. rep. 2 (Departement of theoretical and applied mechanics, University of Illinois, Chicago, USA, 1965), 31. <`http://www.dtic.mil/cgi-bin/GetTRDoc?AD=AD0613576`>.

29. Benzeggagh, M. & Kenane, M. Measurement of mixed-mode delamination fracture toughness of unidirectional glass/epoxy composites with mixed-mode bending apparatus. *Composites Science and Technology* **56,** 439–449 (Jan. 1996).

30. Campilho, R., de Moura, M. & Domingues, J. Using a cohesive damage model to predict the tensile behaviour of CFRP single-strap repairs. *International Journal of Solids and Structures* **45,** 1497–1512 (Mar. 2008).

31. Karaboga, D. & Basturk, B. A powerful and efficient algorithm for numerical function optimization: artificial bee colony (ABC) algorithm. *Journal of Global Optimization* **39,** 459–471 (Apr. 2007).

32. Wittwer, L., Jank, N., Becirovic, A., Waldhör, A. & Enzinger, N. *Influences on the arc stability in welding process of pin structures* in *Proceedings of 13th International Conference on Aluminum Alloys* (eds Weiland, H., Rollet, A. D. & Cassada, W. A.) (Wiley, Pittsburgh, 2012), 795–800. doi:`10.1002/9781118495292.ch117`. <`http://onlinelibrary.wiley.com/doi/10.1002/9781118495292.ch117/summary`>.

33. Rose, S. *et al.* Arc attachments on aluminium during tungsten electrode positive polarity in TIG welding of aluminium. *Welding in the World* **55,** 91–99 (2011).

34. Tändl, J. & Enzinger, N. *Erzeugung von Pinstrukturen an 5xxx und 6xxx Aluminiumlegierungen unter Verwendung eines Elektronenstrahls* tech. rep. (Institute for Materials Science and Welding, TU Graz, 2012).
35. Wittwer, L. & Enzinger, N. *Simulating the welding process of pin structures* in *Tagungsband Sysweldforum 2011* (Weimar, 2011), 45–54.
36. Incropera, F. P. *Fundamentals of heat and mass transfer* 6th ed. (Wiley, Hoboken, NJ, 2007).
37. ESI. *SIL Reference Manual* 2013.
38. Wittwer, L. & Enzinger, N. *Optimization of a heat source using ABC algorithm* in *Mathematical Modelling of Weld Phenomena 10* (eds Enzinger, N. & Cerjak, H.) (2013).
39. *Python Programming Language – Official Website* <http://www.python.org/>.
40. Touloukian, Y. & Ho, C. *Properties of aluminum and aluminum alloys* tech. rep. (West Lafyette, 1973), 541.
41. Rechner, R., Jansen, I. & Beyer, E. Influence on the strength and aging resistance of aluminium joints by laser pre-treatment and surface modification. *International Journal of Adhesion and Adhesives* **30,** 595–601 (Oct. 2010).
42. Läpple, V. *Einführung in die Festigkeitslehre : Lehr- und Übungsbuch ; mit 49 Tabellen / Volker Läpple* 2nd ed., 420 (Vieweg + Teubner, Wiesbaden, 2008).
43. Goyal, V. K., Johnson, E. R. & Goyal, V. K. Predictive strength-fracture model for composite bonded joints. *Composite Structures* **82,** 434–446 (Feb. 2008).
44. Anyfantis, K. N. & Tsouvalis, N. G. A novel traction–separation law for the prediction of the mixed mode response of ductile adhesive joints. *International Journal of Solids and Structures* **49,** 213–226 (Jan. 2012).
45. Goncalves, J. P. M., de MOURA, M. F. S. F., Magalhaes, a. G. & de CASTRO, P. M. S. T. Application of interface finite elements to three-dimensional progressive failure analysis of adhesive joints. *Fatigue Fracture of Engineering Materials and Structures* **26,** 479–486 (May 2003).
46. Pahr, D. H. *Experimental and Numerical Investigations of Perforated FRP- Laminates* PhD thesis (TU Wien, 2003), 150.
47. Ucsnik, S. & Staffenberger, T. *Numerilcal model of acylinder pin reinforced metal to composite single-lap shear joint* in *ECOMAS* (Vienna, 2012).

48. Dessault Systems. *Abaqus* 2011. <http://www.3ds.com/support/certified-hardware/simulia-system-information/abaqus-611/abaqus-611-supported-platforms-products/>.

49. Woelke, P. B., Shields, M. D., Abboud, N. N. & Hutchinson, J. W. Simulations of ductile fracture in an idealized ship grounding scenario using phenomenological damage and cohesive zone models. *Computational Materials Science.* doi:10.1016/j.commatsci.2013.04.009. <http://linkinghub.elsevier.com/retrieve/pii/S0927025613001705> (May 2013).

50. Anyfantis, K. N. & Tsouvalis, N. G. Loading and fracture response of CFRP-to-steel adhesively bonded joints with thick adherents – Part II: Numerical simulation. *Composite Structures* **96,** 858–868 (Feb. 2013).

51. Feith, A., Hein, R., Johnstone, C. & Flagella, P. *Thermophysical properties of low carbon 304 stainless steel to 1350C* in *Thermal conductivity, proceedings of the sight conference* (eds Ho, C. & Taylor, R.) (LaFayette, IN, 1969), 1051–1065. <http://apps.webofknowledge.com/full_record.do?product=UA&search_mode=GeneralSearch&qid=1&SID=Q2NKSt6QOlp5V4YBV6s&page=1&doc=1>.

52. Davis, J. R. & for Metals, A. S. *Properties and selection: irons, steels, and high-performance alloys* 9. print., XI, 1063 S. (ASM International, Materials Park, Ohio, 2008).

Appendices

A. Material data

A.1. Stainless steel

Chemical composition In Table 3.1 on page 27 the chemical compositions of the base and filler material are listed.

Thermo-electrical properties The following graphs show the temperature dependence of the material parameters used in the finite element simulations. For electro-thermal calculations the following parameters were utilized:

- thermal conductivity λ (Figure A.3d and A.1a)
- density ρ (A.1b)
- electrical resistivity R (A.1c)
- specific heat capacity c_p (A.1d)

The density, the electrical resistivity and the specific heat capacity we assumed to be equal for the base (AISI 304) and the filler material (AISI 308).

Mechanical properties Mechanical simulations demand for the properties listed below:

- Young's modulus E (Figure A.2a and A.3a)
- yield stress σ_y (Figure A.2b and A.3b)
- thermal expansion coefficient α (Figure A.2c)
- the plastic stress-strain relation (Figure A.2d and A.3c)

The thermal expansion coefficient was assumed to be equal for filler and base material.

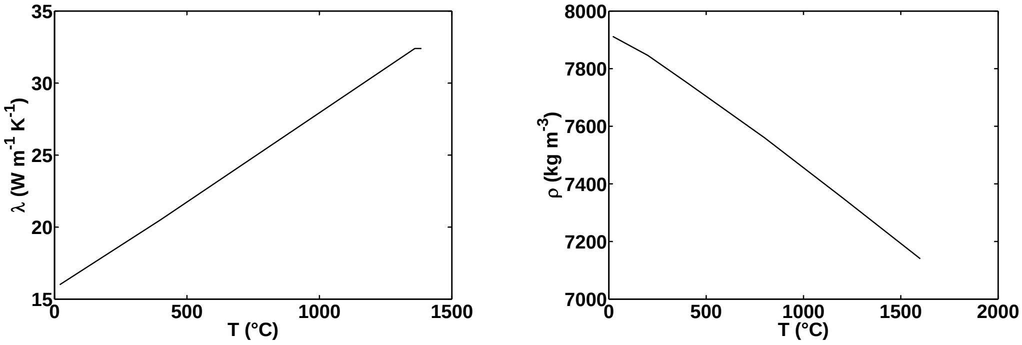

(a) Thermal conductivity

(b) Density

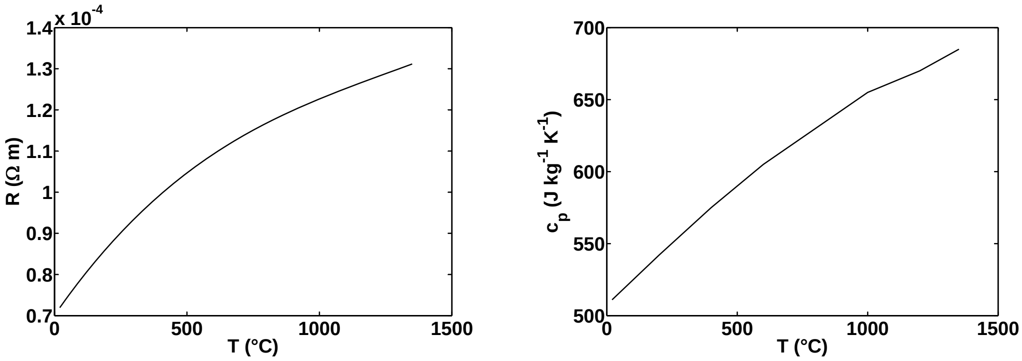

(c) Electrical resistivity; from [51]

(d) Heat capacity

Figure A.1.: Thermo-electrical properties of the base material AISI 304, if not stated differently the data was taken from the SYSWELD database.

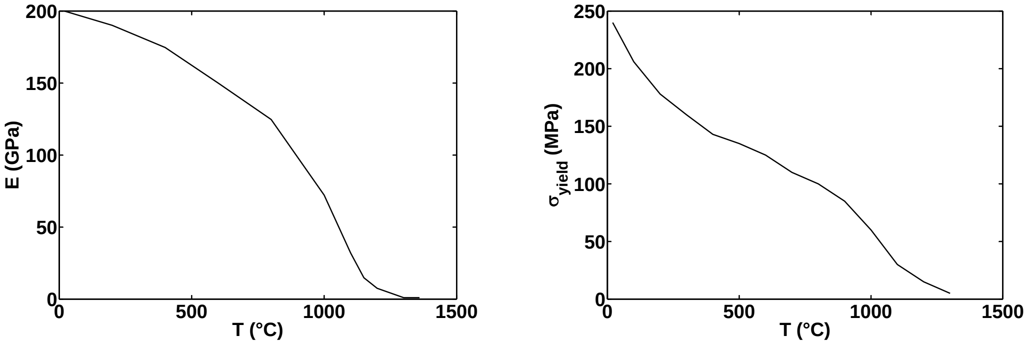

(a) Young's modulus

(b) Yield stress

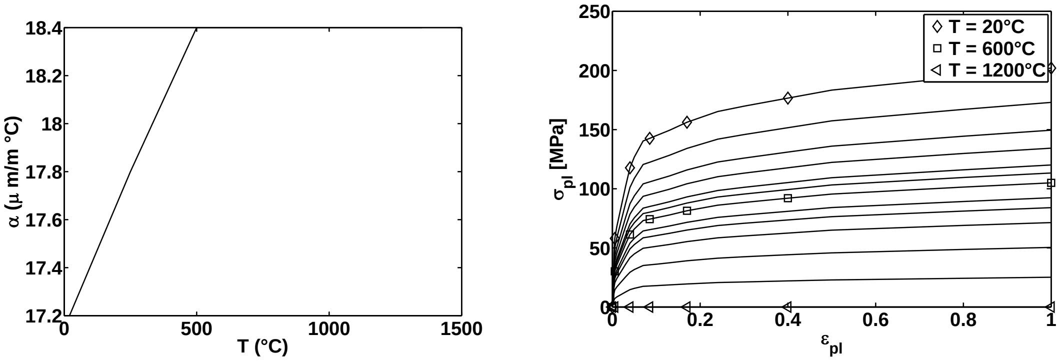

(c) Thermal expansion coefficient

(d) Plastic stress strain relations

Figure A.2.: Thermo-mechanical properties of the base material AISI 304 taken from the SYSWELD database.

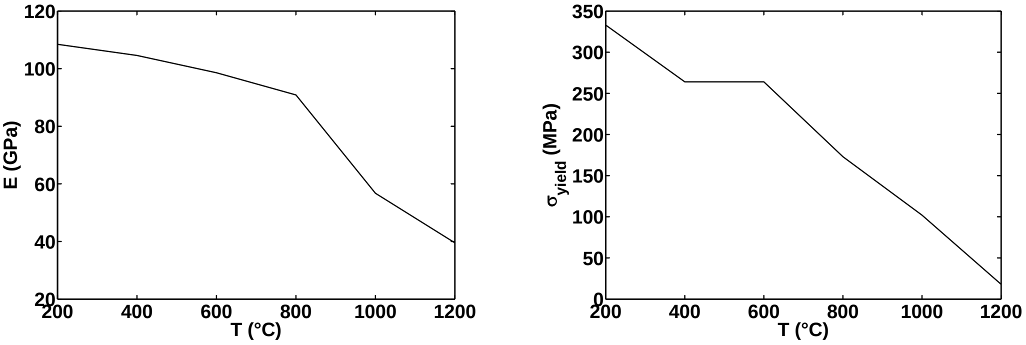

(a) Young's modulus

(b) Yield stress

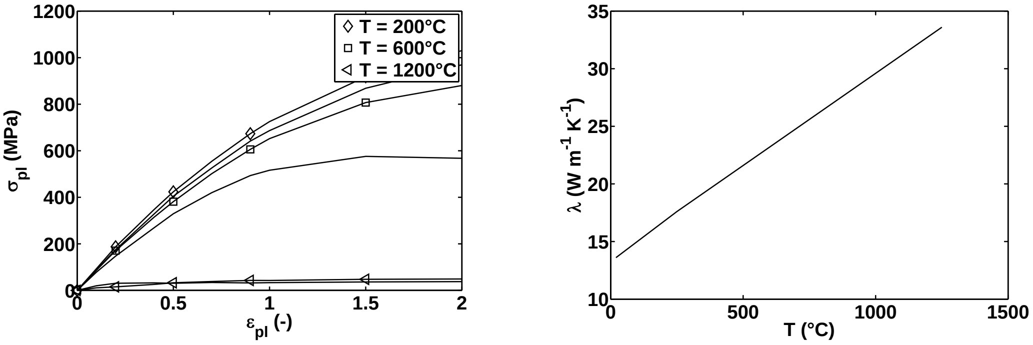

(c) Plastic stress strain relations

(d) Thermal conductivity ; from [52]

Figure A.3.: Thermo-mechanical properties of the base material AISI 308 as measured by the LKR at Ranshofen.

B. Python script used in the ABC algorithm

The ABC optimization algorithm described in Section ?? was realized using the Python script below:

```
import numpy as np;
import pylab as pl;
# importing the script lwfun.py with all the necessary funtions used below
import lwfun as lw;



## ABC optimization
##
##
## Initialize
##
# number of parameter sets:
sn = 15
# dimension of a single parameter set = number of parameters to be optimized:
d = 6
# max. number of optimization cycles
c_max = 20
# number of allowed rejections for a prameter set:
lim_failure = 10
cycle = 1
# lower and upper boundaries for the parameters:
x_min = [0.6,0.4,0.5,0.6,0.001,0.70]
x_max = [1.5,1.0,1.0,1.5,0.05,0.90]
```

```
x = np.zeros((sn,d))
v = np.zeros((1,d))
F_x = np.zeros((sn,6))
F_x_best = np.zeros((c_max+1,6))
rate_emp = np.zeros(c_max)
rate_on = np.zeros(c_max)
n_violation_emp = np.zeros(c_max)
n_violation_on = np.zeros(c_max)



p = np.zeros(sn)
fit = np.zeros(sn)

x_best = np.zeros((c_max+1,d));

# randomly evaluating the initial parameter values
# between the lower and upper boundaries

for i in range(sn):
        k = np.random.rand()
        for j in range(d):
                x[i,j] = x_min[j]+k*(x_max[j] - x_min[j])
        F_x[i] = lw.evaluate(x[i,:])
        if F_x[i,5] < 0: fit[i] = 1 + np.absolute(F_x[i,5])
        else: fit[i] = 1/(1+F_x[i,5])
failure = np.zeros(sn)

ind_best = np.nonzero(min(F_x[:,5])== F_x[:,5]);
F_x_best[0] = F_x[ind_best];
x_best[0] = x[ind_best]

print 'F_x Beginning: \n'
print F_x

print 'x_init'
```

```
print x

##
##Evaluate
##

# employers’ phase
while cycle <= c_max:
        print cycle
        accept = 0
        for i in range(sn):
                pr = 2*(np.random.rand()-0.5)
                k = np.random.randint(sn)
                while k == i: k = np.random.randint(sn)
                for j in range(d):
                    v[0,j]= x[i,j] + pr*(x[i,j] - x[k,j])
                    if v[0,j] > x_max[j]: v[0,j] = x_max[j]
                    if v[0,j] < x_min[j]: v[0,j] = x_min[j]



                F_v = lw.evaluate(v[0])
                if F_v[5] < 0:
                        fit_v = 1 + np.absolute(F_v[5])
                else:
                        fit_v = 1/(1+F_v[5])

                if fit_v > fit[i]:
                        x[i] = v
                        F_x[i] = F_v
                        fit[i] = fit_v
                        failure[i] = 0;
                        accept = accept + 1.0
                else:
                        failure[i] = failure[i]+1
```

```
        p = fit/sum(fit)
        rate_emp[cycle-1] = accept/sn
        print 'acceptance rate employed: %6.4f ' %rate_emp[cycle-1]


# onlookers' phase

        t=0
        i=0
        accept = 0
        while t < sn:
                if np.random.rand() < p[i]:
                        t = t+1
                        pr = 2*np.random.rand()-1
                        k = np.random.randint(sn)
                        while k == i:k = np.random.randint(sn)
                        for j in range(d):
                                v[0,j] = x[i,j] + pr*(x[i,j] - x[k,j])
                                if v[0,j] > x_max[j]: v[0,j] = x_max[j]
                                if v[0,j] < x_min[j]: v[0,j] = x_min[j]

                        F_v = lw.evaluate(v[0])
                        if F_v[5] < 0:
                                fit_v = 1 + np.absolute(F_v[5])
                        else:
                                fit_v = 1/(1+F_v[5])

                        if fit_v > fit[i]:
                                x[i] = v
                                F_x[i] = F_v
                                fit[i] = fit_v
                                failure[i] = 0;
```

```
                                accept = accept + 1.0
                        else:
                                failure[i] = failure[i]+1




                i=i+1
                i = np.mod(i,sn)

        rate_on[cycle-1] = accept/t
        print ’acceptance rate onlookers: %6.4f ’ %rate_on[cycle-1]

# checking if a parameter set was rejected more often as allowed by lim_failure

        if any(failure > lim_failure):
                i = np.nonzero(failure > lim_failure)
                i_l = len(i[0]);
                for k in range(i_l):
                        ind = i[0][k];
                        for j in range(d):
                                k = np.random.rand()
                                x[ind,j] = x_min[j] + k*(x_max[j] - x_min[j])
                        F_x[ind] = lw.evaluate(x[ind,:])
                        if F_x[ind,5] < 0: fit[ind] = 1 + np.absolute(F_x[ind,5])
                        else: fit[ind] = 1/(1+F_x[ind,5])

# searching for a new best set of parameters
        if min(F_x[:,5]) < F_x_best[cycle-1,5]:
                ind_best = np.nonzero(min(F_x[:,5])== F_x[:,5]);
                F_x_best[cycle] = F_x[ind_best]
                x_best[cycle] = x[ind_best]
                print ’new best!!’
        else:
                F_x_best[cycle] = F_x_best[cycle-1]
                x_best[cycle] = x_best[cycle-1]
```

```
        fplate = 1-x_best[cycle,2]

        fmt1 = '%10.8f '
        f = open ("best_parameters.dat","w")
        for k in range(cycle+1):
                for i in range(d):
                        f.write(fmt1 %x_best[k,i])
                f.write("\n")
        for i in range(cycle): f.write(fmt1 %rate_emp[i])
        f.write("\n")
        for i in range(cycle): f.write(fmt1 %rate_on[i])
        f.close()
        f = open ("best_solutions.dat","w")
        for k in range(cycle+1):
                for i in range(6):
                        f.write(fmt1 %F_x_best[k,i])
                f.write("\n")
        f.close();
        print 'F_x_best: %6.4f ' %F_x_best[cycle,5];
        print 'best parameters: '
        print 'x_pin %10.8f ' %x_best[cycle,0]
        print 'y_pin %10.8f ' %x_best[cycle,1]
        print 'f_pin %10.8f ' %x_best[cycle,2]
        print 'x_plate %10.8f ' %x_best[cycle,3]
        print 'y_plate %10.8f ' %x_best[cycle,4]
        print 'f_plate %10.8f ' %fplate
        print 'eta %10.8f ' %x_best[cycle,5]
        cycle = cycle+1


print 'F_x Final: \n'
print F_x
```

```
print '########################### \n '
print 'OPTIMIZATION COMPLETE \n '
print '########################### \n '
```

B.1. Subscripts and functions

The routine `lwfun.py` :

```
import numpy as np;
import os;

## Function to evaluate the dimensions of the calculated molten zone

def evaluate(x_in):
# target parameters:
        h_pin_t = 0.79
        h_pinmid_t = 0.74
        r_plate_t = 0.79
        d_plate_t = 0.12
        target = np.zeros(4);
        target[0] = h_pin_t;
        target[1] = h_pinmid_t;
        target[2] = d_plate_t;
        target[3] = r_plate_t;
# input parameters - heat soure parameters for the Goldak heat source:
        x_pin = x_in[0]
        y_pin = x_in[1]
        f_pin = x_in[2]
        x_plate = x_in[3]
        y_plate = x_in[4]
        eta = x_in[5]

        err = np.zeros(6);
        cmdline_sysweld = r'C:\"Program Files (x86)"\"ESI
        Group"\SYSWORLD_en\2012.0\Sysworld -prod sysweld -batch -64 -multi 2 -input
        solve.dat'
```

```
    cmdline_eval = r’C:\win-bash\bash.exe ./eval_molten_zone’
    f_plate = 1 - f_pin;
    f1 = ’%10.8f ’
    form = 7*f1;
# writing  the heat source parameters in a file for further use in SYSWELD
    f = open(’heat_source_coeffs’,’w’);
    f.write(form % (x_pin,y_pin,eta,f_pin,x_plate,y_plate,f_plate))
    f.close()
# executing sysweld for the thermal FE calculations:
    os.system ("%s" % cmdline_sysweld)
# executing the shell script ’eval_molten_zone’ to extract nodal temperatures and
coordinates:
    os.system ("%s" % cmdline_eval)

# output of the ’eval_molten_zone’ script
    o_file = ’T_nodes’;
    T_o = np.loadtxt(o_file)

    n_c = np.uint16(T_o[-1,0]);

    filetree = ’T_files/T_temp_’
    n_nodes = np.int_(len(T_o)-1);
    T_field = np.zeros((n_nodes,n_c))

# evaluating the dimensions of the calculated molten zone
    for l in range(n_nodes):
            T_field[l,0:3]=T_o[l,0:3];

    for k in range(1,n_c,2):
        filename = filetree+’%i’% k
        T_a = np.loadtxt(filename)
        for l in range(n_nodes):
            T_field[l,(k+1)/2+2]=T_a[l];
```

```
h_plate = 3;
w_wire = 0.4;

n_col = np.size(T_field,1);

T_max = np.zeros((len(T_field),4));

for i in range(len(T_field)):
        T_max[i,0] = T_field[i,0];
        T_max[i,1] = T_field[i,1];
        T_max[i,2] = T_field[i,2];
        T_max[i,3] = np.max(T_field[i,3:n_col]);


T_melt = 1350.0; # Melting temp. of the material

# dtermining the nodes of molten material:
m = np.nonzero(T_max[:,3] >= T_melt);

molten  = T_max[m,:];
molten = molten[0][:][:]

#molten 'nodes' along the symmetry axis
x0 = np.nonzero(molten[:,1] < 8e-5);



T_x0 = molten[x0,:];
T_x0 = T_x0[0][:][:];





i_hpinmid = np.argmax(T_x0[:,2]);
hpinmid = T_x0[i_hpinmid,2] - h_plate;
```

```
#        print hpinmid

        i_dplate = np.argmin(T_x0[:,2]);

        dplate = h_plate - T_x0[i_dplate,2];
        if dplate<0: dplate = 0;

#        print dplate

        ymax = np.argmax(molten[:,2]);
        nd_max = molten[ymax,:];

        dx = nd_max[1] - w_wire;



        if dx >= w_wire:
                hpin = nd_max[2] - h_plate;
        elif abs(dx) < 1e3:
                hpin = nd_max[2] - h_plate;
        else:
                x_left = np.nonzero(molten[:,1] >= w_wire);
                nd_left = molten[x_left,:];
                nd_left = nd_left[0][:][:];

                i_hpin = np.argmax(nd_left[:,2]);
                hpin = nd_left[i_hpin,2] - h_plate;

#        print hpin


        rr = np.nonzero(molten[:,2] < 3.001);
        if np.size(rr) == 0:
                rplate = 0;
```

```
        else:
                ir = np.argmax(molten[rr,1]);
                in_r = rr[0][ir];
                rplate = molten[in_r,1];
                if rplate<0: rplate = 0;
#        print rplate

        pool_par = np.zeros(4);
# calculating the error function
        pool_par[0] = hpin;
        pool_par[1] = hpinmid;
        pool_par[2] = dplate;
        pool_par[3] = rplate;

        err[0] = hpin;
        err[1] = hpinmid;
        err[2] = dplate;
        err[3] = rplate;
        err[4] = max(T_max[:,3]);
        d_1 = (target - pool_par)/target;
        diff = np.sum((d_1)**2);
        err[5] = np.sqrt(diff);

        return err
```

C. SIL scripts

C.1. The script shape_pin.cmd

The following SIL (SYSWELD interface language) was used to calculate the electro-thermal mechanical coupling:

```
list param$, val$;
variable fn$, c$;
list icrd, tt;
variable ac[3];

n_t_tran = 1000;
n_m_tran = 2000;
new_data = 2100;

T_rip = 1350.0;

t_fin = 0.55;
t_start = 0.409;
t_int = 0.001;

compile("update_mesh","update_mesh","update_mesh",0,0);
load("update_mesh");

/**********************************
loop
**********************************/

t_lim = t_start;
while(t_lim < t_fin)
```

```
{
t_lim = t_lim + t_int;

initialize_list(param$);
param$ = file_parameter("pin_cyl_shape_HT.par");
initialize_list(val$);
sprintf(c$,"%f",t_lim); val$ #= c$;
sprintf(fn$,"pin_cyl_shape_HT.dat");
file_instanciation("pin_cyl_shape_HT.par",param$,val$,fn$);

systus_file("pin_cyl_shape_HT.dat");


initialize_list(param$);
param$ = file_parameter("pin_cyl_shape_MECH.par");
initialize_list(val$);
sprintf(c$,"%f",t_lim); val$ #= c$;
sprintf(fn$,"pin_cyl_shape_MECH.dat");
file_instanciation("pin_cyl_shape_MECH.par",param$,val$,fn$);

systus_file("pin_cyl_shape_MECH.dat");


update_mesh()
systus_file("update_mesh.dat");

/****************************/

/**********************
check rip off
***********************/

n_nodes = code_systus("nmax");
// find last thermal card
systus("NAME pin_cyl_");
```

```
sprintf(c$,"OPEN TRAN %d",n_t_tran);
systus(c$);
initialize_list(icrd);
icrd #= tran_maps(1);
n_length = length(icrd);
n_t_card = icrd[n_length];


for(nn=1;nn<=n_nodes;nn=nn+1)
{
num_e = int_node_ext_number(nn);
initialize_list(tt);
tt #= trans_node_displacement(n_t_card,num_e);
if(tt[1] > T_rip) goto exit_point;
}
systus("DEASSIGN 19");
tt[1]?;
num_e?;
}

exit_point: systus("DEASSIGN 19");
tt[1]?;
num_e?;
ac = node_coordinate(num_e);
ac?;
unload("update_mesh");
```

The routine `update_mesh.cmd` was used in order to generate a new mesh file considering the displaced nodes after the mechanical calculations:

```
list icrd;
list param$, val$;
variable fn$, c$;

 n_t_tran = 1000;
 n_m_tran = 2000;
 new_data = 2100;
```

```
// find last mechanical card
systus("NAME pin_cyl_");
sprintf(c$,"OPEN TRAN %d",n_m_tran);
systus(c$);
initialize_list(icrd);
icrd #= tran_maps(1);
n_length = length(icrd);
n_m_card = icrd[n_length];  n_m_card?;   // check
systus("DEASSIGN 19");


// prepare new thermal mesh
initialize_list(param$);
param$ = file_parameter("UPDATE_MESH.par");
initialize_list(val$);
param$?;

sprintf(c$,"%d",n_m_tran); val$ #= c$; // par1: no. of mechanical DATA file
sprintf(c$,"%d",n_m_tran); val$ #= c$; // par2: no. of mecanical TRAN file
sprintf(c$,"%d",n_m_card); val$ #= c$; // par3: last mechanical card
sprintf(c$,"%d",new_data); val$ #= c$; // par4: no. of new mesh file
val$?;
sprintf(fn$,"UPDATE_MESH.dat");
file_instanciation("UPDATE_MESH.PAR",param$,val$,fn$);
```

C.2. The script transfer_data_3d.cmd

The following SIL script was used in order to transfer the results from a radial symmetric FE calculation onto a setup for 3D calculation. Prior to the actual execution of the script the following steps must be carried out:

1. Generating a 3D mesh by rotating the 2D mesh from the radial symmetric calculation around the rotational axis.
2. Perform a single step mechanical FE simulation without any loads in order to get

a result file.

After that the script below allocates the 2D elements to the according 3D elements and transfers the results (residual stresses, strains ...).

```
variable axi_name$ = "pin_cyl_calm_"; // name of the axisymmetric transient file
variable spatial_name$ = "cyl_3d_calc_"; // name of the spatial transient file
list icrd, nodes_center, num_nodes, nodes_spat,
l_nodes,nodes_el,nod_2d,nod_3d,n_el_list_3d,n_el_xy_plane, n_el_list_2d;
variable c$,r_coord[3],r_new[3],disp_nod[3], coord_c[3];
variable stress_nod[40],stress_plane[5000,40];
variable coord_plane[5000,3], num_plane[5000,2], disp_plane[5000,3];
variable n_list_elements[1500,2],stress_el[200],stress_el3d[540],
         stress_g_2d[40],stress_g_3d[60],n_mod_pars[2];
variable stress_el_plane[5000,200], num_elements_axi[5000,5], nod_el[4],
num_elements[50000,2], num_el_2d[5000,4];



$compile "transfer_stresses_axisym";
$load "transfer_stresses_axisym";

k=open_file("model_pars.dat","read");
for(l=1;l<3;l=l+1){
read_file(k,"%d",n_mod_pars[l]);
}
close_file(k);




k=open_file("el_rad_3d.dat","read");
for(m=1;m<=n_mod_pars[1];m=m+1){
read_file(k,"%d",n_list_elements[m,1]);
read_file(k,"%d",n_list_elements[m,2]);
}
close_file(k);

n_layer = 12;
```

```
n_m_tran = 2000;
pi = acos(-1);
phi = 2*pi/n_layer;
/* ---------------------------------------------------------------------
Reading data from initial axisymmetric tran & data file
------------------------------------------------------------------ */

sprintf(c$,"NAME %S",axi_name$);
systus(c$);
sprintf(c$,"SEARCH TRAN data %d",n_m_tran);
systus(c$);

initialize_list(icrd);
icrd #= tran_maps(1);
n_cards = length(icrd);
n_l_card = icrd[n_cards];


n_lim = n_mod_pars[1];
for(ii=1;ii<=n_lim;ii=ii+1)
{
  n_e = n_list_elements[ii,1];
  stress_el = trans_element_stress(n_l_card,n_e);
  for(kk=1;kk<=200;kk=kk+1) stress_el_plane[ii,kk] = stress_el[kk];
}

systus("DEASSIGN 19");



// ///////////////////////////////////////////
// open 3d tran and data file:
//

sprintf(c$,"NAME %S",spatial_name$);
```

```
systus(c$);
sprintf(c$,"SEARCH DATA TRAN %d",n_m_tran);
systus(c$);

initialize_list(icrd);
icrd #= tran_maps(1);
n_cards = length(icrd);
n_l_card = icrd[n_cards];

printf("**************************************************** \n");
printf("starting transformation \n");
printf("**************************************************** \n");

/* ------------------------------------
assign  data on each layer ----
------------------------------------ */



for(k_l=0;k_l<n_layer;k_l=k_l+1)
{

  printf("transferring data to layer %d  ",k_l+1);
  for(i=1;i<=n_mod_pars[1];i=i+1)
  {
    n_el2d = n_list_elements[i,1];
    n_el3d = n_list_elements[i,2] + k_l;
    num_nod_el3d =number_of_nodes_in_element(n_el3d);

    for(l_st=1;l_st<=40;l_st = l_st+1){
     stress_g_2d[l_st] = stress_el_plane[i,l_st];
    }
    psi = 0.;
    transfer_stresses_axisym(stress_g_2d,psi,stress_g_3d);

    for(k_st=1;k_st<=60;k_st = k_st+1){
```

```
 stress_el3d[k_st] = stress_g_3d[k_st];
}

if(num_nod_el3d < 8) // find elements with 6 nodes
{ // averaging gauss points
  psi = phi*k_l + 0.5*phi;
  for(l_st=1;l_st<=40;l_st = l_st+1){
   stress_g_2d[l_st] = (stress_el_plane[i,l_st+40]
   + stress_el_plane[i,l_st+80])*0.5;
  }
  transfer_stresses_axisym(stress_g_2d,psi,stress_g_3d);
  for(k_st=1;k_st<=60;k_st = k_st+1){
   stress_el3d[k_st+60] = stress_g_3d[k_st];
  }
  for(l_st=1;l_st<=40;l_st = l_st+1){ stress_g_2d[l_st] =
  (stress_el_plane[i,l_st+120] + stress_el_plane[i,l_st+160])*0.5;
  }
  transfer_stresses_axisym(stress_g_2d,psi,stress_g_3d);
  for(k_st=1;k_st<=60;k_st = k_st+1){
   stress_el3d[k_st+120] = stress_g_3d[k_st];
  }
  for(k_st=1;k_st<=360;k_st = k_st+1){
   stress_el3d[k_st+180] = 0;
  }
}
else
{
  for(l_3d=1;l_3d<=2;l_3d = l_3d + 1)
  {
    if(l_3d==1) psi = phi*k_l + 0.25*phi;
    if(l_3d==2) psi = phi*k_l + 0.75*phi;

    for(ng=1;ng<=4;ng=ng+1)
    {
      for(l_st=1;l_st<=40;l_st = l_st+1)
```

```
          {
           ind_plane = (40*ng)+l_st;
           stress_g_2d[l_st] = stress_el_plane[i,ind_plane];
          }
          transfer_stresses_axisym(stress_g_2d,psi,stress_g_3d);
          for(k_st=1;k_st<=60;k_st = k_st+1)
          {
           ind_3d = (l_3d-1)*ng*60 + k_st;
           stress_el3d[ind_3d] = stress_g_3d[k_st];
          }
        }
     }
    }
    modify_trans_element_stress(n_l_card,n_el3d,stress_el3d);
  }
printf("DONE \n");
}

sprintf(c$,"SAVE DATA TRAN %d",n_m_tran);
systus(c$);

systus("DEASSIGN 19");
```

The SIL script above uses the routine `transfer_stresses_axisym.cmd` in order to transfer the results from the radial symmetric calculation to the 3D files.

```
argument stress_2d[],psi,stress_el3d[];

    variable T_s[6],T_n[6],R[3,3];

    R[1,1]=cos(psi);
    R[1,2]=0.;
    R[1,3]=-sin(psi);
    R[2,1]=0.;
    R[2,2]=1;
    R[2,3]=0.;
    R[3,1]=sin(psi);
```

```
R[3,2]=0.;
R[3,3]=cos(psi);
// Transforming stesses :
stress_el3d[1] = stress_2d[1];
stress_el3d[2] = stress_2d[2];
stress_el3d[3] = stress_2d[4];
stress_el3d[4] = stress_2d[3];
stress_el3d[5] = 0;
stress_el3d[6] = 0;
// Transforming strains :
stress_el3d[7] = stress_2d[5];
stress_el3d[8] = stress_2d[6];
stress_el3d[9] = stress_2d[8];
stress_el3d[10] = stress_2d[7];
stress_el3d[11] = 0;
stress_el3d[12] = 0;
// Transforming yield surface comps. alpha
stress_el3d[13] = stress_2d[9];
stress_el3d[14] = stress_2d[10];
stress_el3d[15] = stress_2d[12];
stress_el3d[16] = stress_2d[11];
stress_el3d[17] = 0;
stress_el3d[18] = 0;
// Transferring yield stress:
stress_el3d[19] = stress_2d[13];
// Transferring cum. equivalent plastic strain
stress_el3d[20] = stress_2d[14];
// Transferring temperature:
stress_el3d[21] = stress_2d[15];
// transferring time:
stress_el3d[22] = stress_2d[16];
// transferrring equivalent stress
stress_el3d[24] = stress_2d[38];
// transferring Young's mod
stress_el3d[28] = stress_2d[20];
```

```
// transferring strain energy
stress_el3d[30] = stress_2d[21];
// setting gauss point coordinates
stress_el3d[31] = stress_2d[22] * cos(psi);
stress_el3d[32] = stress_2d[23];
stress_el3d[33] = stress_2d[22] * sin(psi);
// transferring thermal strain
stress_el3d[35] = stress_2d[24];
// transforming plastic strains
stress_el3d[37] = stress_2d[25];
stress_el3d[38] = stress_2d[26];
stress_el3d[39] = stress_2d[28];
stress_el3d[40] = stress_2d[27];
stress_el3d[41] = 0;
stress_el3d[42] = 0;
//transferring phases
for(n_phase=1;n_phase<=6;n_phase=n_phase+1)
{
  in_p_3d = 43 + n_phase-1;
  in_p_2d = 29 + n_phase-1;
  stress_el3d[in_p_3d] = stress_2d[in_p_2d];
}
// Transforming yield surface comps. gamma
stress_el3d[50] = stress_2d[36];
stress_el3d[51] = stress_2d[37];
stress_el3d[52] = stress_2d[40];
stress_el3d[53] = stress_2d[39];
stress_el3d[54] = 0;
stress_el3d[55] = 0;
// transferring cum. plastic strain phase gamma
stress_el3d[56] = stress_2d[35];
```